



Norwegian University of  
Science and Technology

# Design, Numerical Modelling and Analysis of TLP Floater Supporting the DTU 10MW Wind Turbine

**Xiaoshuang Tian**

Marine Technology

Submission date: June 2016

Supervisor: Zhen Gao, IMT

Norwegian University of Science and Technology  
Department of Marine Technology





**NTNU – Trondheim**  
Norwegian University of  
Science and Technology

Design, Numerical Modeling and Analysis of  
a TLP Floater Supporting the DTU 10MW  
Wind Turbine

Xiaoshuang Tian

June 2016

Master Thesis

Department of Marine Technology

Norwegian University of Science and Technology

Supervisor: Prof. Zhen Gao

Co-supervisor: Dr. Chenyu Luan

## Preface

Since the first offshore wind turbine was constructed in the mid 1950s, the potential of offshore wind farm increases substantially with floating technologies and electricity requirement world-wide. Offshore wind resources are much stronger, more abundant and blow more consistently than land-based resources. This project represents a preliminary design of a floating Tension Leg Platform (TLP) floater concept for supporting the DTU 10MW wind turbine at water depth  $200m$ .

The initial dimensions of the TLP floater are defined by up-scaling TLP#3 designed by Erin Elizabeth [Bachynski \(2014\)](#) with a proper scale ratio. At first, this preliminary design is checked via spreadsheet study in terms of natural periods, pretensions, hydrodynamic coefficients, moment of inertias etc. In addition, the hydrostatic stability is examined by hand calculation in order to avoid TLP slacking.

Secondly, after generating the TLPWT model in GeniE, a frequency-domain linear analysis is performed to obtain hydrodynamic coefficients, first-order motions and excitation forces, which are almost equal the spreadsheet results. Moreover, considering the unique effects of second-order loads on TLP structures, the second-order loads and motions are also computed in this sep. The second-order computation requires a finite element model of the free surface. Due to the limit space of database, a mesh convergence study is carried out regarding to the mesh size and surface radius of the second-order free surface model. Additionally, the hydrostatic stability is examined by hand calculation.

Thirdly, a time-domain non-linear analysis is performed by using the state-of-art SIMO-RIFLEX-AeroDyn code with given DTU 10MW wind turbine model. Decay test, constant wind test as well as combined turbulence wind and irregular wave test are carried out to investigate the properties and performances of the TLPWT concept design further, such as natural period, damping coefficients, dynamic motions, tensions etc. in real environmental conditions. Then, the computed TLPWT parameters are checked by a series of spectrum and statistical analysis.

Moreover, the tendon tensions are examined according to ULS.

This report only focuses on the TLP floater concept. In the other two parallel project work, a semi-submersible and a spar floater are also assessed in the meantime. Finally, the TLPWT concept is compared with the SemiWT and SparWT, which are designed to support the same wind turbine. In this way, the ideal concept can be decided for supporting the DTU 10MW reference wind turbine.

Trondheim, 2016-06-01

(Your signature)

Xiaoshuang Tian

## Acknowledgment

I would like to thank the following persons for their great help during this semester:

It is a genuine pleasure to express my deep sense of thanks and gratitude to my supervisor, Prof. Zhen Gao. I am grateful for his technical advise and constant encouragement throughout the whole process. This is a difficult work filled with many kinds of challengings. Without his help, I cannot accomplished this work.

I am also very much thankful to Dr. Erin Elizabeth Bachynski for her valuable guidance, keen interest and continuous encouragement at every stage of this project. Because she did a similar work in her Phd thesis, I asked her many questions. She has replied me hundreds of emails and provided me a lot of useful suggestions with infinite patience. It is so kind of her.

I would like to express appreciation to Dr. Chenyu Luan. He has given plenty of professional guidance on the application of software GeniE, HydroD and SRA.

I want to acknowledge with gratitude, the support and love of my parents, Mrs. Shuying Hou and Mr. Qiang Tian, and also my boyfriend Dr. Tianyu Luo. They encourage me to move on and never give up all the time.

Last but not least, I would like to thank my awesome team parters, Md Touhidul Islam and Wenfei Xue. We helped, trusted and encouraged each other all the time. Working with them together makes this project much more funny.

X.T.

# Contents

Preface . . . . .	i
Acknowledgment . . . . .	iii
List of Figures . . . . .	vii
List of Tables . . . . .	xiv
<b>1 Introduction</b>	<b>1</b>
1.1 Background . . . . .	1
1.2 Floating Wind Turbine Concepts . . . . .	4
1.3 Objectives . . . . .	5
1.4 Approach . . . . .	6
1.5 Structure of the Report . . . . .	7
<b>2 Theory</b>	<b>9</b>
2.1 Wind Turbine Aerodynamics . . . . .	11
2.1.1 One-dimensional Momentum Theory . . . . .	11
2.1.2 Blade Element/Momentum Method . . . . .	12
2.1.3 Generalized Dynamic Wake Method . . . . .	14
2.1.4 Corrections . . . . .	17
2.2 Wave Loads on Slender Structures . . . . .	23
2.2.1 Morison's Equation . . . . .	23
2.2.2 Hydrodynamic Coefficients . . . . .	25
2.3 Wave Loads on Large Volume Structures . . . . .	27
2.3.1 First-order Potential Flow Theory . . . . .	27
2.3.2 Second-order Potential Flow Theory . . . . .	34

2.4	Wave-induced Response of Floating Structures	39
2.4.1	Frequency Domain Analysis	39
2.4.2	Time Domain Analysis	41
2.5	TLP Floater Response Characteristics	46
<b>3</b>	<b>TLP Wind Turbine Design</b>	<b>48</b>
3.1	Design Criteria	50
3.1.1	Stability	50
3.1.2	Natural Period	52
3.1.3	Displacement	54
3.1.4	TLP Slacking	54
3.2	Wind Turbine	55
3.3	TLP Hull	57
3.4	Tendon Mooring System	58
3.5	Summary of key parameters	59
<b>4</b>	<b>Frequency Domain Hydrostatic and Hydrodynamic Analysis</b>	<b>61</b>
4.1	Hydrostatic Stability	62
4.2	Mesh Convergence Study	65
4.2.1	Selection of Mesh Size	66
4.2.2	Selection of Free-surface Radius	72
4.3	First-order Hydrodynamic Results	74
4.3.1	Added Mass	75
4.3.2	Potential Damping	76
4.3.3	Viscous Damping	77
4.3.4	Excitation Forces	78
4.3.5	First-order RAO	79
4.4	Second-order Hydrodynamic Results	79
4.4.1	Sum-frequency Transfer Force	80
4.4.2	Difference-frequency Transfer Force	80
4.4.3	Second-order Quadratic Transfer Motion	81



<b>5 Time Domain Dynamic Analysis</b>	<b>83</b>
5.1 Free Decay Test . . . . .	87
5.2 Constant Wind Test . . . . .	91
5.3 Combined Turbulence Wind and Irregular Wave Test . . . . .	95
5.3.1 Load Case . . . . .	95
5.3.2 Case Study - TLPWT Response . . . . .	98
5.3.3 Spectral Analysis of Response . . . . .	101
5.3.4 Statistical Analysis of Response . . . . .	103
5.3.5 ULS Check for Tensions . . . . .	107
<b>6 Comparison of TLP, Spar and Semi-submersible Wind Turbines</b>	<b>109</b>
6.1 Natural Period . . . . .	110
6.2 Platform Motion . . . . .	110
6.3 Tower Base Bending Moment . . . . .	112
6.4 Blade Root Bending Moment . . . . .	113
6.5 Mooring Line Tension . . . . .	113
<b>7 Summary</b>	<b>115</b>
7.1 Summary and Conclusions . . . . .	115
7.2 Recommendations for Further Work . . . . .	118
<b>A Acronyms</b>	<b>120</b>
<b>B Specifications of the TLPWT</b>	<b>122</b>
<b>C Overview of QTFs</b>	<b>124</b>
<b>D Combined sys.dat File Generation</b>	<b>128</b>
<b>E RIFLEX Models</b>	<b>131</b>
<b>F Turbulence wind test response</b>	<b>133</b>
<b>Bibliography</b>	<b>136</b>

# List of Figures

1.1	The european wind resource map Leithead (2007) . . . . .	2
1.2	Annual and cumulative installations of offshore wind in Europe (MW) Gruet et al. (2011) . . . . .	2
1.3	Technical advancements: for instance growth in size of typical commercial wind turbines Edenhofer et al. (2011) . . . . .	3
1.4	Concepts of floating wind turbine (left to right: Spar, Semi-submersible and TLP wind turbine concepts Matzat (2014)) . . . . .	5
1.5	The model process performed in GeniE and HydroD . . . . .	7
2.1	The overview for the design of offshore structures Gao (2015) . . . . .	9
2.2	The loads acting on TLP offshore wind turbine Gao (2015) . . . . .	10
2.3	Illustration of the streamlines past the rotor and the axial velocity and pressure up- and downstream of the rotor Hansen (2008) . . . . .	11
2.4	Blade element geometry, velocities and forces Liu and Janajreh (2012) . . . . .	12
2.5	Comparison between BEM method and GDW method . . . . .	17
2.6	Helical wake pattern of single tip vortex Moriarty and Hansen (2005) . . . . .	18
2.7	Different expressions for the thrust coefficient versus the axial induction factor $a$ Liu and Janajreh (2012) . . . . .	19
2.8	Generator power output during rapid pitch changes (from $0.2^\circ$ to $3.9^\circ$ and back) for the Tjæreborg turbine, Suzuki (2009) Moriarty and Hansen (2005) . . . . .	20
2.9	Lift and drag coefficient versus different angle of attack based Lindenburg (2003) . . . . .	21
2.10	Comparison between dynamic stall and static stall Bousman (2009) . . . . .	22
2.11	Yawed rotor disc in wind field Hansen (2008) . . . . .	22

2.12	Relative importance of mass, viscous drag and diffraction forces on marine structures Faltinsen (1993) . . . . .	24
2.13	Definition of normal force, tangential force and lift force on a slender structure DNV (2014b) . . . . .	26
2.14	Calculated drag and mass coefficients due to planar oscillation compared with experimental data Obasaju et al. (1988) . . . . .	27
2.15	Linear wave body interactions problem Greco (2012) . . . . .	28
2.16	Added mass coefficients of 2D bodies Newman (1977) . . . . .	30
2.17	Surge, sway and yaw motions of a TLP in irregular seas . . . . .	36
2.18	Surge difference-frequency quadratic transfer function (QTF) for 228m classical Spar, From Haslum (1999) DNV (2010a) . . . . .	37
2.19	Breaking down an arbitrary input $x(t)$ into a series of "impulses" Newland (1993) . . . . .	42
2.20	Illustration of the coupling between SIMO, RIFLEX, AeroDyn and the external controller Bachynski (2014) . . . . .	45
3.1	TLPWT front view in GeniE . . . . .	48
3.2	TLPWT side view in GeniE . . . . .	48
3.3	Degrees of freedom for the TLPWT Refat and El-gamal (2014) . . . . .	49
3.4	Morpeth TLP Kibbee et al. (1999) . . . . .	50
3.5	SeaStar TLP hull Kibbee (1996) . . . . .	50
3.6	Characteristic features of $M-\theta$ curves Veritas (2001) . . . . .	51
3.7	Intact and damage stability of criteria of offshore structures NMD (1987) . . . . .	53
3.8	Tension leg platform TLP Moan (1994) . . . . .	55
3.9	DTU 10MW reference wind turbine Bak et al. (2013) . . . . .	55
3.10	Power and thrust as function of wind speed for the rotor computed using Ellip-Sys3D compared to HAWCStab2 simulations Bak et al. (2013) . . . . .	56
3.11	TLP hull (Its dimensions are listed in Table 3.3) . . . . .	57
3.12	Real tendons pieced together in 270-foot sections Smith (2015) . . . . .	58
3.13	Morison model of the TLPWT including the tendon mooring system in HydroD . . . . .	59
4.1	TLP panel model . . . . .	62

4.2	TLP Morison model	62
4.3	TLPWT mass model	62
4.4	Schematic side elevation of a TLP illustrating the geometric displaced position of the platform in surge/sway with pitch and set-down relationship Srinivasan (2014)	64
4.5	Meshed TLP panel model	65
4.6	Meshed free surface model	65
4.7	Free surface mesh definition for selection of mesh size	67
4.8	The meshing on the intersection of free surface model and TLP panel model	67
4.9	Mesh 1	68
4.10	Mesh 2	68
4.11	Mesh 3	68
4.12	Mesh 4	68
4.13	Mesh 1 sum-freq. QTF in heave	70
4.14	Mesh 2 sum-freq. QTF in heave	70
4.15	Mesh 3 sum-freq. QTF in heave	70
4.16	Mesh 4 sum-freq. QTF in heave	70
4.17	Diagonal QTFs in heave, pitch, roll and surge over incoming wave frequency for mesh case 1, 2 and 3	71
4.18	Free surface mesh definition for selection of surface radius	72
4.19	Mesh 3	73
4.20	Mesh 5	73
4.21	Mesh 6	73
4.22	Diagonal QTFs in heave and pitch over incoming wave frequency for mesh case 3, 5 and 6	73
4.23	Overview of the whole structure and free surface model with mesh 3	74
4.24	TLPWT model used for the first-order calculation in HydroD	75
4.25	Added mass coefficient amplitude in 6 DOF $A_{11}, / A_{22}, A_{33}, A_{44} / A_{55}, A_{66}$ (head sea)	76
4.26	Potential damping coefficient amplitude in 6 DOF $B_{11}, / B_{22}, B_{33}, B_{44} / B_{55}, B_{66}$ (head sea)	77

4.27 Comparison of surge RAO between the model with drag velocity $2m/s$ and without drag velocity in frequency domain analysisy . . . . .	77
4.28 First-order wave force excitation amplitude per unit wave amplitude in surge, heave, pitch and yaw (head sea) . . . . .	78
4.29 First-order wave force excitation amplitude per unit wave amplitude in surge, heave, pitch and yaw (head sea) . . . . .	79
4.30 Sum-freq. QTF in heave . . . . .	80
4.31 Sum-freq. QTF in pitch . . . . .	80
4.32 Difference-frequency QTF in surge . . . . .	81
4.33 Mean drift force in surge (head sea) . . . . .	81
4.34 Diff-freq. RAO in surge . . . . .	82
4.35 Sum-freq. RAO in heave . . . . .	82
4.36 Sum-freq. RAO in pitch . . . . .	82
4.37 Diff-freq. RAO in yaw . . . . .	82
5.1 Overview of the TLPWT in SIMA . . . . .	84
5.2 Description of the structural model and external load model of the TLPWT Bachynski (2014) . . . . .	85
5.3 Example of decay force with ramp duration $50s$ and constant force duration $100s$ . . . . .	87
5.4 TLPWT surge motion (m) in free decay test along time . . . . .	88
5.5 TLPWT heave motion (m) in free decay test along time . . . . .	88
5.6 TLPWT pitch motion (deg) in free decay test along time . . . . .	89
5.7 TLPWT yaw motion (deg) in free decay test along time WRONG???. . . . .	89
5.8 Recreated line and original decay line in surge decay test . . . . .	90
5.9 Time histories of platform pitch motion, thrust, rotor speed and generated power of the TLPWT under constant wind speed $8m/s$ . . . . .	91
5.10 Thrust spectrum after FFT transformation at constant wind speed $8m/s$ . . . . .	92
5.11 Mean blade pitch angle for wind speed $4m/s$ to $24m/s$ . . . . .	93
5.12 Constant wind test results for wind speed $4m/s$ to $24m/s$ . . . . .	94
5.13 Location of 18 potential European offshore sites Li et al. (2015) . . . . .	95

5.14	JONSWAP spectrum for the wave distribution in load case OP1 . . . . .	97
5.15	Time realizations of wind speed, blade pitch, generated power, surge motion, heave motion and pitch motion of the TLPWT for turbulence wind test in load case OP3 . . . . .	99
5.16	Time realizations of wind speed, blade pitch, generated power, surge motion, heave motion and pitch motion of the TLPWT for turbulence wind test in load case EX . . . . .	100
5.17	Smoothed spectra of the TLPWT responses in load case OP1, OP2, OP3 and EX . . . . .	101
5.18	Smoothed spectra of the blade and tower bending moment in load case OP1, OP2, OP3 and EX . . . . .	102
5.19	Smoothed tendon1 tension spectrum in load case OP1, OP2, OP3 and EX . . . . .	103
5.20	TLPWT surge motion . . . . .	104
5.21	TLPWT pitch motion . . . . .	104
5.22	TLPWT heave motion . . . . .	104
5.23	Tower base bending moment . . . . .	105
5.24	Blade root bending moment . . . . .	105
5.25	Time history of the tendon axial forces for the TLPWT in OP1 . . . . .	106
5.26	Tension1 . . . . .	106
5.27	Tension3 . . . . .	106
5.28	Maximum tension cdf . . . . .	107
5.29	Maximum tension pdf . . . . .	107
6.1	Mean surge motion . . . . .	111
6.2	Mean pitch motion . . . . .	111
6.3	Mean values, standard derivations and maximum values of the surge motion for the three concepts . . . . .	111
6.4	Mean values, standard derivations and maximum values of the pitch motion for the three concepts . . . . .	112
6.5	Mean values, standard derivations and maximum values of the fore-aft tower base bending moment for the three concepts . . . . .	112
6.6	Mean values, standard derivations and maximum values of the out-of-plane blade root bending moment for the three concepts . . . . .	113

6.7 Mean values, standard derivations and maximum values of the mooring line tensions for the three concepts . . . . .	114
C.1 Mesh 1 sum-freq. QTF in heave . . . . .	125
C.2 Mesh 2 sum-freq. QTF in heave . . . . .	125
C.3 Mesh 3 sum-freq. QTF in heave . . . . .	125
C.4 Mesh 4 sum-freq. QTF in heave . . . . .	125
C.5 Mesh 5 sum-freq. QTF in heave . . . . .	125
C.6 Mesh 6 sum-freq. QTF in heave . . . . .	125
C.7 Mesh 1 sum-freq. QTF in pitch . . . . .	126
C.8 Mesh 2 sum-freq. QTF in pitch . . . . .	126
C.9 Mesh 3 sum-freq. QTF in pitch . . . . .	126
C.10 Mesh 4 sum-freq. QTF in pitch . . . . .	126
C.11 Mesh 5 sum-freq. QTF in pitch . . . . .	126
C.12 Mesh 6 sum-freq. QTF in pitch . . . . .	126
C.13 Mesh 1 diff-freq. QTF in surge . . . . .	127
C.14 Mesh 2 diff-freq. QTF in surge . . . . .	127
C.15 Mesh 3 diff-freq. QTF in surge . . . . .	127
C.16 Mesh 4 diff-freq. QTF in surge . . . . .	127
C.17 Mesh 5 diff-freq. QTF in surge . . . . .	127
C.18 Mesh 6 diff-freq. QTF in surge . . . . .	127
D.1 Overview of the DeepC model . . . . .	129
D.2 The variation of the retardation element (3,3) over time . . . . .	130
D.3 The variation of the retardation element (3,3) over time . . . . .	130
D.4 The first order wave excitation part in the new sys.dat file . . . . .	130
E.1 RIFLEX wind turbine model . . . . .	132
F.1 Time realizations of wind speed, blade pitch, generated power, surge motion, heave motion and pitch motion of the TLPWT for turbulence wind test in load case OP1 . . . . .	134

E2	Time realizations of wind speed, blade pitch, generated power, surge motion, heave motion and pitch motion of the TLPWT for turbulence wind test in load case OP2	135
----	---	-----



# List of Tables

2.1	Hydrodynamic effects of importance for each floater DNV (2010a) . . . . .	35
2.2	Newmark-Beta integration parameters used in SRA simulations . . . . .	44
2.3	Typical natural periods of deep water floaters DNV (2010a) . . . . .	46
3.1	Scaling of the floater parameters using the Froude scaling law . . . . .	49
3.2	DTU 10MW Reference Wind Turbine Design Summary Bak et al. (2013) . . . . .	56
3.3	Specification of TLP floater . . . . .	58
3.4	Specifications of tether mooring system . . . . .	59
3.5	Key parameters for the DTU 10MW TLPWT preliminary design . . . . .	60
3.6	Natural periods of the TLPWT from spreadsheet calculation . . . . .	60
3.7	Added mass, storing stiffness and tendon stiffness calculation results in HydroD . . . . .	60
4.1	Free surface configuration with different mesh size for the meshing convergency test . . . . .	68
4.2	Free surface configuration with different partition radius for the meshing convergency test . . . . .	72
5.1	Simulation parameters for decay test . . . . .	88
5.2	Natural period and damping coefficients based on decay test . . . . .	90
5.3	General information and statistics of site 14 in North Sea . . . . .	96
5.4	Load cases for turbulence wind test . . . . .	97
6.1	Properties of the three floater concepts . . . . .	109
6.2	Undamped natural periods of the three WT concepts obtained by decay test . . . . .	110

7.1 Summary of TLPWT properties . . . . .	117
B.1 Main dimensions for central upper column . . . . .	122
B.2 Main dimensions for central lower column . . . . .	122
B.3 Main dimensions for pontoons . . . . .	123
B.4 Main dimensions for ballast system . . . . .	123

# Chapter 1

## Introduction

### 1.1 Background

The last century has witnessed the vital development of fossil oil as a major energy resource in the earth. However, not every country has sufficient oil storage, and still a lot of countries must rely on oil import. In addition, the unprecedented climate change resulted from GreenHouse Gases (GHG) and pollution impact arouses a new period of affordable reliable and sustainable energy development. In 2009, EU agreed the ‘climate and energy package’ setting targets for production from renewables energies, energy efficiency as well as a target for the EU to reduce greenhouse gases (GHG) emissions by 20% from 1990 levels by 2020 [Gruet et al. \(2011\)](#). It is time to develop clean energy patterns to replace traditional coal, gas and oil generation. As universally applied renewable energy, wind energy plays a significant role in a clean and low-carbon future.

Figure [1.1 Leithead \(2007\)](#) illustrates the wind source distribution in Europe. It refers to a large potential for wind energy development in Europe, especially for the coastal states, such as UK, Ireland and so on. In fact, wind energy grows rapidly in Germany, the US, France, the UK and Denmark after the Second World War [Hansen \(2008\)](#). The EWEA (The European Wind Energy Associate) estimates, there will be a total installed capacity of wind power of 230GW in the EU, producing 581 *TWh* of electricity and meeting 15.7% of electricity consumption in 2020 [Gruet et al. \(2011\)](#).

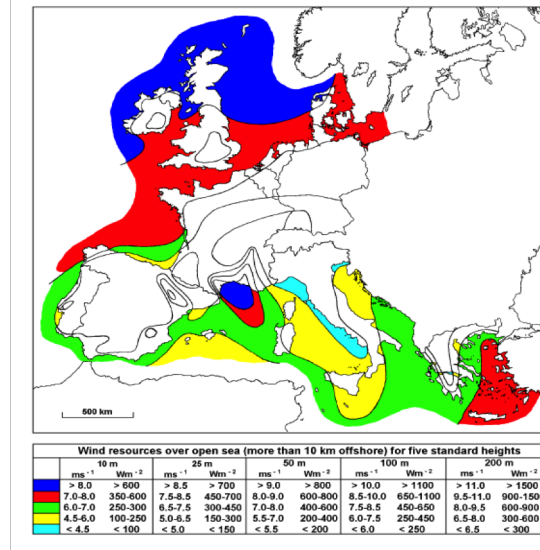


Figure 1.1: The european wind resource map [Leithead \(2007\)](#)

Before 1990s, the development of wind turbine is limited to land-based. However, potential exists in the application of offshore wind turbine in deep water for much stronger and steadier wind field. The offshore wind turbines also benefit from less noise effects and visual pollution. Recently, the wind turbine development trends to move from land space to offshore. The offshore wind turbines have been coming online. At the end of 2012, there were 1,662 turbines with totaling 5GW of installed offshore wind capacity spreading across 55 wind farms in 10 European countries (See Figure 1.2) [Gruet et al. \(2011\)](#).

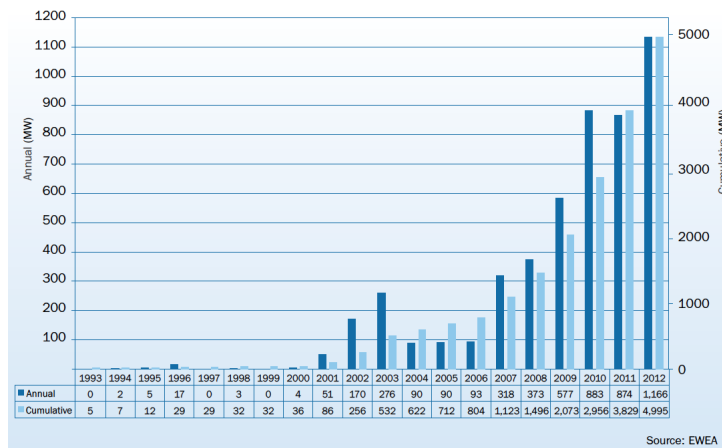


Figure 1.2: Annual and cumulative installations of offshore wind in Europe (MW) [Gruet et al. \(2011\)](#)

Comparing with bottom-fixed wind turbine structures, the main advantage of floating wind turbines is their lower design and installation costs, i.e. reduced capital expenditure (CAPEX); on the other hand, floating structures are expected to produce more energy as they can accommodate bigger wind turbines Wang (2014). This means the floating wind turbines can achieve significant savings per megawatt comparing. Wayman et al. (2006); Musial et al. (2004); Henderson et al. (2002); Lundteigen and Rausand (2008) have proven that floating-type wind farms are expected to be more economical than the fixed ones in offshore areas deeper than 40 m.

In recent years, the wind turbines trend to be in larger scales in order to reduce the cost of energy as shown in Figure 1.3. Dong energy, the world's largest developer and operator of offshore wind farms, has installed 35 Siemens 6MW turbines in the Westernmost Rough Offshore Wind Farm. This is the first time all over the world using such large scale wind turbines. This farm has reached the full power output in 26th May 2015 and provided electricity for 150,000 UK homes Alan Price (2015).

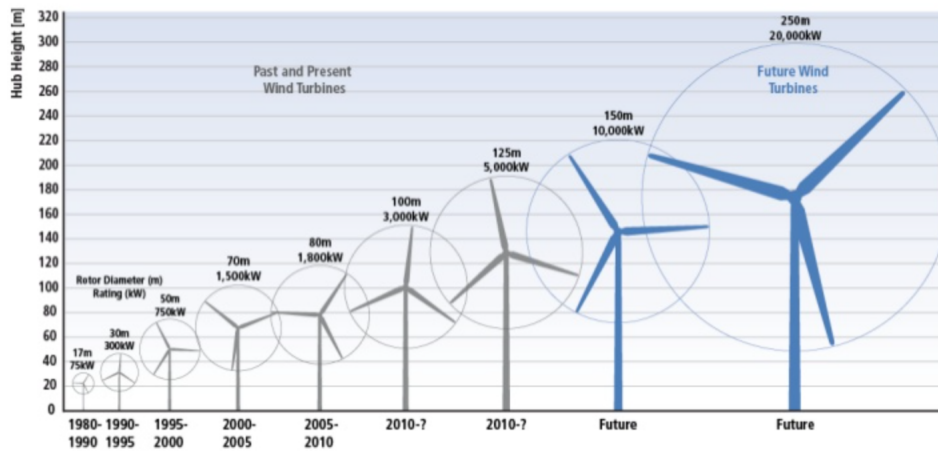


Figure 1.3: Technical advancements: for instance growth in size of typical commercial wind turbines Edenhofer et al. (2011)

Nevertheless, one must note the great challenges behind this kind of large scale offshore wind farm. Firstly, the wind turbine controller must be complex because the behaviors of the wind turbine relates to not only the tower but also the floater. Secondly, the inertia loading acting on tower should be large as a result of great floater acceleration. Last but not least, these

floating structures should be designed to work in harsh environment since they are directly exposed to the open ocean without any natural protection [Bae and Kim \(2013\)](#).

## 1.2 Floating Wind Turbine Concepts

The concept of floating wind turbine was first introduced by professor Heronemus from the University of Massachusetts at Amherst in 1970s [Manwell et al. \(2010\)](#). In recent years, the utilizing of floating wind turbine has evolved from one-time of the wind pioneers into reality.

The solution of floating wind turbine foundations mainly includes: DDF, semi-submersible, TLP, monohull structures and so on. These foundations structures present significant component of cost and have considerable influence on the vibration characteristics of the overall installation [Erich \(2000\)](#). Each type foundation is known of its specific advantages and disadvantages depending on the depth of water. This project proposes a TLP floater concept. In the meantime, a spar floater and a semi-submersible floater concept are proposed by other two students for supporting the same wind turbine (See Figure 1.4). All the concepts have the same freeboard of 10m. These concept are discussed briefly as followings [Roddier et al. \(2011\)](#); [Wang \(2014\)](#); [DNV \(2013a\)](#); [Than \(2006\)](#):

**Spar:** The Spar concept consists of a small-diameter, long single vertical cylinder supporting the wind turbine. The deep draft design of spar makes it less affects by wind, wave and current. However, it requires very nice weather to transport and install the spar wind turbine. Besides, the large draft may also limit the possibility to tow-back for major maintenance. Generally speaking, Spar has good stability and small heave motions.

**Semi-submersible:** Semi-submersible is column-stabilized unit consisting of large-diameter support columns attached to submerged pontoons. The semi-submersible can operate in flexible draft, which allows it to be fully assembled in a sheltered harbor and then wet-towed to its installation site. This process also works when there is a need for major maintenance. A main

concern is that the semi-submersible may experience large heave motions in extreme waves.

**TLP:** A TLP differs fundamentally from other floater concept, because it is the tendon stiffness rather than the water-plane stiffness that governs the vertical motions. By using long steel cables connecting to the seabed, TLP is more economically competitive than other structures. “You don’t pay anything to be buoyant,” said Paul Sclavounos, an MIT professor of mechanical engineering, who involved in a floating ocean windmills design. It has been estimated that the cost of installation and building of a TLP wind turbine is only one third of the current offshore tower wind turbine. Furthermore, the limited platform motions of a TLP structure can reduce the structural loading on the tower, gearbox and blades compared to other floating structures.



Figure 1.4: Concepts of floating wind turbine (left to right: Spar, Semi-submersible and TLP wind turbine concepts [Matzat \(2014\)](#))

### 1.3 Objectives

The total project aims to design a TLP floater to support the DTU 10MW reference wind turbine and study its stability and reliability. Since the design process has been complicated in the previous specialization project, the main objectives of this Master’s project include:

1. Perform a hydrostatic stability check for the designed TLP wind turbine by hand calculation
2. Establish a time-domain model in SIMO-RIFLEX-AeroDyn
3. Perform time-domain simulations of the TLP wind turbine for given wind and wave conditions
4. Compare the dynamic response of the TLP concept with the results from other two concepts (Spar and Semi-submersible)

## 1.4 Approach

Erin Elizabeth Bachynski designed five different sizes TLP floaters in 2014 for supporting the 5MW NREL wind turbine [Bachynski \(2014\)](#). By upscaling the TLP#3 floater with a proper scale ratio, this project determines the initial size of the TLP floater for supporting the DTU 10MW wind turbine.

Figure 1.5 shows the modeling loop of this project. The panel model, Morison model, mass model, structural model, second-order free surface model need to be built in GeniE prior to running HydroD. All the establishment processes are based on DNV manuals [DNV \(2011, 2015\)](#). In GeniE, the general informations can be computed, such as the inertia properties, mass distribution, displacement, COG, COB and so on. However GeniE is only the integral part of the DNV SESAM Package, HydroD is the next interactive application for computation of hydrostatics and stability, wave loads and response motion for ships as well as offshore structures. After inputting the GeniE models to HydroD, Wadam can then be adopted for frequency-domain analysis in wave-only conditions. In fact, Wadam applies Morison's equation, first- and second-order 3D potential theory to its wave load calculations [DNV \(2013b\)](#). Later, by using DeepC, the Wadam output (G1.SIF) is able to be converted to SIMO format (sys.dat), which is then input to SIMA. Then a time-domain model is built in SIMA. Finally, irregular time-domain simulations are carried out with specific wind and wave conditions. Section 2.4.2 introduces the SRA code



in details.

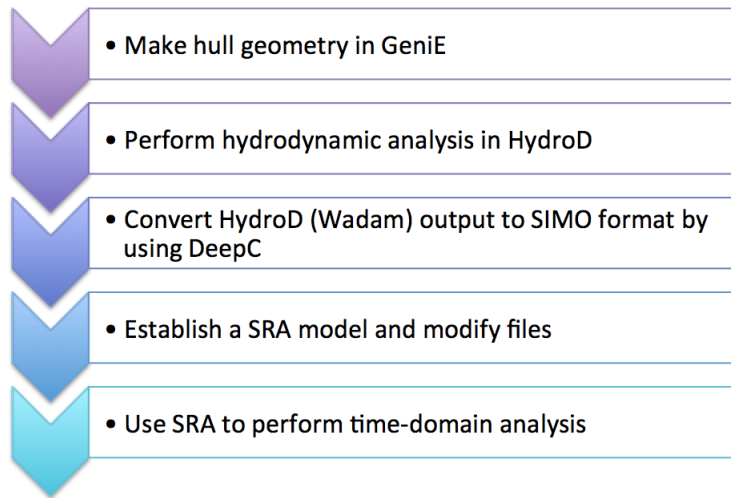


Figure 1.5: The model process performed in GeniE and HydroD

## 1.5 Structure of the Report

The report is organized as follows:

- Chapter 1 introduces the background of the offshore wind turbine development, three most popular floating wind turbine concepts (Spar, Semi-submersible and TLP), and objectives as well as approaches of this project.
- Chapter 2 provides a survey of relevant literature, such as wind turbine aerodynamics, wave loads and wave-induced response. This section also gives a detailed introduction about TLP floater response characteristics.
- Chapter 3 represents this TLPWT design regarding to design criteria, and the designed wind turbine, TLP floater, tendon mooring system, and provides a summary a key parameters.
- Chapter 4 checks the hydrostatic stability of the TLPWT, discusses the optimum mesh size and surface radius of the second-order free surface and also discusses the results of regular

frequency-domain analysis, which include both first- and second-order hydrodynamic results.

- Chapter 5 mainly focuses on the results of irregular time-domain analysis in order to check the performance of TLPWT in given environmental conditions.
- Chapter 6 compares the results of three concepts, such as response motions, natural periods, tower base bending moments, blade root bending moment etc.
- Chapter 7 summaries the total work and results. This chapter also provides several suggestions for further work in this field.

# Chapter 2

## Theory

Basically, the design of offshore structures requires a comprehensive understanding of environmental loads and induced responses (Figure 2.1). The environmental loads may come from wind, wave, current and their randomness should be considered. The resultant hydrodynamic loads can be analyzed by potential theory, the first-order linear potential theory or the second-order nonlinear potential theory, which totally depends on the shape and size of offshore structures. Further, the hydrodynamic loading on slender structures is usually expressed by the Morison's equation in terms of relative fluid-structure velocities and accelerations, for instance, the tendons of a TLP. Additionally, the wave-induced response can be solved by frequency-domain or time-domain analysis. The frequency domain analysis is used only for linear problems, while the time-domain analysis can also be used for non-linear problems. More detailed literature survey can be found in the followings of this chapter.

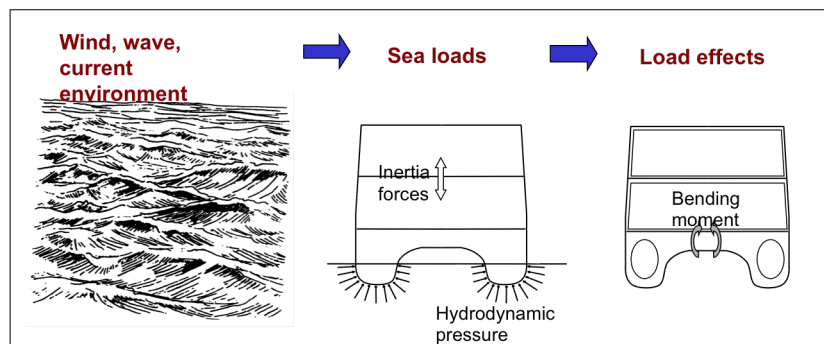


Figure 2.1: The overview for the design of offshore structures [Gao \(2015\)](#)

Figure 2.2 Gao (2015) illustrates the environmental loads acting on a TLPWT. It indicates that the integrated analysis of the TLPWT requires to consider about the turbulent wind field and random waves, as well as corresponding aerodynamic loading and hydrodynamic loading. There are no specific guidelines or standards for the design of TLPWT structures until now. However, the considerations based on the oil and gas TLPs are valuable in designing and analyzing the conceptual TLPWT design. For instance, the American Petroleum Institution's recommended practice for TLP planning, design and construction (API RP 2T) gives detailed guidances with regarding to load and response calculation API (2010). DNV's guideline for structural design of TLPs (DNV-OS-C105) is mainly based on the load and resistance factor design (LRFD) method and it also provides an example of reliability analysis of TLP DNV (2008). In addition, the DNV rule Design of Floating Wind Turbine Structures (DNV-OS-J103) offers the general design requirements for offshore floating wind turbine structures DNV (2013a) and DNV-RP-F205 gives suggestions for the global performance analysis DNV (2010a). More detailed design criteria for the TLPWT design are given in Section 3.1.

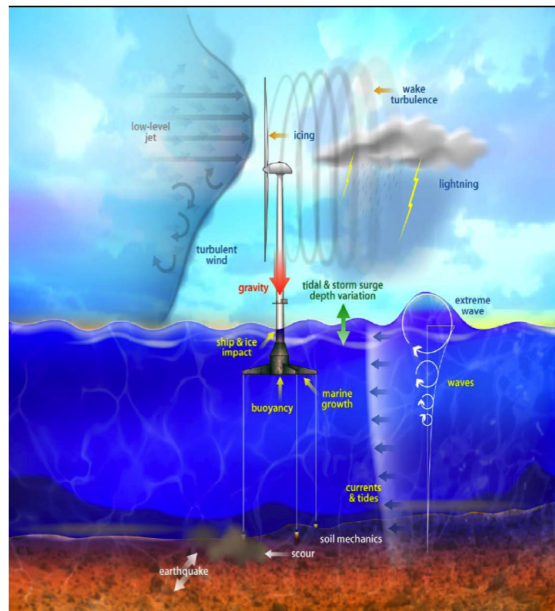


Figure 2.2: The loads acting on TLP offshore wind turbine Gao (2015)

## 2.1 Wind Turbine Aerodynamics

### 2.1.1 One-dimensional Momentum Theory

Figure 2.3 illustrates the change of wind velocity and pressure when passing the rotor of a wind turbine. The rotor acts as a drag device slowing down the wind speed from  $V_0$  to  $u$  at the blade plane and even  $u_1$  in the wake. Meanwhile, the pressure experiences a small rise first, from the atmospheric level  $p_0$  to  $p$  which is followed by a sudden drop  $\Delta p$  over the rotor, and recovers continuously to  $p_0$  in the downstream.

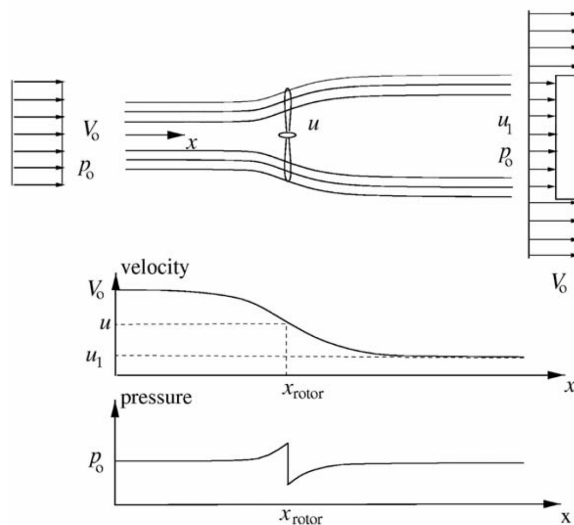


Figure 2.3: Illustration of the streamlines past the rotor and the axial velocity and pressure up- and downstream of the rotor Hansen (2008)

The pressure drop  $\Delta p$  results in a thrust force in the stream-wise direction, which reduces the wind speed from  $V_0$  to  $u$ :

$$T = \Delta p A \quad (2.1)$$

where  $A$  is the cross section area of the rotor,  $A = \pi R^2$ .

The available power in a cross-section equal to the swept area  $A$  by the rotor is represented as Eq 2.2, where  $V_0$  is the wind speed far upstream from the rotor.

$$P = \frac{1}{2} \rho A V_0^3 \quad (2.2)$$

The power coefficient can be expressed as:

$$C_p = \frac{P}{\frac{1}{2} \rho V_0^3 \pi R^2} \quad (2.3)$$

### 2.1.2 Blade Element/Momentum Method

Figure 2.4 shows a basic airfoil model. The airfoil is subjected to a lift force perpendicular to wind speed and a drag force opposite to the wind speed. The lift force is mainly caused by the pressure differential on the two sides of the airfoil. The flow velocity is typically higher (lower pressure) on the top surface of the airfoil than the lower surface (higher pressure). Whereas, the drag force is due to both pressure difference and viscous force Hansen (2015). The development of SIMO-RIFLEX-AeroDyn, which is used in the present thesis work, is performed in parallel with the implement of a BEM code within RIFLEX. With the BEM model it is possible to calculate the steady loads and thus also the thrust and power for different settings of wind speed, rotational speed and pitch angle.

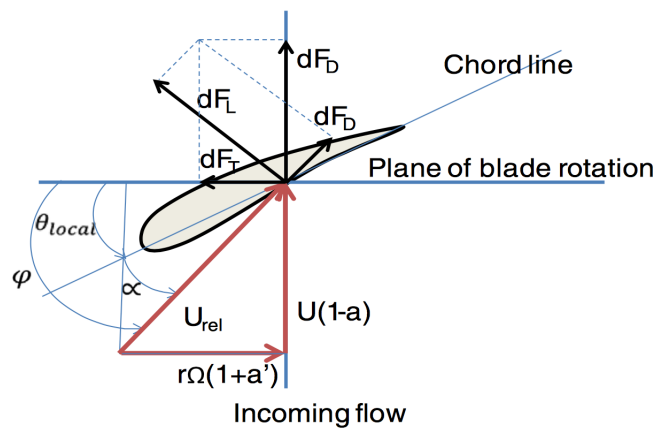


Figure 2.4: Blade element geometry, velocities and forces Liu and Janajreh (2012)

In a BEM model, the following assumptions are made Hansen (2008):

1. No radial dependency - in other words what happens at one element cannot be felt by the

others.

2. The force from the blades on the flow is constant in each annual element. This corresponds to a rotor with infinite number of blades.

Several corrections, such as Prandtl's tip loss factor, Glauert corrections for high values of  $a$  and so on, are introduced in Section 2.1.4. They are necessary for the implement of BEM method.

For an ideal rotor with the above assumptions, the thrust and torque can be computed as Eq. 2.4 and Eq. 2.5 respectively Hansen (2008).

$$dT = 4\phi r \rho V_0^2 a(1-a)dr \quad (2.4)$$

$$dM = 4\pi r^3 \rho V_0 \omega (1-a) a' dr \quad (2.5)$$

The force normal to the rotor plane is defined as  $F_N$  while the force tangential to the rotor plane is defined as  $F_T$  (Figure 2.4). According to BEM method Hansen (2015), the corresponding normal coefficient  $C_n$  and thrust coefficient  $C_t$  are:

$$C_n = C_l \cos\phi + C_d \sin\phi \quad (2.6)$$

$$C_t = C_l \sin\phi - C_d \cos\phi \quad (2.7)$$

Where  $C_l$  is lift coefficient and  $C_d$  is drag coefficient. The angle  $\phi$  accounts for the angle of attach as well as the blade pitch angle.

The axial induction factors are:

$$a = \frac{1}{\frac{4\sin^2\phi}{\sigma C_n} + 1} \quad (2.8)$$

$$a' = \frac{1}{\frac{4\sin\phi\cos\phi}{\sigma C_t} + 1} \quad (2.9)$$

Eq. 2.8 and Eq. 2.9 offer expressions for the unknown  $a$  and  $a'$ . In the meantime, the quantities  $\phi$ ,  $C_n$  and  $C_t$  depend on these two unknowns. A typical solution are [Bachynski \(2015\)](#):

1. Guess starting values for  $a$  and  $a'$ .
2. Calculate  $\phi$  and consequently  $\alpha$ ,  $C_l$  and  $C_d$ .
3. Update  $a$  and  $a'$  using Eq. 2.8 and Eq. 2.9.
4. Check for convergence within a given tolerance, if not, repeat (Starting from step 3).

### 2.1.3 Generalized Dynamic Wake Method

GDW method is an alternative method for finding the induced velocities and computing the aerodynamic loads. This method is commonly used at high wind speed, which is originally developed for helicopters [Peters and He \(1991\)](#); [Pitt and Peters \(1981\)](#). Different from BEM method, GDW method includes inherent of dynamic wake, tip loss and skewed wake effect. Moreover, this method provides a set of first-order differential equations that can be solved by using an Adams-Bashford-Moulton predictor-corrector method and does not necessarily require iteration [Bachynski \(2015\)](#). Theoretically, GDW method is based on potential flow solution to Laplace's equation. The following steps show the solution process of GDW method.

Assuming induced velocities are small compared to incident wind velocity, Euler equation can be obtained:

$$\frac{\partial u}{\partial t} + U_\infty \frac{\partial u}{\partial x} + V_\infty \frac{\partial u}{\partial y} + W_\infty \frac{\partial u}{\partial z} = -\frac{1}{\rho} \frac{\partial p}{\partial x} \quad (2.10)$$

$$\frac{\partial v}{\partial t} + U_\infty \frac{\partial v}{\partial x} + V_\infty \frac{\partial v}{\partial y} + W_\infty \frac{\partial v}{\partial z} = -\frac{1}{\rho} \frac{\partial p}{\partial y} \quad (2.11)$$

$$\frac{\partial w}{\partial t} + U_\infty \frac{\partial w}{\partial x} + V_\infty \frac{\partial w}{\partial y} + W_\infty \frac{\partial w}{\partial z} = -\frac{1}{\rho} \frac{\partial p}{\partial z} \quad (2.12)$$



The conservation of mass can be represented as:

$$\frac{\partial u}{\partial x} + \frac{\partial v}{\partial y} + \frac{\partial w}{\partial z} = 0 \quad (2.13)$$

in order to obtain the Laplace equation for the pressure distribution:

$$\nabla^2 p = 0 \quad (2.14)$$

Note that rotor speed  $\Omega$  changes *w/time*, hence non-dimensionalizations must be computed at every time step:

$$\hat{t} = \Omega t; \hat{u} = \frac{u}{\Omega R}; \hat{x} = \frac{x}{R}; \hat{U}_\infty = \frac{U_\infty}{\Omega R}; \Phi = \frac{p}{\rho(\Omega R)^2} \quad (2.15)$$

Resulting equations:

$$\frac{\partial \hat{u}}{\partial \hat{t}} + \hat{U}_\infty \frac{\partial \hat{u}}{\partial \hat{x}} + \hat{V}_\infty \frac{\partial \hat{u}}{\partial \hat{y}} + \hat{W}_\infty \frac{\partial \hat{u}}{\partial \hat{z}} = -\frac{\partial \Phi}{\partial \hat{x}} \quad (2.16)$$

$$\frac{\partial \hat{v}}{\partial \hat{t}} + \hat{U}_\infty \frac{\partial \hat{v}}{\partial \hat{x}} + \hat{V}_\infty \frac{\partial \hat{v}}{\partial \hat{y}} + \hat{W}_\infty \frac{\partial \hat{v}}{\partial \hat{z}} = -\frac{\partial \Phi}{\partial \hat{y}} \quad (2.17)$$

$$\frac{\partial \hat{w}}{\partial \hat{t}} + \hat{U}_\infty \frac{\partial \hat{w}}{\partial \hat{x}} + \hat{V}_\infty \frac{\partial \hat{w}}{\partial \hat{y}} + \hat{W}_\infty \frac{\partial \hat{w}}{\partial \hat{z}} = -\frac{\partial \Phi}{\partial \hat{z}} \quad (2.18)$$

$$\nabla^2 \Phi = 0 \quad (2.19)$$

The boundary conditions applied in Laplace equation are:

- Aerodynamic loading acts on the rotor blades
- Pressure returns to ambient pressure far from the rotor
- Pressure discontinuity across rotor plane equals to thrust

The solution can be obtained if considering the pressure potential to the sum of a spatially varying potential ( $\Phi^V$ ) and a temporally varying potential ( $\Phi^A$ ), i.e.

$$\Phi = \Phi^V + \Phi^A \quad (2.20)$$

Rewrite momentum balance:

$$\frac{\partial \hat{u}}{\partial \hat{t}} = -\frac{\partial \Phi^A}{\partial \hat{x}}; \hat{U}_\infty \frac{\partial \hat{u}}{\partial \hat{x}} + \hat{V}_\infty \frac{\partial \hat{u}}{\partial \hat{y}} + \hat{W}_\infty \frac{\partial \hat{u}}{\partial \hat{z}} = -\frac{\partial \Phi^V}{\partial \hat{x}} \quad (2.21)$$

$$\frac{\partial \hat{v}}{\partial \hat{t}} = -\frac{\partial \Phi^A}{\partial \hat{y}}; \hat{U}_\infty \frac{\partial \hat{v}}{\partial \hat{x}} + \hat{V}_\infty \frac{\partial \hat{v}}{\partial \hat{y}} + \hat{W}_\infty \frac{\partial \hat{v}}{\partial \hat{z}} = -\frac{\partial \Phi^V}{\partial \hat{y}} \quad (2.22)$$

$$\frac{\partial \hat{w}}{\partial \hat{t}} = -\frac{\partial \Phi^A}{\partial \hat{z}}; \hat{U}_\infty \frac{\partial \hat{w}}{\partial \hat{x}} + \hat{V}_\infty \frac{\partial \hat{w}}{\partial \hat{y}} + \hat{W}_\infty \frac{\partial \hat{w}}{\partial \hat{z}} = -\frac{\partial \Phi^V}{\partial \hat{z}} \quad (2.23)$$

Assuming the differential equations are linear and can be represented by operators  $L$  and  $E$ , one can use Eq. 2.24 and Eq. 2.25 to combine the equations.

$$M = E^{-1} \quad (2.24)$$

$$\hat{u}^* = \frac{\partial \hat{u}}{\partial \hat{t}} \quad (2.25)$$

Governing equation for GDW method becomes:

$$\Phi = L^{-1}[\hat{u}] + M[\hat{u}]^* \quad (2.26)$$

Considering infinite series and linearly independent radial shape functions ( $\psi$ ), a distribution for the induced velocity can be obtained:

$$\hat{u}(\hat{r}, \psi, \hat{t}) = \sum_{r=0}^{\infty} \sum_{j=r+1, r+3, \dots}^{\infty} \phi_j^r(\nu) [\alpha_j^r(\hat{t}) \cos(r\psi) + \beta_j^r(\hat{t}) \sin(r\psi)] \quad (2.27)$$

Without going through the details of the GDW solution procedure, the GDW method can be summarized as [Bachynski \(2015\)](#):

1. The pressure distribution and induced velocity distribution are combined into governing equation.

2. Cosine and sine terms are separated.
3. Pressure coefficients are combined with bladed loading.
4. Matrices are assembled for a certain number of harmonics/flow states.

This project uses both BEM and GDW method in the time-domain analysis (Chapter 5). Figure 2.5 compares the BEM and GDW method. Note that neither method really accounts for large rotor cone or deflections. Furthermore, dynamic stall is applied after angle of attack computation in both methods.

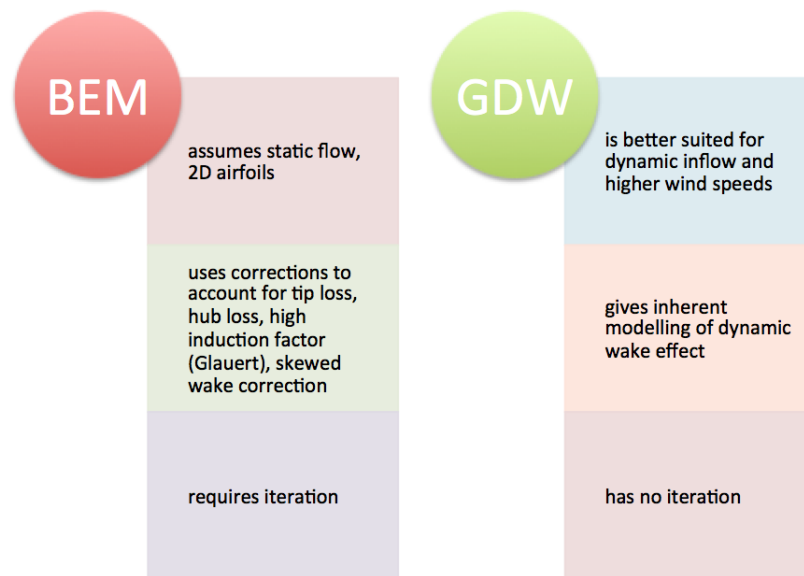


Figure 2.5: Comparison between BEM method and GDW method

### 2.1.4 Corrections

Section 2.1.2 introduces the BEM method in principle. However, it is necessary to apply several corrections to the algorithm in order to get reliable results. These corrections are described in this section.

#### Prandtl's Tip Loss Factor

One of the major limitations of the original BEM theory is that it does not consider the effect of tip loss. It assumes infinite number of blades. As seen in Figure 2.6, air tends to flow around the

tip (following the pressure gradient) from the lower to upper side and these tip vortices create multiple helical structures in the wake [Moriarty and Hansen \(2005\)](#).

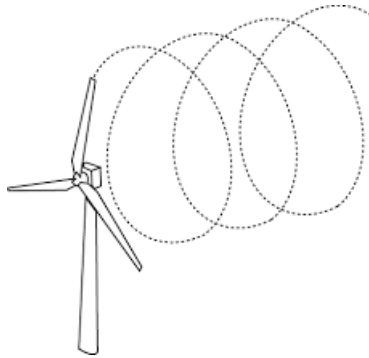


Figure 2.6: Helical wake pattern of single tip vortex [Moriarty and Hansen \(2005\)](#)

Prandtl's tip loss factor corrects the second basic assumption, that the turbines operate with infinite number of blades. It derived a correction factor  $F$  to thrust and torque equations (Eq. 2.4 and Eq. 2.5) [Hansen \(2008\)](#):

$$F = \frac{2}{\pi} \cos^{-1} \left[ \exp\left(-\frac{B(1-r/R)}{2r \sin\phi/R}\right) \right] \quad (2.28)$$

Where  $B$  is the number of blades;  $R$  is the total radius of the rotor;  $r$  is the local radius and  $\phi$  is the flow angle.

This correction factor yields corrected thrust and torque equations:

$$dT = 4\phi r \rho V_0^2 a(1-a)Fdr \quad (2.29)$$

$$dM = 4\pi r^3 \rho V_0 \omega (1-a)a'Fdr \quad (2.30)$$

### Glauert Correction for High Values of $a$

When the axial induction factor  $a$  becomes larger than 0.4, the BEM theory breaks down (See Figure 2.7). This occurs with turbines operating at high tip speed ratios (e.g. constant speed turbine at low wind speeds), as the rotor enters the so-called "turbulent wake state" ( $a > 0.5$ ) [Moriarty and Hansen \(2005\)](#). In this case, the flow behind the rotor slows down, but the thrust on the rotor disk continues increasing. According to BEM theory, this condition happens when

some of the flow in the far wake starts to propagate upstream, but this also violates the second basic assumption.

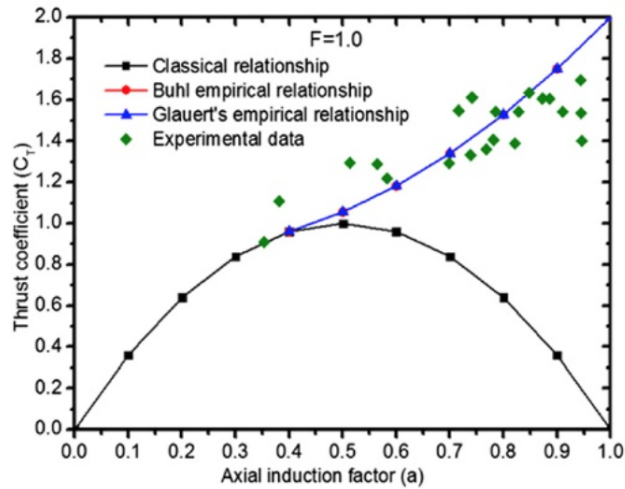


Figure 2.7: Different expressions for the thrust coefficient versus the axial induction factor  $a$  Liu and Janajreh (2012)

To compensate for this effect, Glauert developed a correction based on experimental measurements, which is known as Glauert correction:

$$C_T = \begin{cases} 4a(1-a)F, & \text{for } a \leq \frac{1}{3} \\ 4a(1 - \frac{1}{4}(5-3a)a)F, & \text{for } a > \frac{1}{3} \end{cases} \quad (2.31)$$

$$C_T = \begin{cases} 4a(1-a)F, & \text{for } a \leq \frac{1}{3} \\ 4a(1 - \frac{1}{4}(5-3a)a)F, & \text{for } a > \frac{1}{3} \end{cases} \quad (2.32)$$

### Dynamic Inflow/Wake

The BEM procedure can be considered as quasi-static: the induction factor or the output will immediately be updated if there is a change in the incoming wind speed, blade pitch angle or rotor speed Bachynski (2015). However, the wind turbines take some time to react these updates in practice (See Figure 2.8). This "Dynamic wake effect" is actually the time delay in the induced velocities due to the shedding and downstream convection of velocity Hansen (2008). This effect can be included in the BEM code by applying the "Stig Øye dynamic inflow model", which will act as a filter for induced velocities as shown in Eq. 2.33 and Eq. 2.34 Snel et al. (1995). An alternative approach for including this effect is using GDW theory to compute the aerodynamic forces.

$$W + \tau_2 \frac{dW}{DT} = W_{int} \quad (2.33)$$

$$W_{int} + \tau_1 \frac{dW_{int}}{dt} = W_{qs} + 0.6\tau_1 \frac{dW_{qs}}{dt} \quad (2.34)$$

Where  $W_{qs}$  is the quasi static induced velocity vector;  $W$  is the new induced velocity vector;  $\tau_1$  and  $\tau_2$  are time constants.

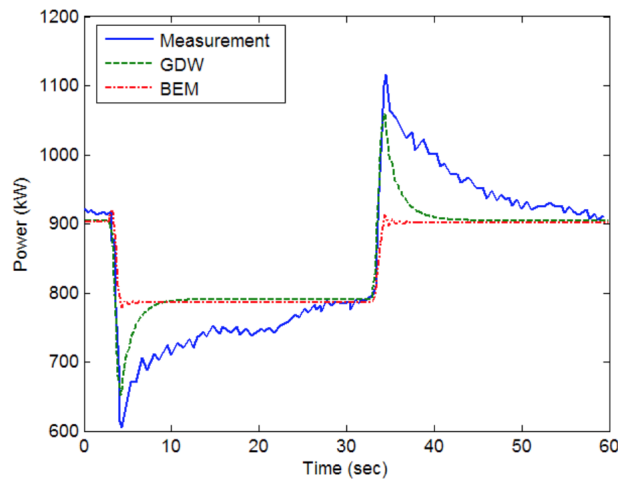


Figure 2.8: Generator power output during rapid pitch changes (from  $0.2^\circ$  to  $3.9^\circ$  and back) for the Tjæreborg turbine, Suzuki (2009) Moriarty and Hansen (2005)

### Dynamic Stall

In fact, the drag and lift coefficients ( $C_d$  and  $C_l$ ) input to BEM can be described as static lift and drag curves for given angle of attack (Figure 2.9). Nonetheless, in the real case of changing the angle of attack, there can be sudden attachment and re-attachment of flow such that the coefficients do not strictly follow the static curves. The effect of changing the angle will not appear instantaneously on the coefficient. An vital consequence of the dynamic stall effect is that transient loads maybe large, since the blade may still experience a high lift coefficient after a sudden increase of wind speed Bachynski (2015). There are several approaches for modeling the dynamic stall effects, such as Stig Øye model (1991) used in HAWC2/Riflex BEM and Beddoes-Leishman model (1989) used in AeroDyn Hansen (2008).

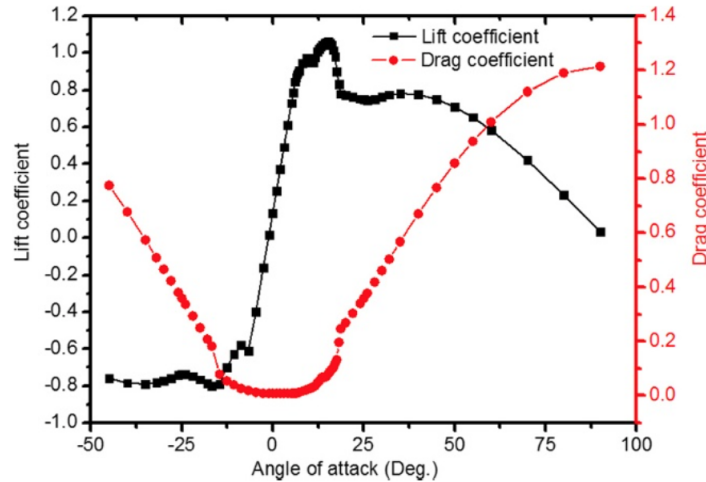


Figure 2.9: Lift and drag coefficient versus different angle of attack based [Lindenburg \(2003\)](#)

The Stig Øye model gives unsteady lift coefficient by filtering the trailing edge separation point with an empirical time constant [Hansen \(2008\)](#). Øye recommends to include a dynamic stall model for the lift so that the degrees of stall  $f_s$  is introduced.

For flow that is not fully stalled, the lift coefficient is computed as:

$$C_L = \frac{1}{4} \frac{dC_L}{d\alpha} (\alpha - \alpha_0) (a + \sqrt{1 - |f_s|})^2 \quad (2.35)$$

Where  $f_s$  is degrees of stall;  $\frac{dC_L}{d\alpha}$  is computed at the full-stall limit (depending on the sign of  $\alpha$ );  $\alpha_0$  is the angle of attack where the lift is zero.

While for fully stalled flow:

$$C_L = C_{L,q_s} (1 + \sqrt{1 - |f_s|})^2 \quad (2.36)$$

Where  $C_{L,q_s}$  is the quasi-static lift.

The Beddoes-Leishman model further takes into account attached flow and also corrects the drag and moment coefficients [Hansen \(2008\)](#). Figure 2.10 shows an example of the result using a dynamic stall model. There is an overshoot in lift, which benefits a rotor in maneuver [Bousman \(2009\)](#).

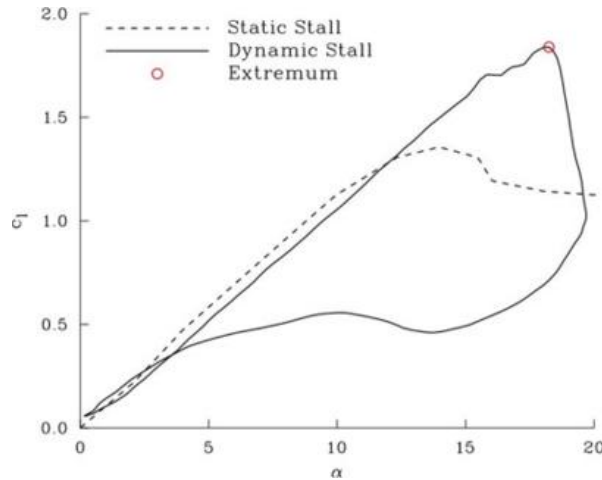


Figure 2.10: Comparison between dynamic stall and static stall [Bousman \(2009\)](#)

### Yaw/Tilt Model

When the rotor is yawed and/or tilted, there will be an azimuthal variation of the induced velocity, leading to higher induced velocity for the blade pointing upstream than that for the blade pointing downstream (Figure 2.11). This is because a blade pointing downstream is deeper into the wake than a blade pointing upstream [Hansen \(2008\)](#). The yaw model describes the distribution of induced velocity. Thus it is impossible for a BEM model without including yaw model to predict the restoring yaw moment.

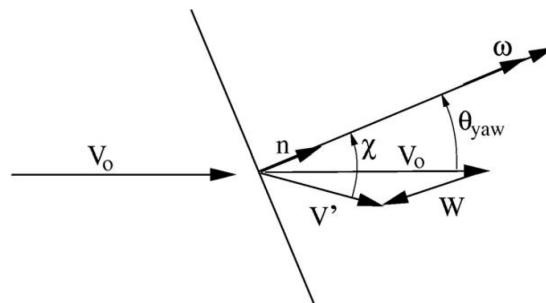


Figure 2.11: Yawed rotor disc in wind field [Hansen \(2008\)](#)

Glauert model originates from helicopter theory and uses the wake skew angle rather than the rotor yaw angle in order to correct the induced velocity [Boorsma \(2012\)](#):

$$\mathbf{W} = \mathbf{W}_0 \left( 1 + \frac{r}{R} \tan\left(\frac{\chi}{2}\right) \cos(\theta_{wing} - \theta_0) \right) \quad (2.37)$$



Where the wake skew angle  $\chi$  is the angle between the wind velocity in the wake and the rotational axis of the rotor, see Figure 2.11.  $\mathbf{W}_0$  is the mean induced velocity and  $\theta_0$  is the angle where the blade is deepest into the wake.

The induced velocity is known now and the angle of attack can also be calculated. The lift, drag and moment coefficients can be found easily by looking up relative tables. Then the normal and tangential loads,  $p_z$  and  $p_y$  are:

$$p_z = L \cos \phi + D \sin \phi \quad (2.38)$$

$$p_y = L \sin \phi - D \cos \phi \quad (2.39)$$

Where:

$$L = \frac{1}{2} \rho |V_{rel}|^2 c C_l \quad (2.40)$$

$$D = \frac{1}{2} \rho |V_{rel}|^2 c C_d \quad (2.41)$$

## 2.2 Wave Loads on Slender Structures

### 2.2.1 Morison's Equation

Both potential flow effects and viscous effects are vital in determining the wave-induced loads on offshore structures. However, potential flow theory is normally applied to large structures while Morison's equation is often used to calculate wave loads on slender structures when viscous force matters, i.e. in long wave conditions ( $\lambda > 5D$ ). Figure 2.12 shows that the mass forces dominate in small and moderate waves, while the viscous forces dominate in extreme waves.

Eq. 2.42 represents the Morison's equation for a fixed structure [Faltinsen \(1993\)](#):

$$F = \rho(1 + C_A) A a + \frac{1}{2} \rho C_D D |u| u \quad (2.42)$$

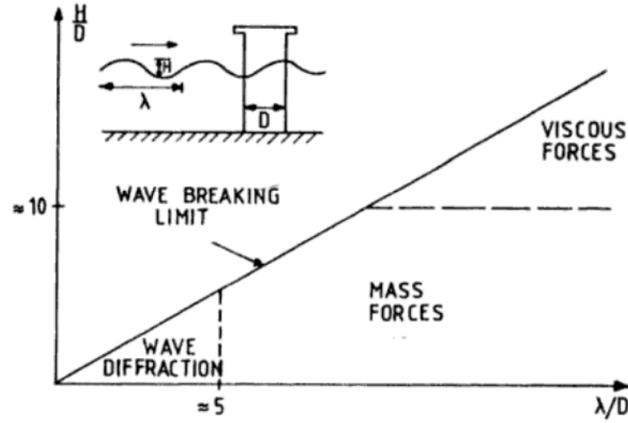


Figure 2.12: Relative importance of mass, viscous drag and diffraction forces on marine structures [Faltinsen \(1993\)](#)

Positive force direction,  $F$ , is in the wave propagation direction;  $\rho$  is the density of sea water;  $A$  is the wetted surface area;  $u$  and  $a$  are the horizontal undisturbed fluid velocity and acceleration at the midpoint of the strip;  $C_A$  are denoted as non-dimensional added mass coefficient;  $C_D$  as non-dimensional drag coefficient;  $(1 + C_A)$  defines the mass coefficient  $C_M$ .

In the case of a moving structure, denoting the horizontal rigid body motion by  $\eta_1$ , the Morison's equation can be modified as:

$$F = -\rho A C_A \ddot{\eta}_1 + \rho A (1 + C_A) a + \frac{1}{2} \rho C_D D |u - \dot{\eta}_1| (u - \dot{\eta}_1) \quad (2.43)$$

Where  $u - \dot{\eta}_1$  represents the relative velocity between the moving structure and fluid velocity.

The second part in Eq. 2.42 and Eq. 2.43 represent drag force, that is the main source of viscous damping. The viscous damping could reduce the amplitude of platforms' motions. This is checked in Section 4.3.3. It can be seen from Eq. 2.42 and Eq. 2.43 that the drag force is a quadratic function of the relative velocity and hence linearization is required for that application of drag force in frequency domain analysis.

If the response of the structure is harmonic, the wave velocity can be given by:

$$\eta = \eta_1 \cos(\omega t) + \eta_2 \sin(\omega t) \quad (2.44)$$

Then the linearized drag force can be represented by:

$$dF_{drag,L} = \frac{4\rho C_D D A}{3\pi} (u - \dot{\eta}_1) \quad (2.45)$$

The viscous damping coefficient from linearized drag force is:

$$B_{viscous} = \frac{4\rho C_D D A}{3\pi} \quad (2.46)$$

Where A is given by:

$$A = \sqrt{(u - \omega \eta_2)^2 + (\omega \eta_1)^2} \quad (2.47)$$

It can be seen that  $A$  depends on the motions of the structure, and thus the viscous damping also depends on platform motions.

### 2.2.2 Hydrodynamic Coefficients

The drag coefficient  $C_D$  is non-dimensional drag force, defined as Eq. 2.48 DNV (2014b). In general, the drag force is in the composite direction of the fluid velocity and can be decomposed in a normal force  $f_N$  and a tangential force  $f_T$  (Figure 2.13).

$$C_D = \frac{f_{drag}}{1/2\rho D v^2} \quad (2.48)$$

Where  $f_{drag}$  = sectional drag force [ $N/m$ ];  $\rho$  = fluid density [ $kg/m^3$ ];  $D$  = diameter (or typical dimension) [ $m$ ];  $v$  = velocity [ $m/s$ ].

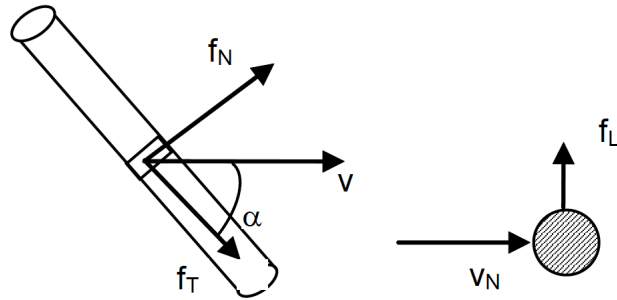


Figure 2.13: Definition of normal force, tangential force and lift force on a slender structure [DNV \(2014b\)](#)

The added mass coefficient  $C_A$  is non-dimensional added mass [DNV \(2014b\)](#):

$$C_A = \frac{m_a}{\rho A} \quad (2.49)$$

Where  $m_a$  = the added mass per unit length [ $kg/m$ ];  $A$  = cross-sectional area [ $m^2$ ].

The added mass  $C_A$  and drag coefficients  $C_D$  have to be determined empirically, depending on Reynolds number, KC number and non-dimensional roughness number:

- Reynolds number:  $Re = VD/\nu$
- KC number:  $Kc = V_m T/D$
- Non-dimensional roughness:  $\Delta = k/D$

Where  $D$  is diameter;  $V$  is flow velocity;  $V_m$  is maximum water particle velocity;  $T$  is wave period;  $k$  is roughness height;  $\nu$  is fluid kinematic viscosity.

Figure 2.14 shows an example for the variation of drag coefficient  $C_D$  and mass coefficient  $C_M$ . The coefficients are calculated during sinusoidal oscillation of a cylinder for various KC numbers. When  $KC > 30$ ,  $C_D$  tends to be 1.5 while  $C_M$  tends to be 1.2 approximately.

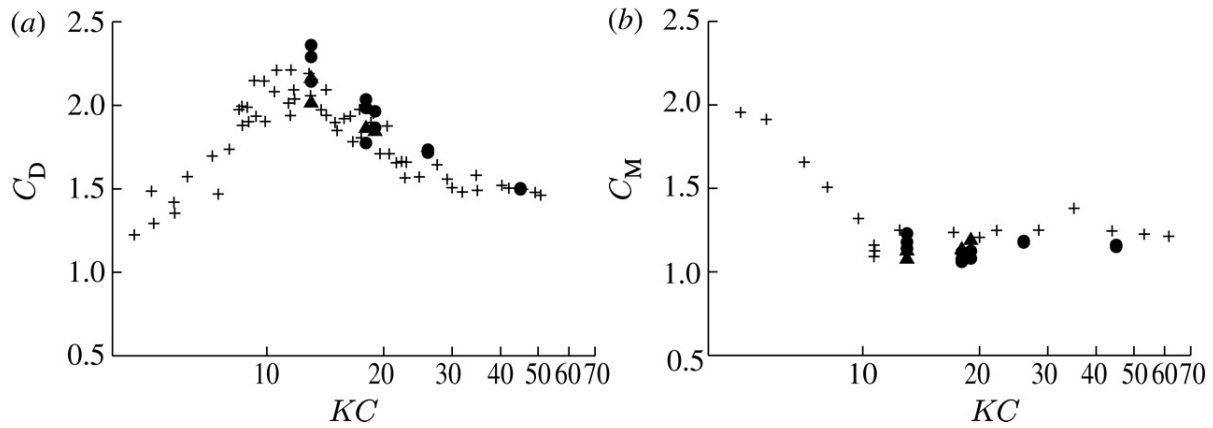


Figure 2.14: Calculated drag and mass coefficients due to planar oscillation compared with experimental data [Obasaju et al. \(1988\)](#)

## 2.3 Wave Loads on Large Volume Structures

### 2.3.1 First-order Potential Flow Theory

The first-order potential flow theory is a linear solution, in which both the free-surface condition and the body boundary condition are defined in the mean position of the free-surface and the submerged hull surface respectively. Further, the fluid pressure and the velocity of fluid particles on the free-surface are linearized [Faltinsen \(1993\)](#). In the first-order theory, the sea water is assumed incompressible, inviscid and irrotational. Additionally, the floater is assumed as a rigid body. Thus the velocity potential  $\phi$  can be solved by the Laplace equation (Eq 2.50) with relevant boundary conditions in the fluid.

$$\frac{\partial^2 \phi}{\partial x^2} + \frac{\partial^2 \phi}{\partial y^2} + \frac{\partial^2 \phi}{\partial z^2} = 0 \quad (2.50)$$

The following boundary conditions have to imposed:

- Sea bottom boundary condition (i.e. the boundary condition on  $S_{SB}$  in Figure 2.15):

$$\frac{\partial \phi}{\partial n} = 0 \quad (2.51)$$

- Body surface boundary condition (i.e. the boundary condition on  $S_B$  in Figure 2.15):

$$\frac{\partial \phi}{\partial n} = \mathbf{U} \cdot \mathbf{n} \quad (2.52)$$

- Free surface boundary condition (i.e. the boundary condition on  $S_{FS}$  in Figure 2.15):

$$\frac{\partial^2 \phi}{\partial t^2} + g \frac{\partial \phi}{\partial z} = 0 \quad (2.53)$$

- Infinite distance boundary condition (i.e. the boundary condition on  $S_{-\infty}$  and  $S_{\infty}$ ):

$$\frac{\partial \phi}{\partial n} = 0 \quad (2.54)$$

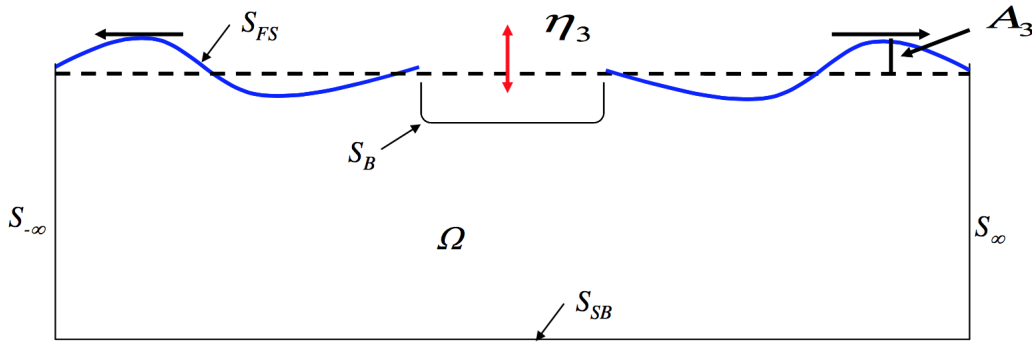


Figure 2.15: Linear wave body interactions problem Greco (2012)

Referring to Figure 2.15,  $\mathbf{n}$  is a normal vector pointing to the fluid;  $S_{SB}$  is the sea bottom surface;  $S_B$  is the body surface;  $S_{FS}$  is the wave free surface;  $S_{-\infty}$  and  $S_{\infty}$  are the boundaries in infinite distance from the body;  $\Omega$  is the mean fluid volume;  $\mathbf{U}$  denotes the body velocity.

According to the potential flow theory Faltinsen (1993), the equation of a platform motion is given as:

$$\sum_{k=1}^6 [(M_{jk} + A_{jk})\ddot{\eta}_k + B_{jk}\dot{\eta}_k + (C_{jk} + K_{jk})\eta_k] = F_j e^{-i\omega_0 t}, (j = 1, 2, 3, 4, 5, 6) \quad (2.55)$$

Where  $M_{jk}$  are the components of the mass matrix for the structure, which contain the struc-

tural mass and mass moment of inertia;  $A_{jk}$  are the components of the added mass matrix;  $B_{jk}$  are the components of the damping matrix;  $C_{jk}$  are the components of the restoring matrix. Note the restoring matrix can be split into hydrostatic and tendon system parts for the TLPWT. Indeed, the mooring system stiffness should be much larger than the hydrodynamic stiffness during operation; on the contrary, during installation, the hydrostatic stiffness determines the stability of the freely floating platform [Bachynski \(2014\)](#). Moreover,  $\eta$ ,  $\dot{\eta}$  and  $\ddot{\eta}$  are the response displacement, velocity and acceleration respectively.  $F_j$  are the complex amplitudes of the exciting forces and moments. The force and moment components are given by the real part of  $F_j e^{-i\omega_0 t}$ .

Since the TLP floater has six DOF (surge, sway, heave, roll, pitch and yaw), all the matrixes  $\mathbf{M}$ ,  $\mathbf{A}$ ,  $\mathbf{B}$ ,  $\mathbf{C}$  and  $\mathbf{K}$  should be  $6 \times 6$  matrixes. Actually, the added mass and damping coefficients ( $\mathbf{A}$  and  $\mathbf{B}$ ) show a strong frequency dependence [Faltinsen \(1993\)](#). For example, the added mass in heave for a surface-piercing two-dimensional body in deep water goes logarithmically to infinity when  $\omega \rightarrow \infty$ .

The hydrodynamic problem in regular waves normally deals with two sub-problems [Faltinsen \(1993\)](#):

- Diffraction problem: when the body is fixed and interacting with regular waves, with regarding to wave excitation loads.
- Radiation problem: when the body is forced to oscillate and no incident waves, with regarding to added mass, damping and restoring loads.

If the body is assumed as a small volume structure, which means  $\lambda > 5D$  for a vertical cylinder, the excitation force can be written as:

$$\mathbf{F} = \mathbf{i}F_1 + \mathbf{j}F_2 + \mathbf{k}F_3 \quad (2.56)$$

where

$$F_i = - \iint_S p n_i ds + A_{i1} a_1 + A_{i2} a_2 + A_{i3} a_3 \quad (2.57)$$

Where  $p$  is the pressure in the undisturbed wave field and  $n = (n_1, n_2, n_3)$  is the unit vector normal to the body surface defined to be positive into the fluid. The integration is over the average wetted surface of the body. In addition,  $a_1, a_2$  and  $a_3$  are acceleration components along the  $x$ -,  $y$ - and  $z$ - axes of the undisturbed wave field and are to be evaluated at the geometrical mass centre of the body. When the wave length is large relative to TLP cross section length (e.g.  $\frac{\lambda}{D} > 5$ ), Eq. 2.57 is often used with strip theory together to predict wave excitation forces [Faltinsen \(1993\)](#). The response of the first order problem has zero mean value and oscillate with the frequency of the incident waves, i.e. superposition principle is valid.

### Added Mass and Moments

Assuming there is no interaction, the added mass can be estimated by summing the 2D cross sectional properties of the submerged parts of the main hull and spokes. Newman provided the added mass coefficients for 2D bodies by using conformal mapping techniques [Newman \(1977\)](#), see Figure 2.16.  $m_{11}$  corresponds to longitudinal acceleration;  $m_{22}$  to lateral acceleration in equatorial plane;  $m_{66}$  denotes the rotational added moment of inertia.

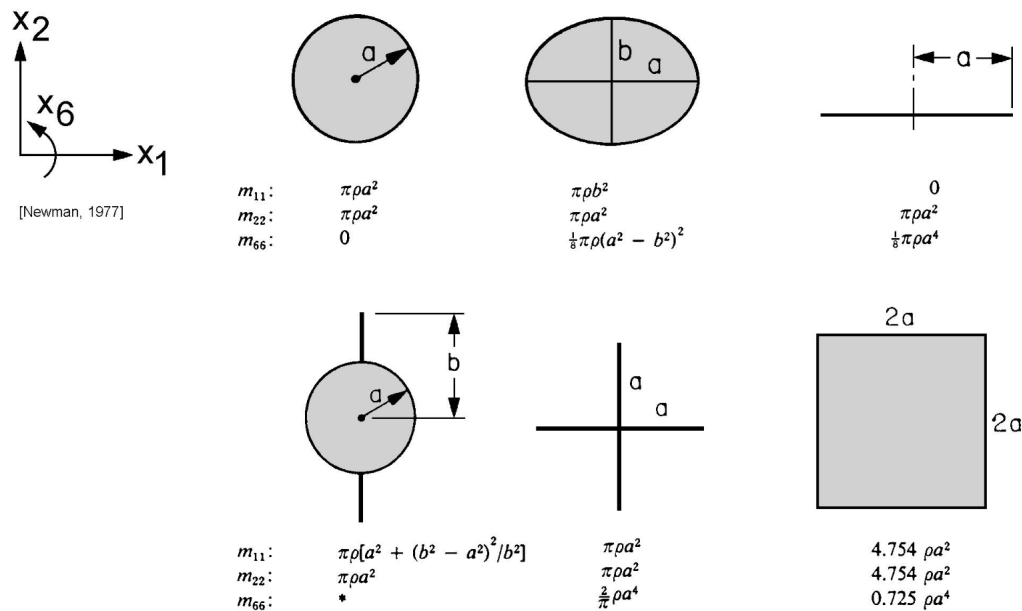


Figure 2.16: Added mass coefficients of 2D bodies [Newman \(1977\)](#)

According to the equations given in Figure 2.16, the transverse added mass per unit length



( $a_t$ ) for the central cylinders is:

$$a_t[D] = \rho\pi \frac{D^2}{4} \quad (2.58)$$

While Eq 2.59 can be employed for the square section of the spokes with side length  $h$ .

$$a_t[h] = 4.754\rho\left(\frac{h}{2}\right)^2 \quad (2.59)$$

Based on Eq 2.58 and Eq 2.59, the surge, heave, pitch and yaw added mass contributions for the TLP floater can be simplified by Eq 2.60 - 2.64 respectively.

$$A_{11} = a_t[D_1](h_1 - b_t) + a_t[D_2]h_2 + \sum_{i=1}^{n_p} l_p a_t[h_p] \cos^2(\theta_i) \quad (2.60)$$

$$A_{33} = \rho\pi \frac{1}{12} D_2^3 + \sum_{i=1}^{n_p} l_p a_t[w_p] \quad (2.61)$$

$$\begin{aligned} A_{55} = & a_t[D_1](h_1 - b_t)\left(\frac{1}{12}(h_1 - b_t)^2 + \left(\frac{1}{2}(h_1 - b_t)\right)^2\right) + a_t[D_2]h_2\left(\frac{1}{12}h_2^2 + \left(\frac{1}{2}(-2T + h_2)\right)^2\right) \\ & + \sum_{i=1}^{n_p} \left(\frac{1}{3}(r_p^3 - D_2^3)\right) a_t[w_p] \cos^2(\theta_i) + \sum_{i=1}^{n_p} (z_s^2 l_p a_t[h_p]) \sin^2(\theta_i) \end{aligned} \quad (2.62)$$

$$A_{51} = -\frac{1}{2}(h_1 - b_t)^2 a_t[D_1] - \frac{1}{2}(T^2 - (-T + h_2)^2) a_t[D_2] + \sum_{i=1}^{n_p} z_s l_p a_t[h_p] \sin^2(\theta_i) \quad (2.63)$$

$$A_{66} = \sum_{i=1}^{n_p} \frac{1}{3} a_t[w_p] \left(l_p^3 - \frac{D_2^3}{2}\right) \quad (2.64)$$

Where  $\theta_i$  is the angle of pontoons distribution along the z-axis. The angles for the three spokes of the TLPWT equal to  $0^\circ$ ,  $120^\circ$  and  $240^\circ$  respectively.

### Restoring Stiffness

When a body is freely floating, the restoring forces and moments follows from the hydrostatic and mass consideration. Then the restoring forces and moments can be represented by:

$$F_k = -C_{kj}\eta_j \quad (2.65)$$

where stiffness coefficient  $C_{kj}$  stands for the effects from the motion  $\eta_j$  on the force  $F_k$ .

Eq 2.66-2.69 below give the non-zero terms in the hydrostatic stiffness matrix for a body with x-z symmetry.

$$C_{33} = \rho g A_{wp} \quad (2.66)$$

$$C_{35} = C_{53} = -\rho g \iint_{A_{wp}} x ds \quad (2.67)$$

$$C_{44} = \rho g V(z_B - z_G) + \rho g \iint_{A_{wp}} y^2 ds \quad (2.68)$$

$$C_{55} = \rho g V(z_B - z_G) + \rho g \iint_{A_{wp}} x^2 ds \quad (2.69)$$

Where  $A_{wp}$  is the water plane area;  $V$  is the displaced volume of water;  $z_G$  and  $z_B$  are the z-coordinates of the center of gravity and center of buoyancy respectively. Because of the symmetry of the TLP floater, the integration of  $x$  around the water plane area equals to zero. That means  $C_{35}$  and  $C_{53}$  are zeroes.

$$C_{35} = C_{53} = 0 \quad (2.70)$$

Even though Eq 2.66 - 2.70 are valid for infinitesimally small motions theoretically, it has been proven that they are reasonable approximations for the studied motions [Bachynski \(2014\)](#).

### Tendon Stiffness

The tendons employed by the TLP floater are three steel pipes. Assuming these pipes remain straight, one can get the following tendon stiffness coefficients (Eq 2.71 - Eq 2.75).

$$K_{11} = \sum_{j=1}^{n_t} \frac{F_t}{l_0} \quad (2.71)$$

$$K_{33} = \sum_{j=1}^{n_t} \frac{EA}{l_0} \quad (2.72)$$

$$K_{51} = K_{15} = \sum_{j=1}^{n_t} \frac{F_t}{l_0} z_s \quad (2.73)$$

$$K_{55} = \sum_{j=1}^{n_t} \left[ \frac{F_t}{l_0} z_s^2 + \frac{EA}{l_0} r_p^2 \right] \cos^2(\theta_j) \quad (2.74)$$

$$K_{66} = \sum_{j=1}^{n_t} \frac{F_t}{l_0} r_p^2 \quad (2.75)$$

Where  $\theta_i$  denotes the angle of the tendons distribution along the z-axis. The angle of the three tendons of the TLPWT are  $0^\circ$ ,  $120^\circ$  and  $240^\circ$  respectively.  $n_t$  represents the number of tendons.

Since the structure is symmetric along the xz-plane, one can get:

$$K_{22} = K_{11} \quad (2.76)$$

$$K_{24} = K_{42} = -K - 51 \quad (2.77)$$

$$K_{44} = K_{55} \quad (2.78)$$

### Natural Periods Estimation

The TLPWT is assumed as a rigid body with six degrees of freedom. The natural periods in surge, sway and heave motion can be estimated by Eq. 2.79 - Eq. 2.81 respectively if the surge, sway or heave motion is assumed as uncoupled from other rigid-body motions.

$$T_{11} = 2\pi \sqrt{\frac{M_{11} + A_{11}}{K_{11}}} \quad (2.79)$$

$$T_{22} = T_{11} \quad (2.80)$$

$$T_{33} = 2\pi \sqrt{\frac{M_{33} + A_{33}}{C_{33} + K_{33}}} \quad (2.81)$$

And the natural periods in pitch, roll and yaw are given by:

$$T_{44} = T_{55} = 2\pi \sqrt{\frac{M_{55} + A_{55}}{C_{55} + K_{55}}} \quad (2.82)$$

$$T_{66} = 2\pi \sqrt{\frac{M_{66} + A_{66}}{K_{66}}} \quad (2.83)$$

### 2.3.2 Second-order Potential Flow Theory

Floater motions are commonly split into difference-frequency, mean-frequency and sum-frequency motion components. The difference-frequency and mean-frequency motions are mainly dominated by inviscid fluid effects, while the sum-frequency motions are governed by viscous effects [DNV \(2010a\)](#). Various offshore type structures are sensitive to different hydrodynamic effects. Table 2.1 gives an overview of these load effects. It can be seen that TLP structures are very sensitive to sum-frequency loads, different from other structures. Actually, the 'Springing' phenomenon is just excited by sum-frequency forces. Additionally, the mean-frequency and difference-frequency motions are also of importance to a TLP structure. Mean and difference-frequency wave loads are of importance for all offshore structures, such as the design of mooring and thruster systems, analysis of offshore loading systems, added resistance of ships in waves

and so on [Faltinsen \(1993\)](#). In this section, the second-order wave loads, difference-frequency and sum-frequency wave forces, are reviewed. Generally, there are two common methods for second order wave loads, i.e. direct pressure integration and conservation of fluid momentum.

Table 2.1: Hydrodynamic effects of importance for each floater [DNV \(2010a\)](#)

	FPSO	Semi-submersible	DDF	TLP
Wave frequency loads	×	×	×	×
Low frequency loads	×	×	×	×
Loads in moonpool	×		×	
Mathieu instability			×	
Hull vortex shedding			×	
Wave in deck loads		×	×	×
Slamming loads	×	×		×
Green water loads	×			
High frequency loads				×

The most common method for solving second order problem in ship and offshore dynamics is to use perturbation analysis with the wave amplitude as a small parameter. Assuming potential theory, the problem is solved to second-order in incident wave amplitude [Faltinsen \(1993\)](#).

A simple way to illustrate the presence of the non-linear wave effects is to consider the quadratic velocity term in Bernoulli's equation for the fluid pressure:

$$-\frac{\rho}{2}(V_1^2 + V_2^2 + V_3^2) = -\frac{\rho}{2} |\nabla\Phi|^2 \quad (2.84)$$

where  $\mathbf{V} = (V_1, V_2, V_3)$  is the fluid velocity vector.

Considering an idealized sea state consisting of two wave components of circular frequencies  $\omega_1$  and  $\omega_2$ , the x-component velocity can be written formally as:

$$V_1 = A_1 \cos(\omega_1 t + \epsilon_1) + A_2 \cos(\omega_2 t + \epsilon_2) \quad (2.85)$$

By substituting Eq. 2.85 into Eq. 2.84, it now becomes:

$$\begin{aligned}
-\frac{\rho}{2}V_1^2 = &-\frac{\rho}{2}\left[\frac{A_1^2}{2} + \frac{A_2^2}{2} + \frac{A_1^2}{2}\cos(2\omega_1 t + 2\epsilon_1) + \frac{A_2^2}{2}\cos(2\omega_2 t + 2\epsilon_2)\right. \\
&+ A_1 A_2 \cos[(\omega_1 - \omega_2)t + \epsilon_1 - \epsilon_2] + A_1 A_2 \cos[(\omega_1 + \omega_2)t + \epsilon_1 + \epsilon_2]]
\end{aligned} \tag{2.86}$$

Eq. 2.86 states that the second-order effects cause the following forces:

- mean drift forces → the constant term  $-0.5\rho(A_1^2/2 + A_2^2/2)$
- difference-frequency forces → the pressure term oscillating with frequency  $(\omega_i - \omega_j)$
- sum frequency forces → the pressure term oscillating with frequency  $(\omega_i + \omega_j)$

Where  $i$  and  $j$  can be 1 or 2 randomly. The QTF for second-order loads depends on first-order motions  $x_{wa}$  and the direction of propagation  $\beta_i$  of the wave components.

### Difference-frequency Force

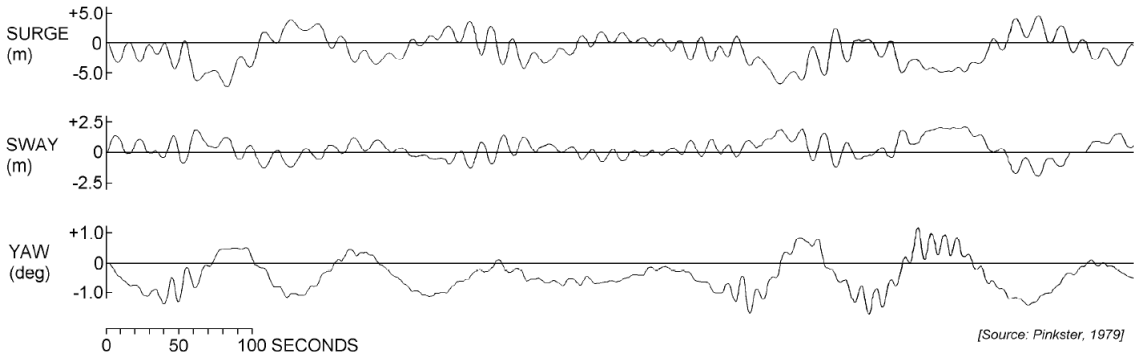


Figure 2.17: Surge, sway and yaw motions of a TLP in irregular seas

Difference-frequency forces may excite slow drift motions. Due to low damping, large motions occur. Figure 2.17 gives an example of slow drift horizontal motions of a TLP in irregular waves coming at an angle to the longitudinal axial of the platform. The low frequency components in all the three motions are clear. A general formula for the slow drift excitation loads is:

$$F_i^{SV} = \sum_{j=1}^N \sum_{k=1}^N A_j A_k [T_{jk}^{ic} \cos[(\omega_k - \omega_j)t + (\epsilon_k - \epsilon_j)] + T_{jk}^{is} \sin[(\omega_k - \omega_j)t + (\epsilon_k - \epsilon_j)]] \tag{2.87}$$

Where the wave amplitudes  $A_i$ , wave frequencies  $\omega_i$ , random phase angles  $\epsilon_i$ , and number of wave components  $N$  are explained by the velocity potential given by Equation 2.88 in irregular sea:

$$\phi^I = \sum_{j=1}^N \frac{gA_i}{\omega_i} e^{k_j z} \cos(\omega_j t - k_j x \cos\beta - k_j y \sin\beta + \epsilon_j) \quad (2.88)$$

Moreover,  $F_1^{SV}$ ,  $F_2^{SV}$  and  $F_3^{SV}$  are respectively x-, y- and z-components of the slow-drift forces, while  $F_4^{SV}$ ,  $F_5^{SV}$  and  $F_6^{SV}$  stands for the moments about the x-, y- and z-axes. Furthermore, the coefficients  $T_{jk}^{ic}$  and  $T_{jk}^{is}$  represent the second-order transfer functions for the difference-frequency loads. These two coefficients are independent of the wave amplitudes  $A_i$ , but dependent on wave frequencies  $\omega_j$  and  $\omega_k$  DNV (2010a).

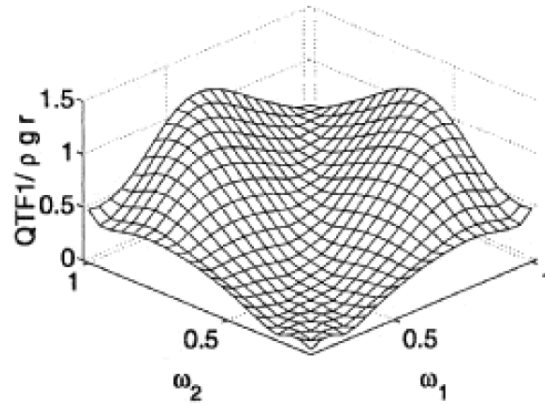


Figure 2.18: Surge difference-frequency quadratic transfer function (QTF) for 228m classical Spar, From Haslum (1999) DNV (2010a)

In general all frequencies in the  $w_i w_j$ -plane may contribute to the second-order difference frequency wave forces  $F_i^{SV}$ . An example is shown in Figure 2.18. As the second-order wave forces are usually small, their most important contribution is in the vicinity of resonance. When the resulting difference-frequency equals to natural frequency of the offshore structure  $w_n$ , the two lines in the  $w_i w_j$ -plane are:

$$w_i = w_j + w_n \quad (2.89)$$

If the natural frequency of the structure  $w_n$  is extremely low, it can be obtained that  $w_i = w_j$  from Eq. 2.89. One can then take advantage of Newman's approximation, which states that  $T_{jk}^{ic}$  and  $T_{jk}^{is}$  can be approximated by  $T_{jj}^{ic}$ ,  $T_{kk}^{ic}$ ,  $T_{jj}^{is}$  and  $T_{kk}^{is}$  Faltinsen (1993):

$$\begin{aligned} T_{jk}^{ic} = T_{kj}^{ic} &= 0.5(T_{jj}^{ic} + T_{kk}^{ic}); \\ T_{jk}^{is} = T_{kj}^{is} &= 0 \end{aligned} \quad (2.90)$$

Furthermore, by approximating the double summation by the square of a single series, Eq. 2.87 can be simplified to:

$$F_i^{SV} = 2 \left[ \sum_{j=1}^N A_j (T_{jj}^{ic})^{1/2} \cos(\omega_j t + \epsilon_j) \right]^2 \quad (2.91)$$

Obviously, using Eq. 2.91 to calculate the slow-drift forces reduces the computation time significantly comparing to Eq. 2.87. A linear analysis is sufficient for this calculation. Besides, the transfer functions  $T_{jj}^{ic}$  and  $T_{kk}^{ic}$  can be calculated from first-order velocity potential alone, thus there is no need to calculate the second-order velocity potential.

### Sum-frequency Force

Following the discussion about Eq. 2.86, there are non-linear effects due to the quadratic velocity term in Bernoulli's equation, that may create excitation forces with higher frequencies than the dominant wave frequencies, such as  $2\omega_1$ ,  $2\omega_2$  and  $\omega_1 + \omega_2$ . For TLPs, the second-order wave forces in a random sea-state oscillating at the sum-frequencies  $w_i + w_j$  excite resonant response in heave, pitch and roll. The typical resonance periods are in the range of 2 – 5s. Usually the waves in this range do not carry enough energy to excite resonance. However, the TLPs maybe excited by the waves of periods  $2T_n$ ,  $3T_n$  etc, which carries sufficient energy DNV (2010a). The high-frequency stationary time-harmonic oscillation a TLP is referred to 'Springing'. In general the sum-frequency pressure effects decay exponentially. When there is only small difference between frequencies, the sum-frequency pressure decays slowly Bachynski (2014).

It should be noted that the contribution from the quadratic velocity in Bernoulli's equation



to the sum-frequency heave forces for a TLP is normally small. It is the spokes and the bottom of the central column that contributes to the vertical force on the TLP. Indeed, the most important cause to vertical sum-frequency force on a TLP is the second-harmonic component of the second-order potential velocity [Kim and Yue \(1988\)](#). The second potential  $\phi_2$  must follow from solving a boundary value problem with inhomogeneous free-surface condition [Faltinsen \(1993\)](#):

$$\phi_{2u} + g\phi_{2z} = -\frac{\partial}{\partial t}(\phi_{1x}^2 + \phi_{1y}^2 + \phi_{1z}^2) + \frac{1}{g}\phi_{1t}\frac{\partial}{\partial z}(\phi_{1u} + g\phi_{1z}) \quad (2.92)$$

Eq. 2.92 is for calculating the sum-frequency force on the free surface, i.e.  $z = 0$ . Where the index 1 denotes first-order potential and 2 denotes second-order potential. The free surface forcing term decreases slowly along with the distance away from the main structure and includes products of highly oscillatory terms [Kim and Yue \(1988\)](#). From this perspective, it is necessary to apply a proper discretization of the free surface and its extension. The combination between the contribution of the quadratic velocity term in Bernoulli's due to the first-order potential and the solution of the second-order boundary problem will provide sum-frequency QTF, which is a function of frequency-pairs.

So the most vital aspects to be considered for the calculation of sum-frequency force include:

- Discretization of wetted floater surface geometry
- Discretization of free surface
- Number of frequency pairs in the QTF matrix
- Damping level for the tendon axial response

## 2.4 Wave-induced Response of Floating Structures

### 2.4.1 Frequency Domain Analysis

The frequency-domain refers to the analysis of mathematical functions respect to frequency. The wave induced loads in irregular sea can be obtained by linearly superposing loads due to

regular wave components [DNV \(2014b\)](#).

Assuming a constant amplitude harmonic input given by [Newland \(1993\)](#):

$$x(t) = x_0 e^{i\omega t} \quad (2.93)$$

is applied to a linear system, the corresponding output  $y(t)$  will be given by:

$$y(t) = H(\omega) x_0 e^{i\omega t} \quad (2.94)$$

Where  $H(\omega)$  is the system's complex frequency response function evaluated at the angular frequency  $\omega$ . It defined by:

$$H(\omega) = A(\omega) - iB(\omega) = \sqrt{A^2 + B^2} e^{-i \arctan(B/A)} \quad (2.95)$$

Indeed,  $\sqrt{A^2 + B^2}$  represents  $|H(\omega)|$ , which gives the ratio between response and the excitation;  $\phi = \arctan(B/A)$  gives the phase angle between response and excitation.

The frequency-domain method suits well for systems exposed to random wave environments, since the random response spectrum can be computed directly from the transfer function and the wave spectrum in the following way [DNV \(2010a\)](#):

$$S_{yy}(\omega) = |H(\omega)|^2 S_{xx}(\omega) \quad (2.96)$$

Where  $\omega$  = angular frequency;  $H(\omega)$  = transfer function of the response;  $S_{xx}(\omega)$  = wave spectrum;  $S_{yy}(\omega)$  = response spectrum.

For typical TLP geometries and tendon arrangements, the analysis of the total dynamic loads effects maybe carried out as [DNV \(2008\)](#):

- a HF analysis of springing
- a WF analysis in all six degrees of freedom

- a LF analysis in surge, sway and yaw

The wave frequency domain analysis is normally carried out by using linear wave potential theory to discover the first-order structure motions and forces. What's more, the high frequency domain analysis shall be performed especially to evaluate the TLPWT and its tendons' susceptibility to springing effects. The QTF can be calculated in the process for testing the springing effects. This is the basis for determination of tendon fatigue due to springing [DNV \(2008\)](#). Total damping level applied in the springing response analysis shall be duly considered and documented.

This method benefits from its simplicity and efficiency, so that the frequency domain analysis is widely used in offshore structures for the analysis of their motions and forces. It is usually applied in fatigue analysis and analysis of more moderate environmental conditions due to its limitation, that it requires linear equation of motions [DNV \(2010a\)](#).

## 2.4.2 Time Domain Analysis

### Convolution Integral

The method used for non-linear analysis in current project is based on a numerical integration of dynamic equilibrium equation. Such method is especially fitted from dynamic analysis with element method, and are used daily by engineers for dimensioning of many types of structures which are exposed to time-varying loads. SIMO uses convolution integral approach for solving equation of motion (Eq. 2.55) [MARINTEK \(2012b\)](#).

Eq. 2.55 can be written as:

$$[\mathbf{M} + \mathbf{A}(w)]\ddot{\mathbf{x}} + \mathbf{B}(w)\dot{\mathbf{x}} + \mathbf{C}\mathbf{x} = \mathbf{f}'(t) = \mathbf{q} - \mathbf{D}_2\mathbf{f}(\dot{\mathbf{x}}) - \mathbf{D}_1\dot{\mathbf{x}} \quad (2.97)$$

With regarding to frequency-dependent coefficients only, this equation can be represented by:

$$\mathbf{A}(w)\ddot{\mathbf{x}} + \mathbf{B}(w)\dot{\mathbf{x}} = \mathbf{f}(t) = \mathbf{f}'(t) - \mathbf{C}\mathbf{x} - \mathbf{M}\ddot{\mathbf{x}} \quad (2.98)$$

Eq. 2.98 shows that right hand force varies sinusoidally at given frequency  $\omega$ . Then this equation can be converted to frequency-domain:

$$[-w^2\mathbf{A}(w) + \mathbf{i}w\mathbf{B}(w)]\mathbf{X}(w) = \mathbf{F}(w) \implies [\mathbf{i}w\mathbf{A}(w) + \mathbf{B}(w)]\mathbf{i}w\mathbf{X}(w) = \mathbf{F}(w) \quad (2.99)$$

Using the following relations:

$$\mathbf{A}(w) = \mathbf{A}_\infty + \mathbf{a}(w) \quad (2.100)$$

$$\mathbf{B}(w) = \mathbf{B}_\infty + \mathbf{b}(w) \quad (2.101)$$

Where  $\mathbf{A}_\infty = \mathbf{A}(w = \infty)$  and  $\mathbf{B}_\infty = \mathbf{B}(w = \infty) = 0$ , Eq. 2.99 can be written as:

$$-w^2\mathbf{A}_\infty\mathbf{X}(w) + [\mathbf{i}w\mathbf{a}(w) + \mathbf{b}(w)]\mathbf{i}w\mathbf{X}(w) = \mathbf{F}(w) \quad (2.102)$$

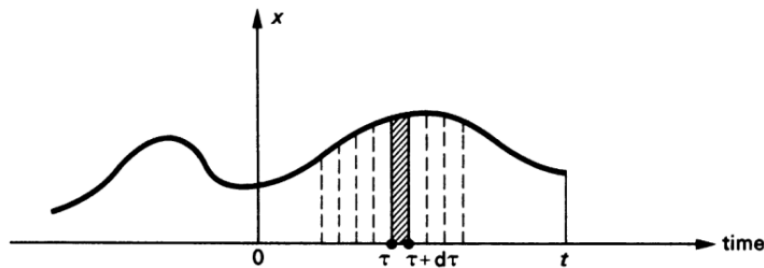


Figure 2.19: Breaking down an arbitrary input  $x(t)$  into a series of "impulses" [Newland \(1993\)](#)

Figure 2.19 shows breaking down an arbitrary input  $x(t)$  into a series of "impulses". The impulse response function  $h(t)$  gives the response at time  $t$  to a unit impulse applied at time  $t = 0$ ; while  $h(t - \tau)$  gives response at time  $\tau$  to a unit impulse applied at  $t = \tau$ . Application of the superposition principle for linear system gives the total response at time  $t$ :

$$y(t) = \int_{-\infty}^t h(t - \tau)x(\tau)d\tau \quad (2.103)$$

This impulse response method and inverse Fourier transform are applied to Eq. 2.102:

$$\mathbf{A}_\infty \ddot{\mathbf{x}}(t) + \int_{-\infty}^{\infty} \mathbf{h}(t-\tau) \dot{\mathbf{x}} d\tau = \mathbf{f}(t) \quad (2.104)$$

When  $t < 0$ , i.e. before "experiment" start, the value of  $\mathbf{h}(t-\tau)$  should be physically zero. Also causality implies that  $\mathbf{h}(t-\tau) \equiv 0$  for  $\tau > t$ . So Eq. 2.105 can be rewritten as:

$$\mathbf{A}_\infty \ddot{\mathbf{x}}(t) + \int_0^t \mathbf{h}(t-\tau) \dot{\mathbf{x}} d\tau = \mathbf{f}(t) \quad (2.105)$$

Substituting  $\mathbf{f}(t)$  from Eq. 2.98 and  $\mathbf{f}'(t)$  from Eq. 2.97, the equation of motion becomes:

$$(\mathbf{M} + \mathbf{A}_\infty) \ddot{\mathbf{x}} + \mathbf{D}_1 \dot{\mathbf{x}} + \mathbf{D}_2 \mathbf{f}(\dot{\mathbf{x}}) + \mathbf{C}\mathbf{x} + \int_0^t \mathbf{h}(t-\tau) \dot{\mathbf{x}} d\tau = \mathbf{q}(\mathbf{t}, \mathbf{x}, \dot{\mathbf{x}}) \quad (2.106)$$

Where the retardation function  $\mathbf{h}(\tau)$  is computed by a transform of the frequency-dependent added-mass and damping:

$$\mathbf{h}(\tau) = \frac{1}{2\pi} \int_{-\infty}^{\infty} [\mathbf{c}(w) + i w \mathbf{a}(w)] \mathbf{e}^{i w \tau} \mathbf{d}w \quad (2.107)$$

Using  $\mathbf{b}(w) = \mathbf{b}(-w)$  and  $\mathbf{a}(w) = \mathbf{a}(-w)$ :

$$\mathbf{h}(\tau) = \frac{1}{\pi} \int_0^{\infty} [\mathbf{b}(w) \cos(w\tau) - w \mathbf{1}(w) \sin(w\tau)] \mathbf{d}w \quad (2.108)$$

$\mathbf{h}(\tau) = 0$  for  $\tau < 0$  from causality so that this process have no memory effect of the future. This implies that the two parts in Eq. 2.108 must be opposite for  $\tau < 0$  and identical for  $\tau > 0$ , or mathematically:

$$\mathbf{h}(\tau) = \frac{2}{\pi} \int_0^{\infty} \mathbf{b}(w) \cos(w\tau) \mathbf{d}w = -\frac{2}{\pi} \int_0^{\infty} w \mathbf{a}(w) \sin(w\tau) \mathbf{d}w \quad (2.109)$$

for  $\tau > 0$ .

This means that the frequency-dependent mass and damping can be found from retardation function  $\mathbf{h}(\tau)$  based on Eq. 2.109.

In order to form Eq. 2.106, the force vector  $\mathbf{q}$  needs to be determined Wang (2014):

$$\mathbf{q} = \mathbf{q}^{(1)} + \mathbf{q}^{(2)} + \mathbf{q}_{\text{drag}} + \mathbf{q}_{\text{mooring}} + \mathbf{q}_{\text{wind}} \quad (2.110)$$

Where  $\mathbf{q}^{(1)}$  is the first order wave excitation loads that can be found from Panel Method in HydroD and  $\mathbf{q}^{(2)}$  is the second order wave loads that can be obtained from QTF functions with free surface model also in HydroD [DNV \(1994\)](#). These loads are converted to second-order transfer functions in SIMO. The nonlinear quadratic drag force  $\mathbf{q}_{\text{drag}}$  can also be added to the equation of motion by using Morison elements in SIMO [Bachynski \(2014\)](#). The mooring line force (calculated in RIFLEX) and the wind force (calculated in AeroDyn) are added to this equation at each time step [Wang \(2014\)](#).

The Eq. 2.106 should be solved based on an incremental procedure using the dynamic time integration scheme, according to Nemark  $\beta$  method [MARINTEK \(2012b\)](#). Pure Newton-Raphson iteration is applied for all SRA simulations. The SRA simulations are performed with integration parameters presented in Table 2.2. Detailed SRA process is explained in Chapter 6.

Table 2.2: Newmark-Beta integration parameters used in SRA simulations

$\Delta t$	0.005s
$\gamma$	0.505
$\beta$	0.2564

### SIMO-RIFLEX-AeroDyn

SIMO is a computer program system developed by MARINTEK, which is used to model the rigid body floating structures [MARINTEK \(2011\)](#). The state-of art models of LF, WF and HG excitation can be employed for modeling the hydrodynamic loads on floating structures by using SIMO.

RIFLEX, another computer program system developed by MARINTEK for analysis of slender offshore structures [MARINTEK \(2013\)](#). Actually, it is a non-linear time-domain program with a finite element formulation that can handle unlimited displacement and rotations. Both static analysis and dynamic analysis are performed in RIFLEX. The static analysis is based on a complete non-linear formulation, while the time domain analysis is based on step by step numerical

integration of the dynamic equilibrium equations. All the analysis are three-dimensional [MARINTEK \(2012a\)](#). RIFLEX is used to define the beam elements of the TLPWT in this project, such as TLP tendons, tower and blades. The definition for the RIFLEX model is given in Appendix E.

By including aerodynamic forces on elastic structural members using the publicly available AeroDyn code, the commercial SIMO-RIFLEX has been updated to the coupled code SIMO-RIFLEX-AeroDyn: a time-domain simulation tool for fixed and floating wind turbine [Ormberg et al. \(2012\)](#). This code was developed by Bachynski [Bachynski \(2014\)](#) for the analysis of TLPWT in 2014, see Figure 2.20. A Dynamic Link Library (DLL) behaves as the connection between RIFLEX and AeroDyn. In this project, the TLPWT is modeled as a rigid Simo body with flexible Riflex elements for mooring lines and the aerodynamic properties are modeled in AeroDyn. This tool takes advantage of the nonlinear beam element models in RIFLEX, hydrodynamic models in SIMO and aerodynamic models in AeroDyn, together with an external controller.

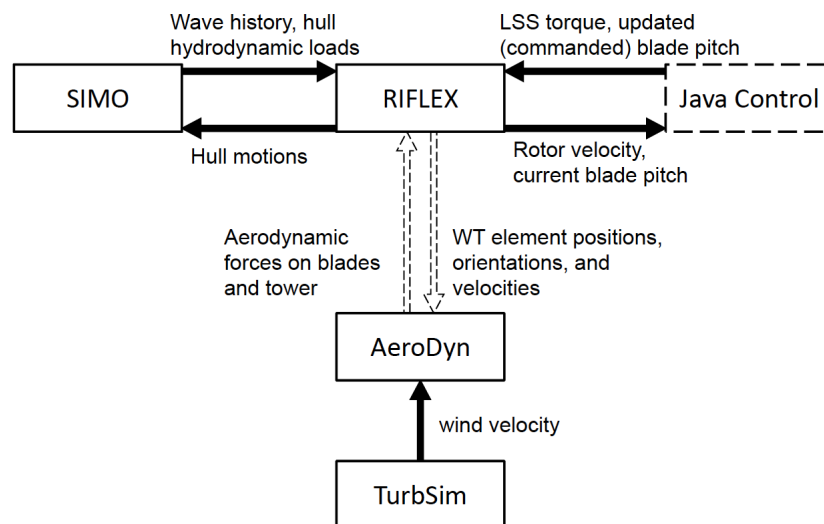


Figure 2.20: Illustration of the coupling between SIMO, RIFLEX, AeroDyn and the external controller [Bachynski \(2014\)](#)

## 2.5 TLP Floater Response Characteristics

The TLP floater concept fundamentally differs from other floater concepts in the sense that it is the tendon stiffness dominates its vertical motions instead of water plane stiffness. TLP floaters generally have very strong tension forces acting on its mooring system. For instance, three FVAWT concepts were designed in 2015 but the power spectral density of the tension for the TLP FVAWT is approximately three order of magnitude higher than that of the semi FVAWT and the spar FVAWT [Cheng et al. \(2015\)](#). Due to the unique and strong tendon riser system, a TLP floater is normally soft in surge, sway and yaw motions, but stiff in heave, roll and pitch motions. On the contrary, other floaters are also relatively soft in vertical motions. This can be seen from [Table 2.3](#).

Table 2.3: Typical natural periods of deep water floaters [DNV \(2010a\)](#)

Floater Mode	Natural periods (s)			
	FPSO	DDF	TLP	Semi-submersible
Surge	>100	>100	>100	>100
Sway	>100	>100	>100	>100
Heave	5-12	20-35	<5	20-50
Roll	5-30	50-90	<5	30-60
Pitch	5-12	50-90	<5	30-60
Yaw	>100	>100	>100	>100

A TLP floater generally experiences wave frequency motions in horizontal directions of the same order of magnitude as those of a semi-submersible of comparable size [DNV \(2010a\)](#). In the vertical directions, however, the TLP floater usually behaves like a fixed structure with practically no wave frequency motions response. The environmental forces are directly counteracted by its tendon stiffness forces. Moreover, the second-order sum-frequency wave loads may introduce the 'springing' response and higher-order wave loads can even cause a transient response, which is called 'ringing'.

In addition, the heave motions of a TLP floater is kinematically coupled with horizontal



surge/sway motions, which is often denoted as 'set-down' effect [Lygren \(2011\)](#). The designers must pay enough attention to the assessment of the TLPWT hydrodynamic stability, since it plays a vital role in the calculation of air-gap, tether forces and riser system responses such as stroke [DNV \(2010a\)](#). Section 4.1 discusses the hydrostatic stability of this TLPWT concept design.

Typical parameters should be considered for the global performance of TLP floaters, including TLP draughts, wave conditions and headings, tidal effects, storm surges, set-down, foundation settlements, subsidence, mis-positioning, tolerance, tendon flooding, tendon removal and hull compartment flooding [DNV \(2008\)](#).

## Chapter 3

# TLP Wind Turbine Design

After the first tension leg platform - Conoco Hutton was built in the early of 1980s, this special structure has been a popular choice for its high stability. Compared with other offshore structures, a TLP structure has favorable characteristics that its dynamic response is typically much smaller. The concept of using TLP for wind turbine was first proposed by the Massachusetts Institute of Technology (MIT) [Bachynski \(2014\)](#). TLPWT represents one potential method for accessing offshore wind source in deep water.

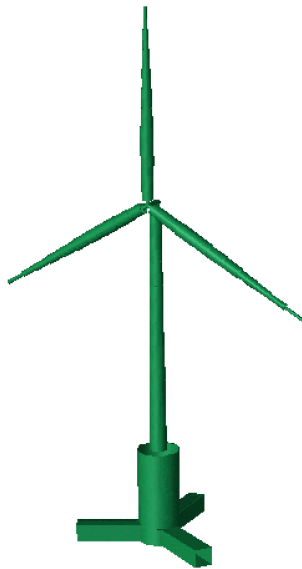


Figure 3.1: TLPWT front view in GeniE

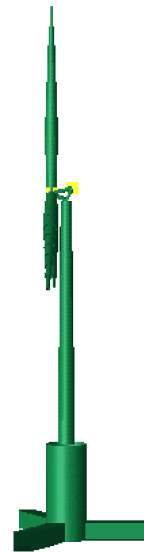


Figure 3.2: TLPWT side view in GeniE

Figure 3.1 and Figure 3.2 show the front and side view of the designed TLPWT respectively. The initial design process is described in the previous specialization project [Tian \(2015\)](#). This TLP floater consists of a central column and three spokes. Basically, the hull dimensions of the TLP floater is obtained by upscaling the floater of the 5MW TLPWT3 [Bachynski \(2014\)](#) developed by Erin Elizabeth Bachynski in 2014 with proper scale ratio. A summary of scale ratios of the TLPWT physical parameters is shown in Table 3.1.

Table 3.1: Scaling of the floater parameters using the Froude scaling law

Linear dimensions (Length, width, height, diameter and thickness etc.)	$\lambda$
Floater mass and floater displacement	$\lambda^3$
Moment of inertia of floater	$\lambda^5$
Natural period of rigid-body motions of vertical modes (heave, pitch and roll)	$\sqrt{\lambda}$
Natural frequency of rigid-body motions of vertical modes (heave, pitch and roll)	$1/\sqrt{\lambda}$
Force	$\lambda^3$
Moment	$\lambda^4$
Stress	$\lambda$
Acceleration	1
Time	$\sqrt{\lambda}$
Pressure	$\lambda$

The origin point of global coordinate system locates at the center of central column in the still water level. Six degrees of freedom (Figure 3.3) are considered during the TLPWT design process.

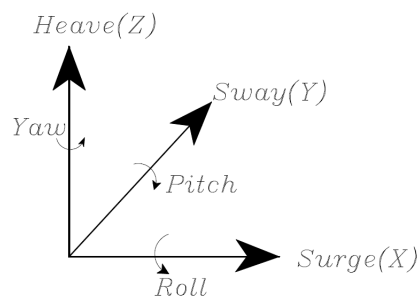


Figure 3.3: Degrees of freedom for the TLPWT [Refat and El-gamal \(2014\)](#)

The TLPWT concept represented in this project is actually based on the so-called SeaStar deepwater mini-platform. The first SeaStar TLP in the world is Morpeth TLP (Figure 3.4), built in Gulf of Mexico in 1998 [Kibbee et al. \(1999\)](#). The SeaStar TLP features small size, moderate cost, simple construction and installation and significant storage capability.

Figure 3.4: Morpeth TLP [Kibbee et al. \(1999\)](#)Figure 3.5: SeaStar TLP hull [Kibbee \(1996\)](#)

This chapter introduces the design criteria for the TLPWT design in Section 3.1, the configurations of wind turbine in Section 3.2, the designed TLP hull in Section 3.3 and mooring Section 3.4. In the end, Section 3.5 emphasizes the key parameters of the TLPWT.

## 3.1 Design Criteria

The conceptual design for the TLPWT is based on the requirements in terms of stability, natural period and displacement. In addition, the preliminary design should comply with the theory, that the three tendon tensions cannot be zero. Only in this way, the TLP slacking phenomenon can be avoided.

### 3.1.1 Stability

For a TLP wind turbine, the stability criteria mainly consider the effects of wind, wave. Current are not explicitly taken into account. Thus the heeling (overturning) moment is typically calculated by the integration of the wind force effects along the total windward area:

$$M_H = \int T h \quad (3.1)$$

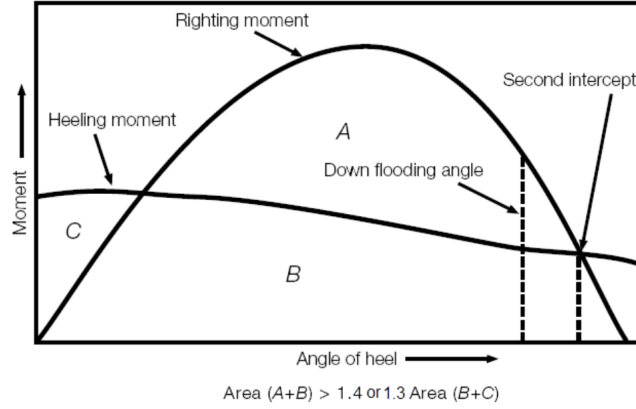


Figure 3.6: Characteristic features of  $M-\theta$  curves Veritas (2001)

Where  $T$  is the thrust force acting at different positions of the wind turbine and  $h$  is relative the moment arm. But only the maximum wind thrust,  $T_{max}$ , is considered here, so Eq 3.1 can be simplified as:

$$M_H = T_{max}H \quad (3.2)$$

Generally speaking, the TLP wind turbine should rotate across the top point of tethers. Literally, however, the overturning point is assumed as a wet area center to simplify this problem, so  $H$  is taken as the distance between the hub center and the water plane. Considering the overturning moment, the largest heeling angle  $\theta_a$  corresponding to the maximum thrust force should be less than 7 degrees, i.e.  $\theta_a \leq 7^\circ$  Chenyu Luan (2015). Based on linear theory,  $\theta_a$  can be calculated by Eq. 3.3. A small value of  $\theta_a$  implies good intact stability and large roll/pitch restoring stiffness.

$$\theta_a = \frac{M_H}{K} = \frac{T_{max} \times H}{K_{55} + C_{55}} \quad (3.3)$$

Where  $\theta_a$  is defined as the static angle of heels, at which point the heeling moment and righting moment get the first interception (Figure 3.6). When the heeling angle  $\theta$  is larger than the second interception angle, the overturning moment is greater than the righting moment, leading to capsizing. Obviously, the area under the  $M-\theta$  curves, which can be expressed as the integral  $\int M d\theta$ , represents energy. To prevent excessive heeling and eventually capsizing,

a proper "energy-based" criteria should be obtained. Usually this righting moment curve can be computed automatically in HydroD, but it is not working for TLP structures. The hydrostatic stability of the TLPWT, therefore, is done by hand calculation in Section 4.1.

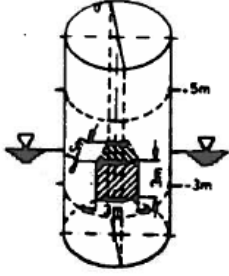
Figure 3.7 illustrates the intact and damage stability of mobile drilling structures according to NMD NMD (1987). For the TLPWT, the area under the righting moment curve to the angle of down-flooding should not be less than 30% in excess of the area under the wind heeling moment curve to the same limiting angle. Consequently, the mean surge/sway offset of the TLP floater should not exceed 5% of the water depth, in order to limit the angle of the tendon connectors Bachynski (2014). In this case, the water depth is 200m and thus the corresponding maximum allowable offset caused by wind thrust is 10m. The horizontal offset of the TLPWT can be calculated by Eq. 3.4.

$$s_{offset} = \frac{T_{max}}{K_{11}} \quad (3.4)$$

Where  $K_{11}$  is the horizontal tendon stiffness, calculated in Eq. 2.71.

### 3.1.2 Natural Period

Generally speaking, most of the waves in open sea have significant energy at a period interval of 5 – 20s. Thus offshore structures are supposed to be designed to have natural periods of rigid body motions away from this region, to avoid resonance phenomenon. In details, the surge and sway natural periods for a TLP structure should be larger than 25s, while the heave, pitch and roll natural periods should be less than 3.5s Bachynski (2014). It means that the TLP structure is soft in surge, sway and yaw motions, but stiff in heave, roll and pitch motions. The estimation of natural periods regarding to uncoupled motions in all degrees of freedoms can be achieved based on the equations given in Section 2.3.1. It can be seen from Eq 2.81 that the heave natural period increases along with the tendon length, i.e. the water depth. Consequently, the stiffness due to the water plane area is much smaller comparing with the restoring effect of tendons.

Criterion		Intact stability	Damage stability	
$\overline{GM}_0$ for ships, jack-ups for semisubmersibles - under operating conditions - at short intervals		$\geq 0.5$ m	One compartment damage adjacent to the sea 	
	$\theta_1$	$\leq 15^\circ$		$\leq 15^\circ$
	$\theta_2$	$\leq 30^\circ$		
$K = \frac{A+B}{B+C}$ for ships, jack-ups for semisubmersibles		$\geq 1.4$	$\geq 1$	
		$\geq 1.3$	$\geq 1$	

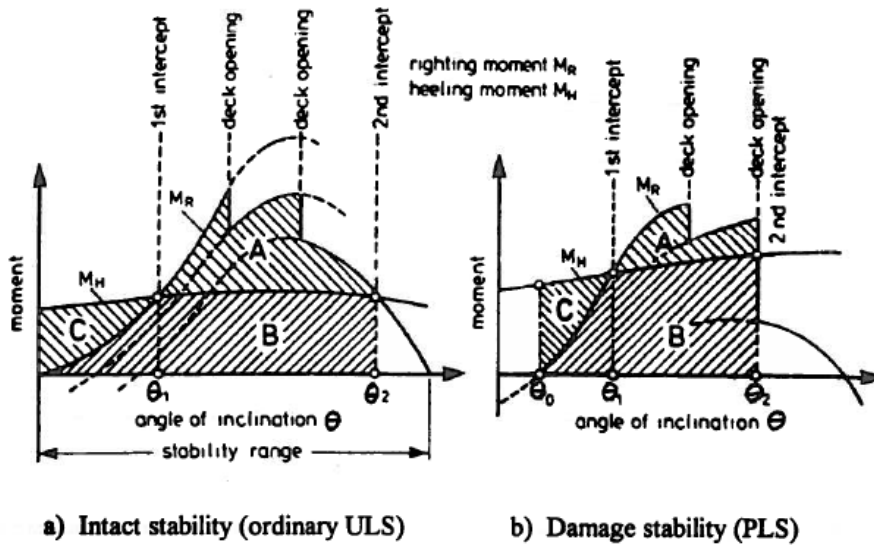


Figure 2.10 Intact and damage stability criteria of offshore structures [2.4]

Figure 3.7: Intact and damage stability of criteria of offshore structures NMD (1987)

### 3.1.3 Displacement

The design of offshore structures requires sufficient displacement to survive from extreme weather conditions:

$$\Delta > 2000m^3 \quad (3.5)$$

A minimum displacement increases both the stiffness of the system and its ability to mitigate extreme loads by platform inertia [Bachynski et al. \(2012\)](#). However, a too high displacement may contribute to a too stiff design. Thus it is important to adjust the displacement of the structure to a proper level.

### 3.1.4 TLP Slacking

Figure 3.8(a) [Moan \(1994\)](#) shows that the TLP floater is a specific structure with excessive buoyancy  $V$  and pretension  $S$ . When the TLP is subjected to resulting forces  $H$  and  $M$  due to wind, wave and current, it undergoes both horizontal displacement and vertical decline. In consequence, the tethers will be partly larger while partly less than the pretension  $S$ . If the forces keep increasing, then right tether slacks and rotation increases until the whole structure capsizes as shown in Figure 3.8(c). Therefore, the minimum tensions on the TLP tethers must be checked in the preliminary design process in order to avoid the slacking phenomenon.

In order to guarantee the TLPWT safe even in harsh weather conditions, the tethers need to fulfill the ultimate limit state (ULS) requirement [DNV \(2008\)](#):

$$\gamma_0 S_0 - \gamma_E S_E \geq 0 \quad (3.6)$$

Where  $S_0$  is axial pretension force;  $S_E$  is the axial force due to environment load and  $\gamma_0$  as well as  $\gamma_E$  are safety factors. For the tendons of a TLP structure,  $\gamma_0 = 1.2$  and  $\gamma_E = 0.7$ .



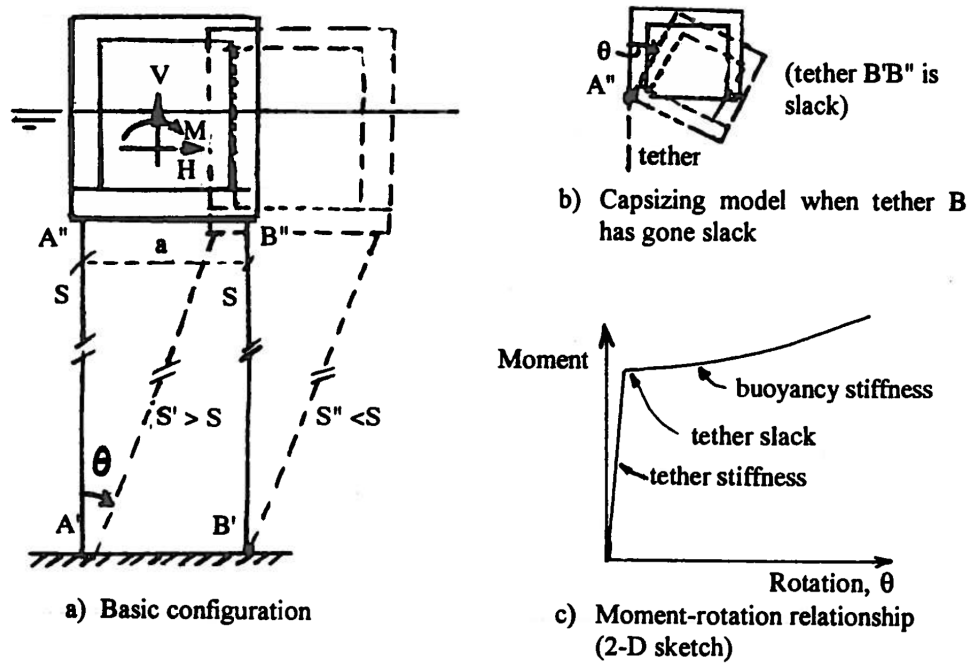


Figure 3.8: Tension leg platform TLP Moan (1994)

## 3.2 Wind Turbine

From the late 1970s until now the wind turbine trends to be in larger scale for the sake of business benefit. The largest wind turbine on the market now is in the order of 8 MW - Vestas V164 8MW turbine Wind (2013). But DTU Wind Energy has already designed the DTU 10MW Reference Wind Turbine (See Figure 3.9) in 2013 Bak et al. (2013). The presented TLP floater in this project precisely supports this kind of wind turbine.



Figure 3.9: DTU 10MW reference wind turbine Bak et al. (2013)

Table 3.2 lists the specifications of the DTU 10MW Reference Wind Turbine. It is a three-blade, upwind and horizontal wind turbine. The turbine has a cut-in wind speed of  $4\text{m/s}$  from which the turbine starts power production, a rated wind speed of  $11.4\text{m/s}$  from which the power production keeps constant by pitching its blades, and a cut-out wind speed of  $25\text{m/s}$  which is maximum operational wind speed. This also can be seen from Figure 3.10. It should be noted the hub height  $119\text{m}$  is the distance from the hub to the water surface.

Table 3.2: DTU 10MW Reference Wind Turbine Design Summary [Bak et al. \(2013\)](#)

Description	Value
Rating	10MW
Rotor orientation, configuration	Upwind, 3 blades
Control	Variable speed, collective pitch
Drivetrain	Medium speed, multiple stage gearbox
Rotor, Hub diameter	$178.3\text{m}$ , $5.6\text{m}$
Hub height	$119\text{m}$
Cut-in, Rated, Cut-out wind speed	$4\text{m/s}$ , $11.4\text{m/s}$ , $25\text{m/s}$
Cut-in, Rated rotor speed	$6\text{RPM}$ , $9.6\text{RPM}$
Rated tip speed	$90\text{m/s}$
Overhang, Shaft tilt, Pre-cone	$7.07\text{m}$ , $5^\circ$ , $5^\circ$
Pre-bend	$3\text{m}$
Rotor mass	$229\text{tons}$ (each blade $41\text{tons}$ )
Nacelle mass	$446\text{tons}$
Tower mass	$605\text{tons}$

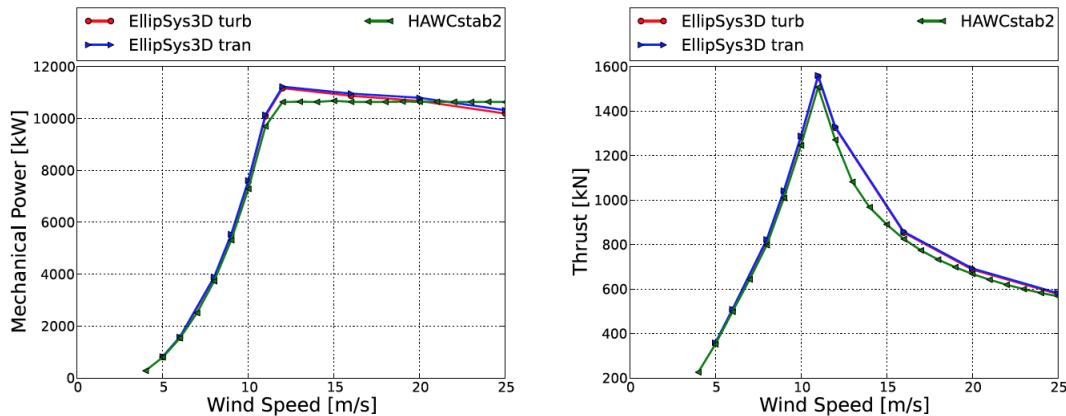


Figure 3.10: Power and thrust as function of wind speed for the rotor computed using EllipSys3D compared to HAWCStab2 simulations [Bak et al. \(2013\)](#)

### 3.3 TLP Hull

Figure 3.11 presents the TLP hull. As shown in this figure, Three spokes spread evenly ( $120^\circ$ ) around the central column of the TLP. Actually, the central column consists of two columns all made from mild steel with the same density of  $7850\text{kg}/\text{m}^3$ . However, these columns have different thicknesses. Because the three spokes are all connected with the bottom column, the bottom column is designed as about twice thicker than the upper one to provide sufficient strength. Additionally, there is  $4456\text{tons}$  concrete ballast with density of  $2562.5\text{kg}/\text{m}^3$  in inside the bottom column to provide required draft, which is also feasible to adjust during transportation and installation. Furthermore, the compartmentalization in both the columns and spokes (see Figure 3.5) could limit the effects of accidental damage.

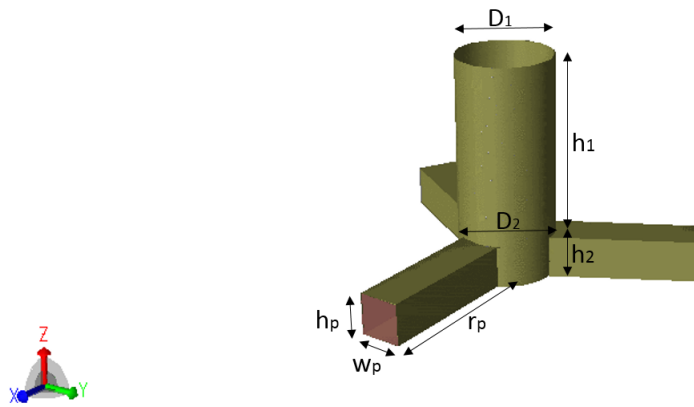


Figure 3.11: TLP hull (Its dimensions are listed in Table 3.3)

Different from other offshore structures ( $G = B$ ), the vertical balance for a TLP structure is given in Eq. 3.7. The ballast system plays an important role in ensuring the stability of the TLPWT during the installation operation when the mooring system is not attached.

$$G = B + T \quad (3.7)$$

Where  $G$  is the gravity of the structure;  $B$  is buoyancy;  $T$  is the total tension.

The main dimensions of the TLP hull are listed in Table 3.3. The TLP hull provides sufficient buoyancy to support deck, facilities and flexible risers and has sufficient excess buoyancy to develop the design tendon pretension. The hull is designed of a stiffened plate and shell con-

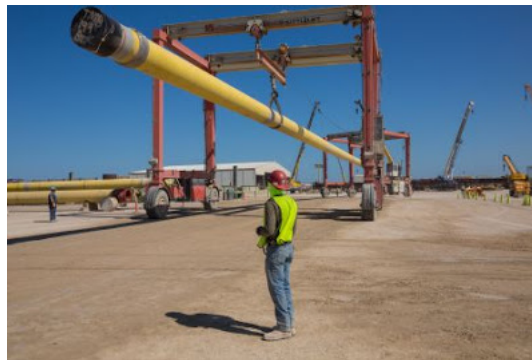
struction. Moreover, it should be emphasized that the total displacement and mass shown in this table does not count the displacement and mass of tendons, for the the net displacement and mass of tendons are relatively small compared with the entire structure. The freeboard of the TLPWT is  $10m$ , which fulfills the stability requirement by the DNV standard [DNV \(2013a\)](#).

Table 3.3: Specification of TLP floater

Water depth	$H$	$200m$
Freeboard	$f$	$10m$
Upper column diameter	$D_1$	$19.8m$
Upper column length	$h_1$	$36.8m$
Lower column diameter	$D_2$	$19.8m$
Lower column length	$h_2$	$8.5m$
Spoke radius	$r_p$	$39.6m$
Spoke height	$h_p$	$8.5m$
Spoke width	$w_p$	$8.5m$
Total displacement	$B$	$17307m^3$
Total mass	$M$	$8121t$

### 3.4 Tendon Mooring System

The buoyancy of the TLPWT is about twice than its weight (Table 3.3), requiring big pretension forces to secure the structure to the foundation on the seabed. The TLP hull is moored by tubular steel tendons (like shown in Figure 3.12), whose thickness is  $89mm$ . There is one tendon attaching with the substructure at the end of every spoke, see Figure 3.13. In order to prevent excessive vibration, strakes maybe attached to the surface of tendons.

Figure 3.12: Real tendons pieced together in 270-foot sections [Smith \(2015\)](#)

Generally speaking, the tendon mooring system suppresses heave motion and reduces excursions compared to catenary mooring [Kibbee \(1996\)](#). Since the buoyancy of the three tendons is almost equivalent to its weight, it is assumed that the tendons are naturally buoyant.

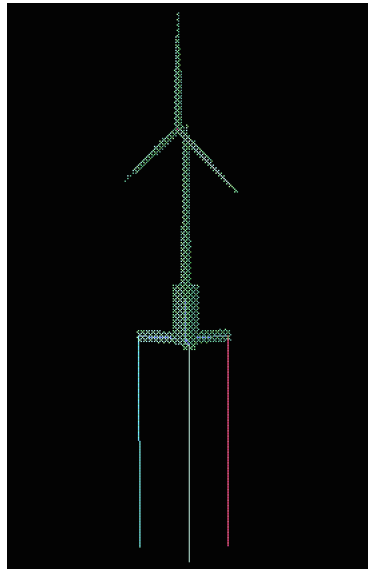


Figure 3.13: Morison model of the TLPWT including the tendon mooring system in HydroD

Table 3.4 lists the specifications of the tendon mooring system.

Table 3.4: Specifications of tether mooring system

Number of mooring lines	$n_t$	3
Outer radius	$r_2$	1.35m
Inner radius	$r_1$	1.26m
Density	$\rho_{steel}$	7850kg/m <sup>3</sup>
Inertia moment	$I_t$	0.623m <sup>4</sup>
Young's modulus	$E$	2.11E11Pa
Mass per unit length	$m_t$	5737kg/m
Tether stiffness	$k_t$	931845kN/m
Unstretched tether length	$l_t$	164.7m
Pretension per line	$F_t$	28064kN

### 3.5 Summary of key parameters

The key parameters from the preliminary design of the DTU 10MW TLPWT are summarized in Table 3.5. The main dimensions for every compartments of the TLPWT are given in Appendix B.

Table 3.5: Key parameters for the DTU 10MW TLPWT preliminary design

Geometry		Property	
Turbine power	10MW	Turbine Mass	1280t
Hub height	119m	Floater mass	8013t
Central column diameter	19.8m	Total mass	9293t
Spoke radius	39.6m	Displacement	17362m <sup>3</sup>
Draft	35.3m	Center of gravity	(-0.04m, 0m, -9.83m)
Water depth	200m	Center of buoyancy	(0m, 0m, -22.67m)

Assuming the whole TLPWT as a fully rigid structure, the natural periods in 6 DOF of the TLPWT obtained from spreadsheet calculation are listed in Table 3.6.

Table 3.6: Natural periods of the TLPWT from spreadsheet calculation

Surge/Sway	$T_1/T_2$	45.53s
Heave	$T_3$	0.53s
Roll/Pitch	$T_4/T_5$	0.76s
Yaw	$T_6$	19.04s

After establishing the TLPWT model in softwares, the added mass, restoring stiffness and tendon stiffness are calculated, shown in Table 3.7.

Table 3.7: Added mass, storing stiffness and tendon stiffness calculation results in HydroD

Added mass coefficients		Storing stiffness coefficients		Tendon stiffness coefficients	
$A_{11}$	15062t	$C_{11}$	0	$K_{11}$	499kN/m
$A_{22}$	15062t	$C_{22}$	0	$K_{22}$	499kN/m
$A_{33}$	9925t	$C_{33}$	3096kN/m	$K_{33}$	2808846kN/m
$A_{44}$	10799102tm	$C_{44}$	-2810000kNm/rad	$K_{44}$	2202600543kNm/rad
$A_{55}$	10799102tm	$C_{55}$	-2810000kNm/rad	$K_{55}$	2202600543kNm/rad
$A_{66}$	1964238tm	$C_{66}$	-	$K_{66}$	782651kNm/rad

# Chapter 4

## Frequency Domain Hydrostatic and Hydrodynamic Analysis

A frequency-domain analysis (introduced in Section 2.4.1) is performed in HydroD, by using composite model with drag velocity  $2m/s$  and one-node Gauss. Basically, the TLPWT models for frequency-domain analysis are established in GeiniE except for the tendon elements, which are built in HydroD and connected to TLP Morison model directly. The super-element type are defined as type 1, 2 and 4 for panel model (Figure 4.1), Morison model (Figure 4.2) and mass model (Figure 4.3) respectively. The panel model is used for stability analysis and calculation of the 3D wave potential in Wadam. This matters with the outer wetted surface area of the panel model. The applied mesh size for the panel model is about  $1m$  Tian (2015).

Besides, the second-order free surface model with proper discretization is also established in GeiniE. Note that the wet surface property should be assigned to the front side of the panel model, but back side of free surface model. The selection of mesh density for free surface model is discussed in Section 4.2.

By using composite model and running Wadam Wizard, the frequency-domain analysis is performed in HydroD. Drag velocity  $2m/s$  and one-node Gauss are used in these computations.

Neglecting nonlinear wave excitation terms (such as quadratic damping, amplitude-dependent

higher order terms etc.), the wave excitation and caused body response at one frequency can be assumed harmonic. For a given frequency, Eq. 2.55 can then be re-written as:

$$[-\omega^2(M_{jk} + A_{jk}(w)) + i\omega B_{ik}(w) + (C_{jk} + K_{jk})]\eta_k = F_j(w) \quad (4.1)$$

The coefficients  $A_{jk}$  and  $B_{ik}$  are frequency-dependent, therefore this equation can be easily solved, and then the first- and second- order hydrodynamic results can be obtained, discussed in Section 4.3 and Section 4.4 respectively. Furthermore, the hydrostatic stability is assessed by hand calculation in Section 4.1 due to the limit of Wadam Wizard for TLP structures.

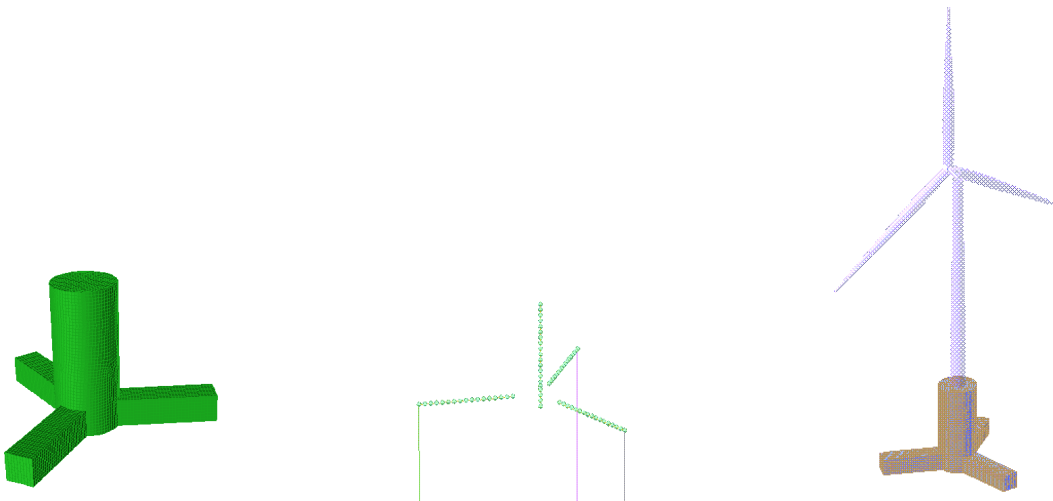


Figure 4.1: TLP panel model    Figure 4.2: TLP Morison model    Figure 4.3: TLPWT mass model

## 4.1 Hydrostatic Stability

The SESAM software HydroD fails to assess the hydrostatic stability for TLP structures, so that the hydrostatic stability of this TLPWT is checked by hand calculation in this project. Figure 4.4 shows the schematic TLP with displaced position, due to the wind, wave and current forces. The TLP undergoes a horizontal displacement  $\delta_x$ , a vertical decline  $\delta_z$  and also a small pitch  $\theta$ . Consequently, the fore tether tension  $T_f$  is larger than its original tension  $T_0$ , while the aft tether tension  $T_a$  is smaller than  $T_0$ , i.e.

$$T_f = T_0 + k(\varepsilon + r_p\theta) \quad (4.2)$$



$$T_a = T_0 + k(\varepsilon - r_p\theta) \quad (4.3)$$

It is important to guarantee that all the tendons are always retained in tension. Otherwise, slacking phenomenon will occur and then the TLPWT may capsize. In order to check the minimum aft tension force, the maximum wind thrust  $1560kN$  (See Figure 3.10) is applied to this TLPWT.

In this case, the horizontal movement  $\delta_x$  is only  $3.05m$  obtained by Eq. 4.4, which is less than 5% water depth.

$$\delta_x = \frac{T_{wind}}{K_{11}} = 3.05m \quad (4.4)$$

The corresponding tether pitch angle  $\alpha$  is:

$$\alpha \approx \frac{\delta_x}{L} = 3.05164.7 = 1.062^\circ \quad (4.5)$$

Assuming small inclination of the TLPWT, both of the tethers have the same pitch angle  $\alpha = 1.062^\circ$ . Then the equilibriums for horizontal forces, vertical forces and rotation moments can be obtained as follows.

$$\sum F_x = 0 \Rightarrow T_f \sin\alpha + T_a \sin\alpha = T_{wind} \quad (4.6)$$

$$\sum F_y = 0 \Rightarrow T_f \cos\alpha + T_a \cos\alpha = B - G \quad (4.7)$$

$$\sum M = 0 \Rightarrow T_f r_p - T_a r_p - T_{wind} H = 0 \quad (4.8)$$

Where  $r_p$  is pontoon length.

Combing Eq. 4.6, Eq. 4.7 and Eq. 4.8, it can be known that the fore tendon has tension force of  $44715kN$ , which is about 1.6 times of pretension  $28064kN$ , but still 4 times less than the yield

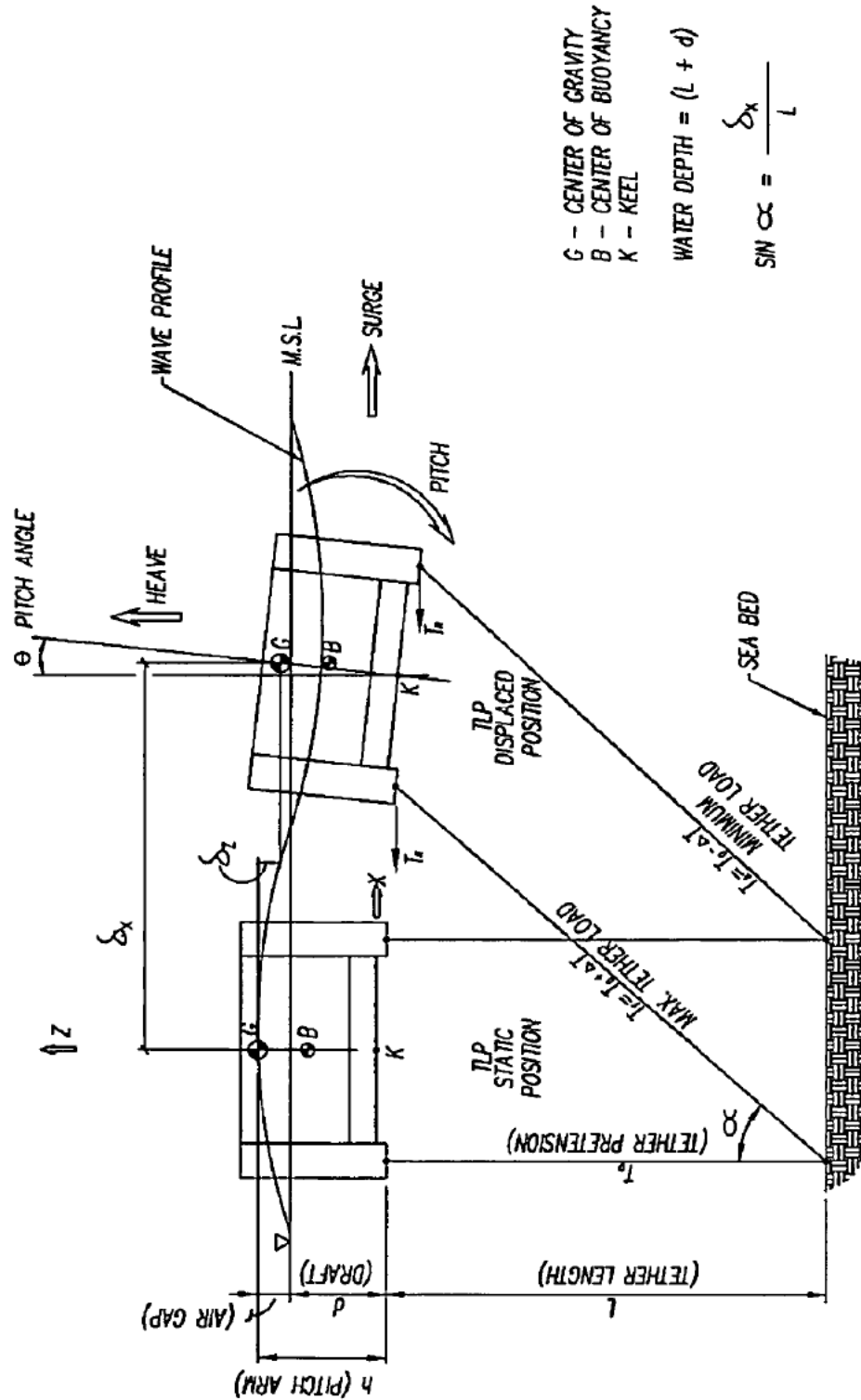


Figure 4.4: Schematic side elevation of a TLP illustrating the geometric displaced position of the platform in surge/sway with pitch and set-down relationship [Srinivasan \(2014\)](#)

load  $1.83 \times 10^5$  (calculated from Eq. 5.4). In fact, the designed TLPWT has two fore tendons, instead of one. Therefore the practical fore tensions (tension 1 and tension 2) should be less than  $44715kN$ . Additionally, the aft tendon has relatively smaller tension force of  $39631kN$ . There is no risk of exceeding yield stress or slacking. Furthermore, the tensions are double-checked by ULS based on results from real load cases in Section 5.3.5.

## 4.2 Mesh Convergence Study

As required by SESAM manual [DNV \(2013b\)](#), the element diagonal in the TLP panel model shall not exceed a quarter of wave length. This results in a mesh size of  $1m$  for the half TLP hull panel model (See Figure 4.5). Additionally, in order to compute second-order loads in Wadam, it is necessary to establish a second-order free surface model in GeniE, as discussed in Section 2.3.2. The free surface model should be meshed with 4 node shell elements (No. 3 node elements). Nevertheless, the Wadam Wizard, used for calculating second-order loads, employs a database called Objectstore, in which the maximum acceptable size of the database is only 600MB [DNV \(2013b\)](#). It is impossible to run analysis for a free surface model with more than 3000 basic elements. To achieve a more accurate result, the free surface is made in half but with the same symmetry as the TLP hull panel model (See Figure 4.6). In this way, the free surface model could have more elements involving in frequency-domain analysis.

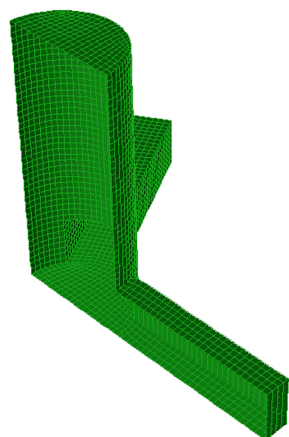


Figure 4.5: Meshed TLP panel model

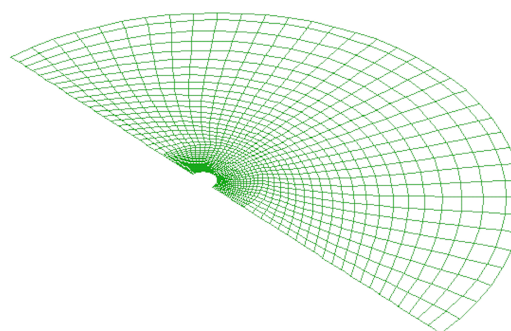


Figure 4.6: Meshed free surface model

The discretization of free surface model is dominated by the second-order incident wave length, which is one quarter of the first order wavelength. The rule of thumb indicates that every second order wavelength should cover at least 6 panels [DNV \(2010a\)](#), i.e.:

$$l_{mesh} < \frac{gT^2}{150} \quad (4.9)$$

The natural frequency of the TLPWT is  $11.42rad/s$  in heave and  $11.42rad/s$  in pitch referring to [Table 3.6](#). To access the effects of second-order loads, the utilized frequency packages must include the frequency pairs which summation equals to these natural frequencies. For instance, if the incoming wave has frequency  $4rad/s$ , i.e. half of the pitch natural frequency, the required biggest mesh size is only  $0.1m$  according to [Eq. 4.9](#). This will need 12,535,128 shell elements on the free surface, obviously exceeding the limitation of the software. In this case, a mesh convergency study is definitely required in order to assess the effects of second-order loads as much accurately as possible. Indeed, there are usually two approaches to vary the element number of free surface model: changing partitioning radius and changing mesh size. This chapter discusses the both approaches and aims to select the ideal mesh case.

### 4.2.1 Selection of Mesh Size

Generally speaking, the partitioning radius  $R$  of the free surface model should be determined according to the decaying rate of local waves. However, it is also common to use an approximation proposed in [DNV \(1994\)](#):  $R \sim O(h)$  for shallow water and  $R \sim O(\lambda)$  for deep water. In this case, the water depth is only  $200m$ , whereas the largest wave length is  $872m$  that is more than 4 times of the water depth. Hence a shallow water can be assumed and the radius of the free surface is defined as  $200m$  initially.

The mesh geometry for the free surface model is defined in [Figure 4.7](#). The inner curved edge with radius  $R_0$  must tightly surrounding the TLP panel model. This implies that  $R_0$  equals to TLP hull's radius  $9.9m$ . Even though the meshing of the free surface model is separated from the TLP panel model, the meshing around the intersection area between these two models must

be same. Hence the finer meshing inside the radius  $R_1$  exactly matches the meshing on the TLP hull panel model (See Figure 4.8). The meshing in the domain (between  $R_1$  and  $R_2$ ), which is relatively far away from the panel model, has relatively coarser resolution.  $R_2$  equals to the water depth  $200m$ . Furthermore, An identical number of elements (NC) are distributed on the three curved edge, while distributions NX1 and NX2 are used for the inner straight edge and outer straight edge separately.

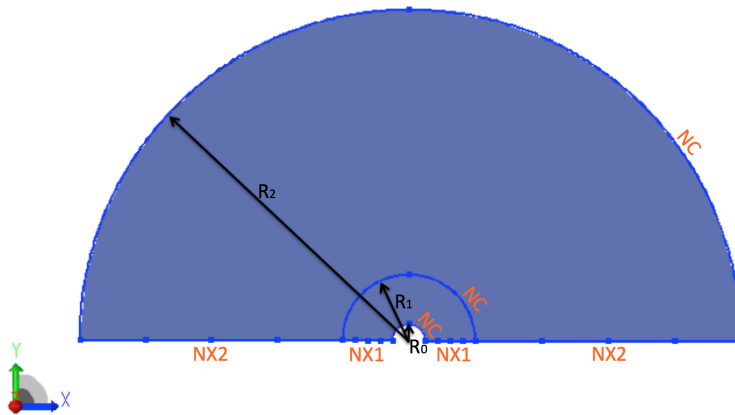


Figure 4.7: Free surface mesh definition for selection of mesh size

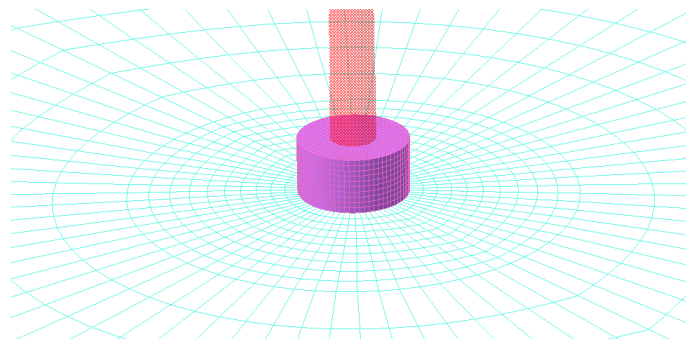


Figure 4.8: The meshing on the intersection of free surface model and TLP panel model

Table 4.1 shows four different meshing cases and their corresponding meshing plots are illustrated in Figure 4.9 - 4.12. The meshing is finer and finer in these four cases, resulting in more accurate results. Mesh case 4 is supposed to provide most accurate result.

Usually TLP structures are sensitive to second-order loads due to its stiff tendons. The

Table 4.1: Free surface configuration with different mesh size for the meshing convergency test

	Mesh 1	Mesh 2	Mesh 3	Mesh 4
R0 (m)	9.9	9.9	9.9	9.9
R1 (m)	40	40	40	40
R2 (m)	200	200	200	200
NC	36	36	36	72
NX1/NX2	5	10	20	20
No. of free surface elements	360	720	1440	2880

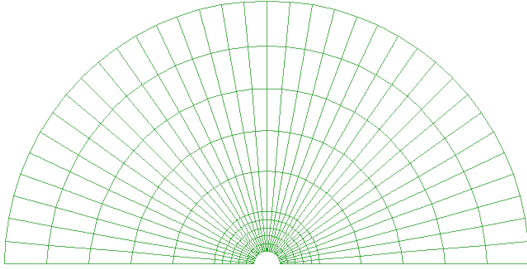


Figure 4.9: Mesh 1

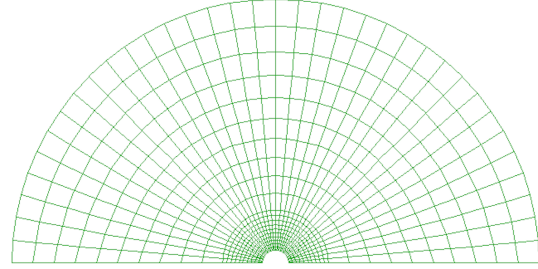


Figure 4.10: Mesh 2

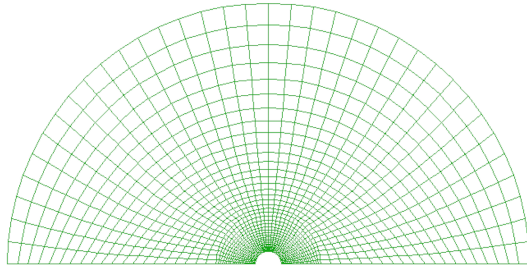


Figure 4.11: Mesh 3

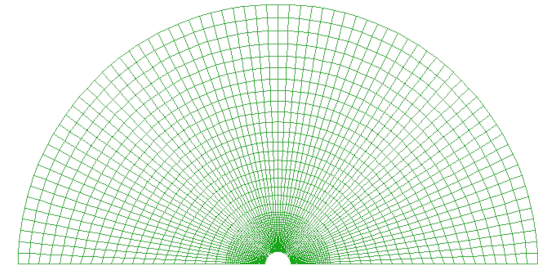


Figure 4.12: Mesh 4

second-order sum-frequency loads may excite heave, roll and pitch motions, while the second-order difference-frequency loads may excite surge and sway modes. Hence the QTFs are defined as index for selecting the idea mesh case.

After performing Wadam Wizard in HydroD, the quadratic second-order forces calculated by pressure integration, which can be read in Wamit files. Note the data output evaluated by Wamit V6.4S are all in a standard non-dimensional form. Therefore the second-order wave forces and moments are converted to real values by using Eq. 4.14 - Eq. 4.13 (WAMIT (1998)). All second-order outputs satisfy symmetry relations  $F/M_{ij}^+ = F/M_{ji}^+$  and  $F/M_{ij}^- = F/M_{ji}^-$ . Here + denotes sum frequency quantity, whereas - denotes difference frequency quantity.  $ij$  or  $ji$  gives the

location of output in second-order force/moment matrix.

$$\bar{F}^+ = \frac{F^+}{\rho g L A_i A_j} \quad (4.10)$$

$$\bar{F}^- = \frac{F^-}{\rho g L A_i A_j^*} \quad (4.11)$$

$$\bar{M}^+ = \frac{M^+}{\rho g L^2 A_i A_j} \quad (4.12)$$

$$\bar{M}^- = \frac{M^-}{\rho g L^2 A_i A_j} \quad (4.13)$$

Where  $L = 100m$  is the characteristic length;  $A_i = A_j = 1m$  represent the complex first-order incident wave amplitudes;  $\rho = 1025kg/m^3$  is the fluid density and  $g = 9.80665kg/m^2$  is the gravity acceleration.

The second-order response amplitude operator at sum- and difference-frequencies are defined as [WAMIT \(1998\)](#):

$$\bar{\xi}^+ = \frac{\xi^+}{A_i A_j / L^n} \quad \bar{\xi}^- = \frac{\xi^-}{A_i A_j / L^n} \quad (4.14)$$

Where  $n = 1$  for the translational modes  $k = 1, 2, 3$  and  $n = 2$  for the rotational modes  $k = 4, 5, 6$ .

Figure 4.13 - Figure 4.16 illustrate the sum-frequency QTFs in heave direction for the four mesh case 1-4. The x- axis and y- axis are the frequencies of the two incoming waves while z- axis represents the amplitude of the sum-frequency QTF. Virtually, the QTF can be considered as the second-order forces for unit wave amplitudes. Apparently, there are small differences among the results of these four meshing cases. The sum-frequency heave force has a magnitude of  $10^3N$  which is 1000 times less than that of the first-order heave force (Figure 4.28(b)). The heave QTF generally increases with frequency. In addition, the obtained sum-frequency belongs to a range of  $0.1 - 3rad/s$ , whereas the heave natural frequency ( $11.42rad/s$ ) is so high. It is unlikely to be excited.

Similarly, the QTF plots in other motions are given in Appendix C. More detailed discusses about QTFs are given in Section 4.4.1.

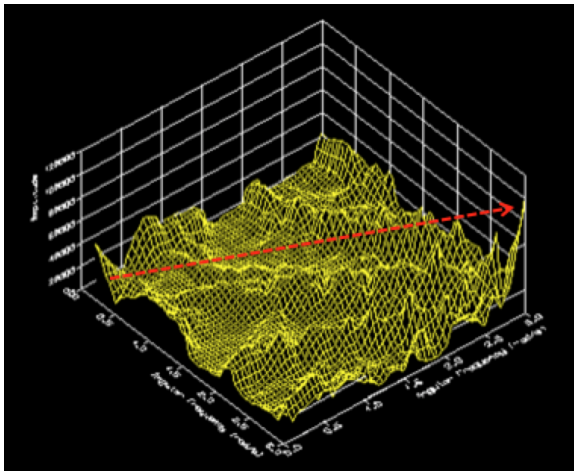


Figure 4.13: Mesh 1 sum-freq. QTF in heave

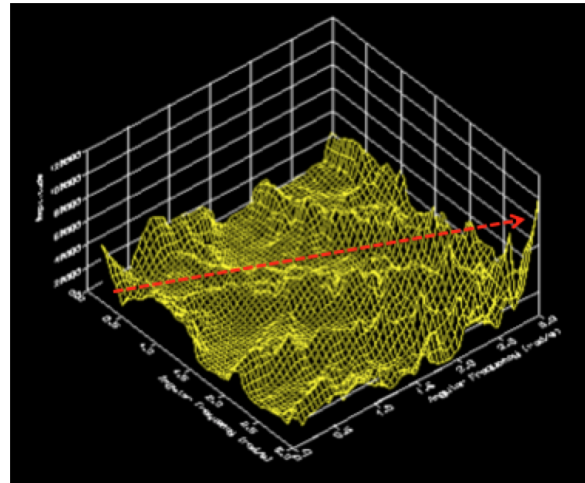


Figure 4.14: Mesh 2 sum-freq. QTF in heave

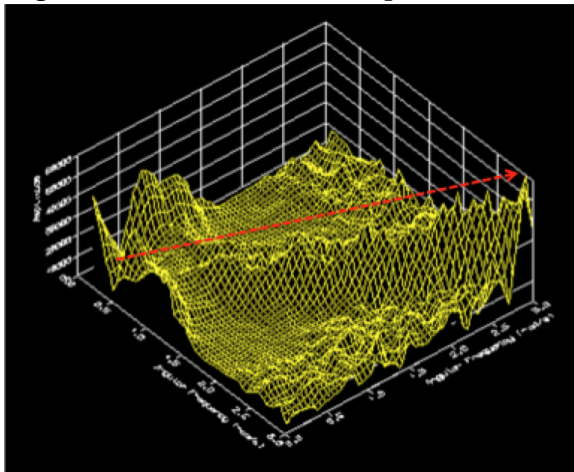


Figure 4.15: Mesh 3 sum-freq. QTF in heave

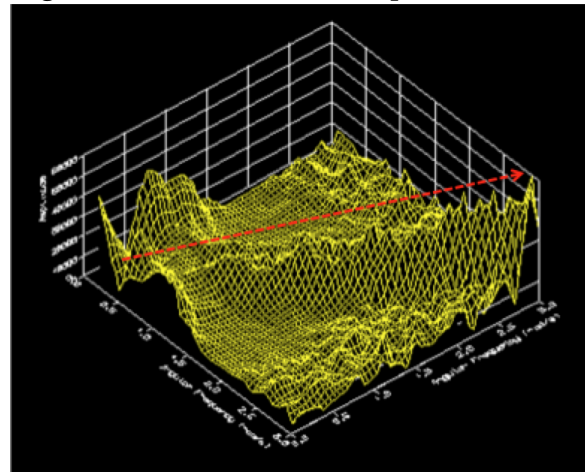


Figure 4.16: Mesh 4 sum-freq. QTF in heave

In order to select proper mesh density, the diagonal sum-frequency heave QTFs for the four mesh cases are plotted in Figure 4.17(a). The results agree quite well for high frequencies except for a little bit deviations at low frequencies. Finer resolution contributes to a more accurate result in mesh 4. The similarity between mesh 3 and mesh 4 soundly demonstrates that the size of mesh 3 is sufficient for an accurate result in heave direction. In the same way, Figure 4.17(b) shows the comparison of diagonal sum-frequency pitch QTF for mesh case 1-4. The pitch QTF



maintains a high degree of consistency. Furthermore, it trends to be high at the surge natural frequency. Figure 4.17(c) shows the diagonal sum-frequency roll QTF for the four mesh cases. The QTF results also have good agreement in high frequency but some difference at low frequency. However, the roll force (Figure 4.17(c)) is considered negligible since its magnitude is much smaller than others. The surge QTF (Figure 4.17(d)) also shows that mesh case 3 with element number 1440 is the ideal choice for second-order calculations.

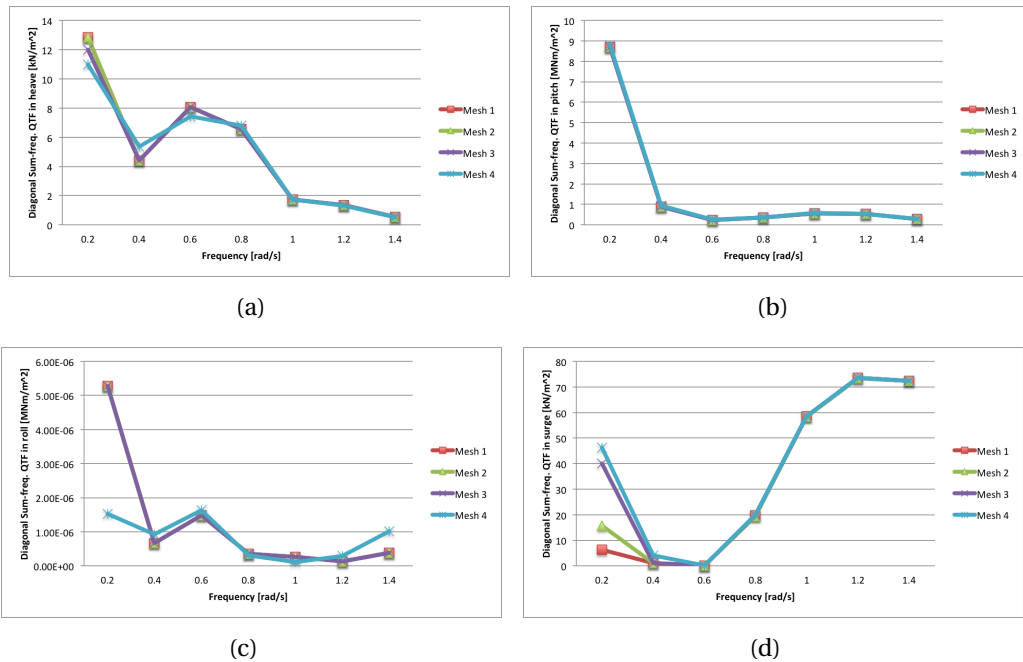


Figure 4.17: Diagonal QTFs in heave, pitch, roll and surge over incoming wave frequency for mesh case 1, 2 and 3

### 4.2.2 Selection of Free-surface Radius

Section 4.2.a has already selected mesh 3 as the optimum mesh size for specific surface radius  $200m$ , so this section will focus on the effects of changing of free-surface radius. The results from three radiuses,  $200m$ ,  $250m$  and  $300m$ , are compared. Figure 4.18 shows the meshing definition and Table 4.2 lists the meshing conditions of the three free surface models.

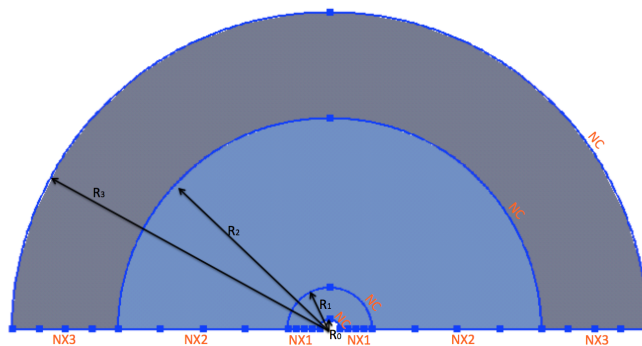


Figure 4.18: Free surface mesh definition for selection of surface radius

Table 4.2: Free surface configuration with different partition radius for the meshing convergency test

	Mesh 3	Mesh 5	Mesh 6
R0 (m)	9.9	9.9	9.9
R1 (m)	40	40	40
R2 (m)	200	200	200
R3 (m)	200	250	300
NC	36	36	36
NX1/NX2	20	20	20
NX3	0	4	8
No. of free surface elements	1440	1584	1728

Figure 4.19 - Figure 4.21 show the plottings of mesh case 3, 5 and 6 respectively. Note that within the radius  $R_2 = 200m$ , the meshing conditions of mesh 5 and mesh 6 are exactly the same as that of mesh 3. However, the radius of mesh 5 and mesh 6 are larger than water depth  $200m$  so that they are deemed to account for more waves during the analysis.

Figure 4.22(a) and Figure 4.22(b) illustrate the trends of diagonal QTFs for mesh case 5 and 6 are identical as that of mesh case 3. This means that mesh 3 with partition radius  $200m$  is

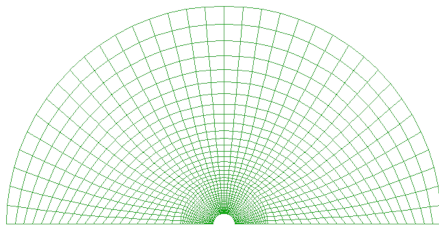


Figure 4.19: Mesh 3

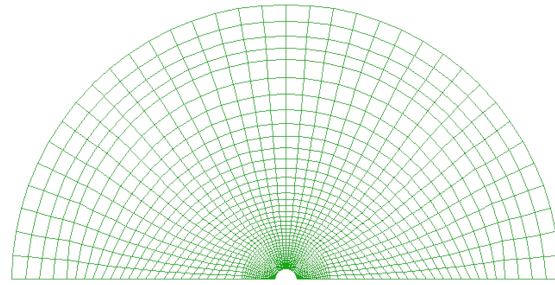


Figure 4.20: Mesh 5

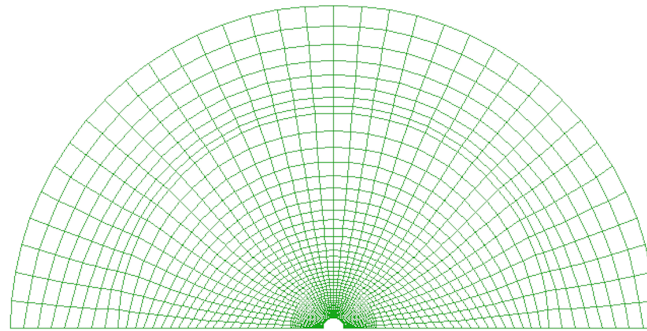


Figure 4.21: Mesh 6

sufficient for the second-order loads calculation.

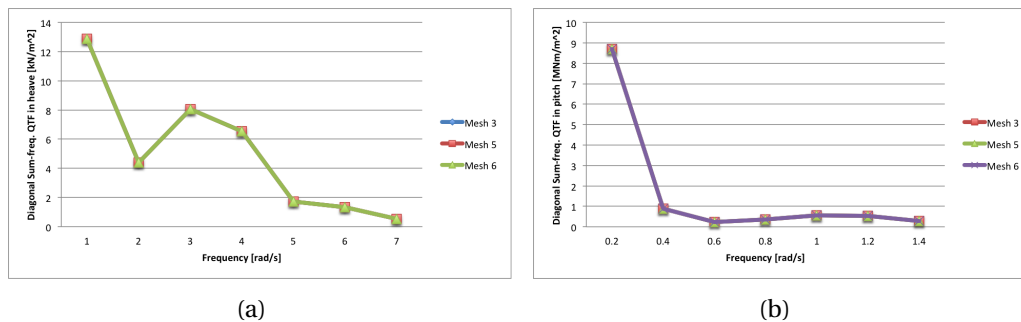


Figure 4.22: Diagonal QTFs in heave and pitch over incoming wave frequency for mesh case 3, 5 and 6

Figure 4.23 gives an overview of the meshed TLPWT (1 m) and the second-order free surface model (mesh 3). This meshed model and free surface are involved into second-order frequency-domain hydrodynamic analysis in Section 4.4.

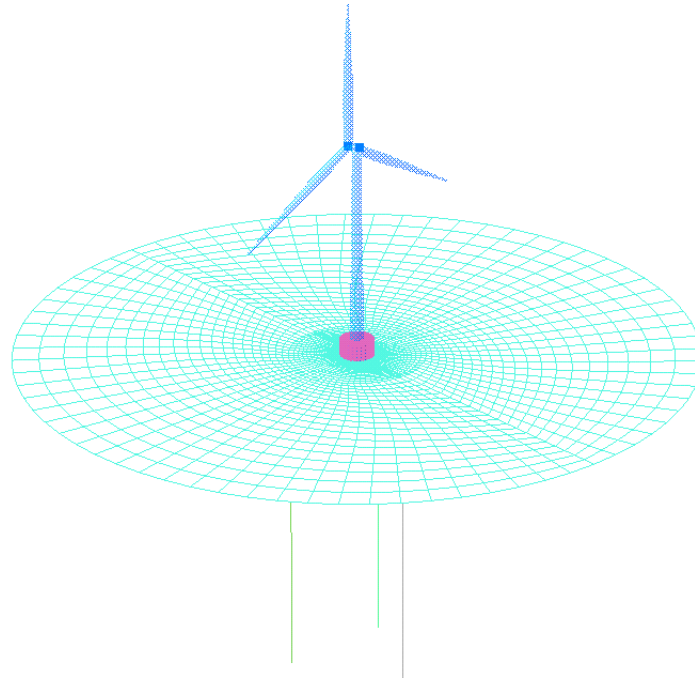


Figure 4.23: Overview of the whole structure and free surface model with mesh 3

### 4.3 First-order Hydrodynamic Results

After establishing the models based on a spreadsheet analysis, the first-order potential for the TLPWT hull is computed using the 3D panel capability in the Wadam, which is based on the well-known WAMIT software [DNV \(2010b\)](#). This section discusses the obtained results, including hydrodynamic coefficients, first-order RAOs and excitation forces. The frequency-domain analysis for first-order loads only uses the TLPWT model in head sea with unit wave amplitude (See [Figure 4.24](#)). 30 frequencies ( $0.1 - 3 \text{ rad/s}$  with step  $0.1 \text{ rad/s}$ ) are applied in the analysis. The Wadam results include real value, imaginary value, amplitude and phase of hydrodynamic coefficients, but only the amplitude of the coefficients are discussed in this section.

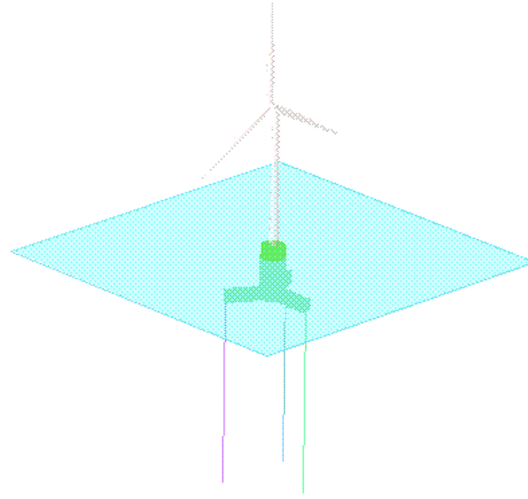


Figure 4.24: TLPWT model used for the first-order calculation in HydroD

### 4.3.1 Added Mass

Due to symmetry of the geometry of the TLPWT, the added coefficients of surge and sway, pitch and roll are the same. The added masses are steady-state hydrodynamic forces and moments due to harmonic rigid body motions in calm water. There are a total of 36 coefficients in a full added mass matrix according to Eq. 2.55.

Figure 4.25 shows the diagonal added mass matrix in 6 DOF. It can be seen that added mass coefficients have strong frequency dependence in low frequency region  $\omega < 2 \text{ rad/s}$ , as discussed in Section 2.3.1. But when wave frequency  $\omega > 2 \text{ rad/s}$ , the added mass coefficients become constant. The added mass in horizontal direction ( $A_{11}$ ,  $A_{22}$ ) is almost the same as the original structure mass.  $A_{33}$  is the smaller because the cross-section area in heave motion is the smallest. It is noted that the three pontoons are included in the potential flow model, leading to non-zero  $A_{66}$ .

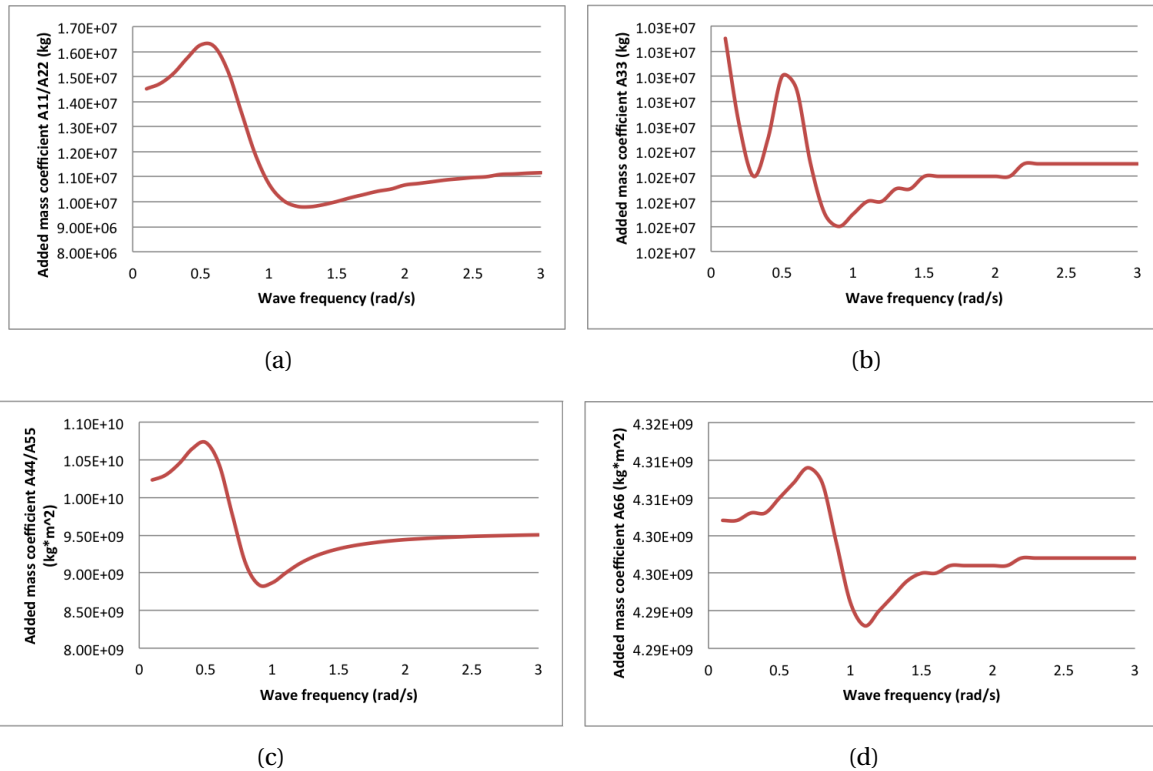


Figure 4.25: Added mass coefficient amplitude in 6 DOF  $A_{11}$ ,  $A_{22}$ ,  $A_{33}$ ,  $A_{44}/A_{55}$ ,  $A_{66}$  (head sea)

### 4.3.2 Potential Damping

Figure 4.26 shows that the potential damping coefficients are also function of excitation frequency. However, the potential damping is banded to wave frequency region  $0.5 - 1.5 \text{ rad/s}$  and it approaches to zero in the low and high frequency limits.

As mentioned in Section 2.3.1, the potential damping relates to the capability of the body to generate waves. In long waves, the TLPWT follows the waves rather than interacts with the waves, so that the generated waves must be small. This explains why the potential damping in low-frequency region trends to be zero. Linear and quadratic damping is further discussed in Section 5.1.

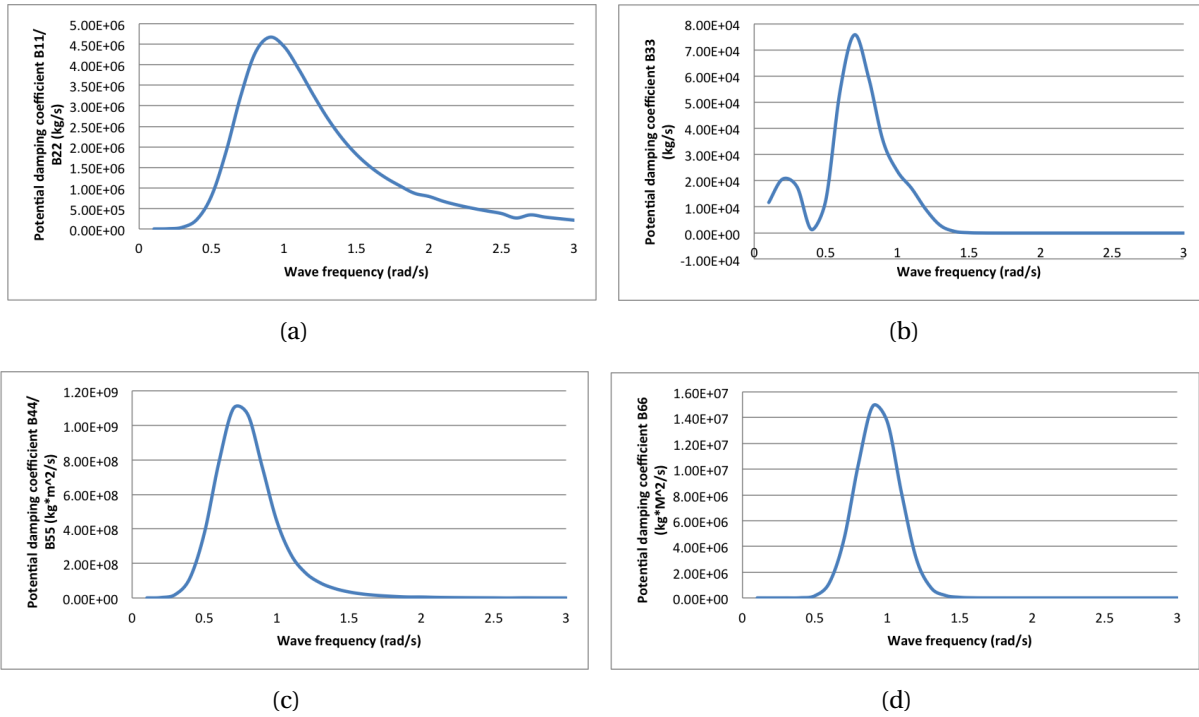


Figure 4.26: Potential damping coefficient amplitude in 6 DOF  $B_{11}$ ,  $B_{22}$ ,  $B_{33}$ ,  $B_{44}$  /  $B_{55}$ ,  $B_{66}$  (head sea)

### 4.3.3 Viscous Damping

As mentioned in Section 2.2.1, The viscous damping is of importance in long waves. In the frequency domain analysis, a linearized drag velocity ( $2m/s$ ) is used on all Morison elements to calculate the drag force (Eq. 2.45).

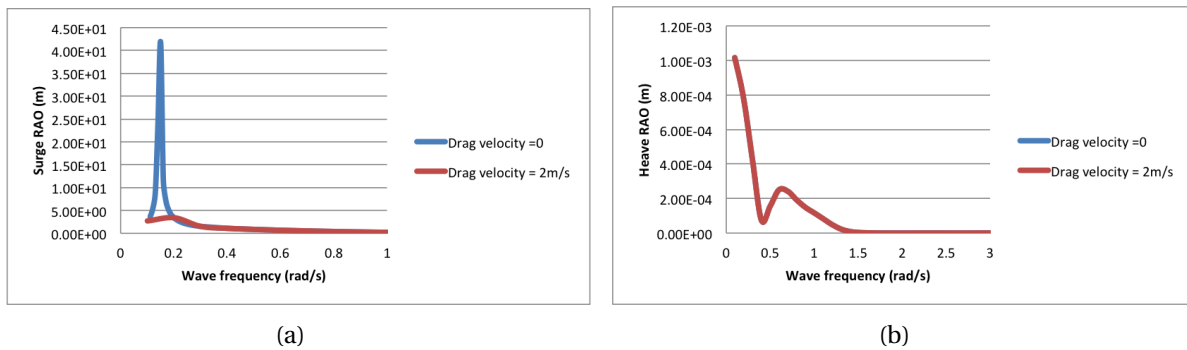


Figure 4.27: Comparison of surge RAO between the model with drag velocity  $2m/s$  and without drag velocity in frequency domain analysis

To examine the effects of viscous effects, the computed surge and heave RAO of the TLPWT

are compared with that of a TLPWT model without including drag velocity. Figure 4.27(a) show that viscous damping helps to reduce the surge resonance in a large degree. However, the viscous damping effects is less obvious in heave motion since the heave natural frequency is too high, see Figure 4.27(b).

### 4.3.4 Excitation Forces

The first-order wave excitation forces based on the potential flow solution are shown in Figure 4.28. Since the waves come in head sea, the sway force and yaw moment are zero. And the pitch moment is identical to roll moment due to the symmetry of the TLPWT. Furthermore, the surge, heave and pitch motions coincide with the incoming wave frequency  $0.6\text{rad/s}$ . This is because the interference of the structure geometry and certain incoming wave. Cancellation effects can be seen in the heave excitation force. There is very little first-order forcing above  $2\text{rad/s}$ .

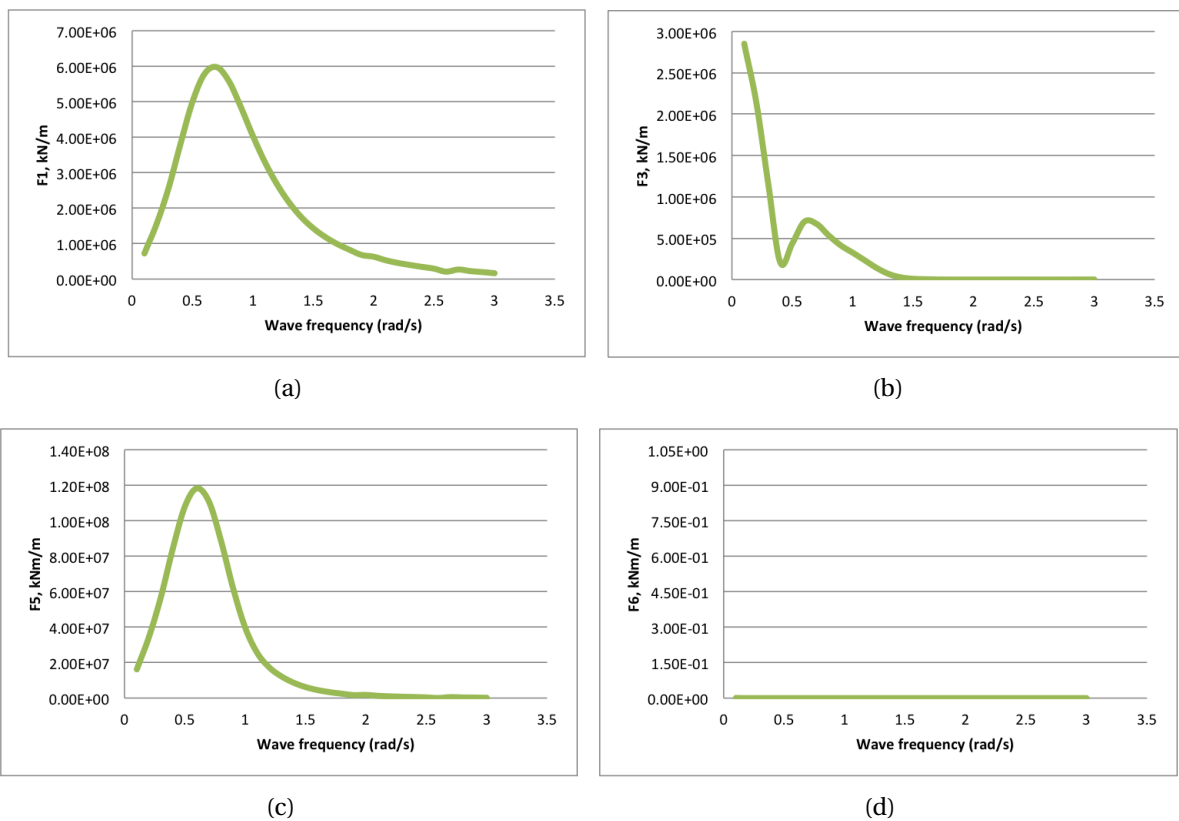


Figure 4.28: First-order wave force excitation amplitude per unit wave amplitude in surge, heave, pitch and yaw (head sea)



### 4.3.5 First-order RAO

Figure 4.29 shows the surge, heave, pitch and yaw amplitude operator. The maximum surge motion occurs at surge natural frequency  $0.14\text{rad/s}$  (Table 5.2), while the maximum yaw motion occurs at yaw natural frequency  $0.30\text{rad/s}$ . In addition, both heave and pitch motions of the TLPWT excite at surge natural frequency. This implies that the heave and pitch motion are coupled kinematically with the surge motion, which is the so-called 'set-down' effect. It should be noted that cancellation effects can be seen in heave response. Furthermore, the spoke-generated waves contribute to the fluctuations shown in the pitch motion.

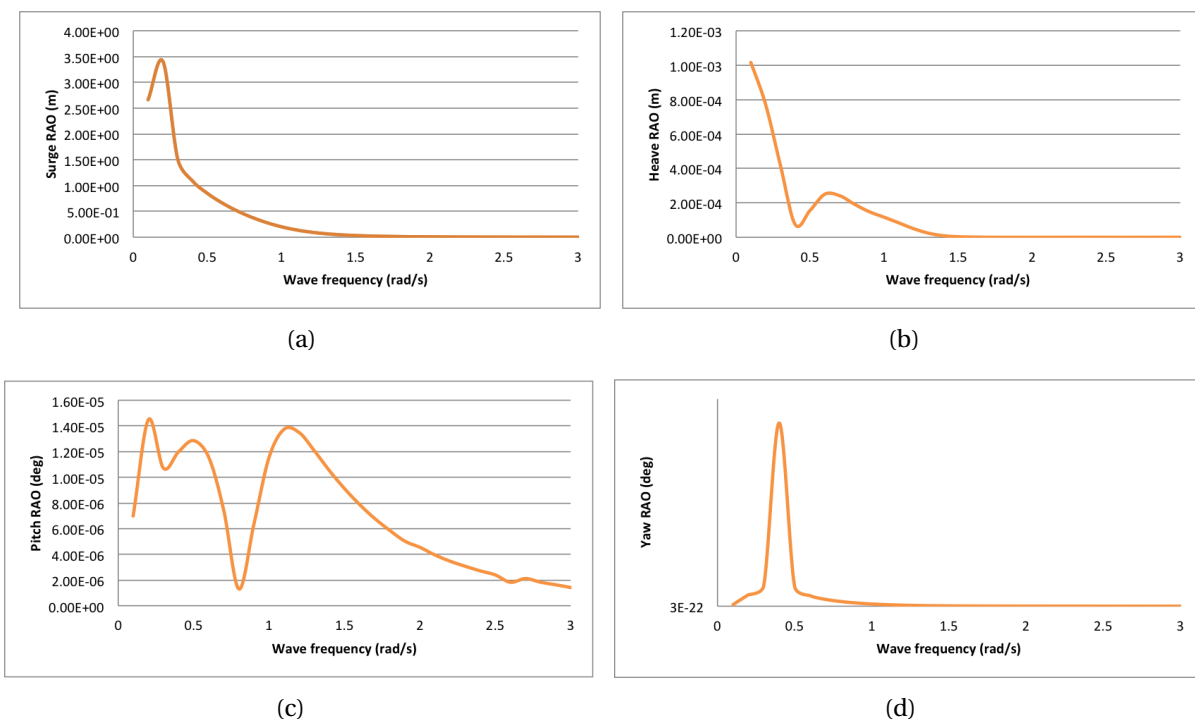


Figure 4.29: First-order wave force excitation amplitude per unit wave amplitude in surge, heave, pitch and yaw (head sea)

## 4.4 Second-order Hydrodynamic Results

Section 2.3.2 introduces the basic theories regarding to second-order potential theory. According to Table 5.2, the TLPWT has really small natural periods in heave, roll and pitch motions. In this case, it is necessary to check the second-order effects on the TLPWT. Therefore this sec-

tion tests the sum-frequency force (Section 4.4.1), difference-frequency force (Section 4.4.2) and Second-order motions (Section 4.4.3). The second-order wave loads and motions are calculated in Wadam by using indirect method All the results presented in this section comes from TLPWT model (Figure 4.23), which free surface are meshing with mesh case 3.

### 4.4.1 Sum-frequency Transfer Force

Figure 4.30 and Figure 4.31 show the sum-frequency QTF in heave and pitch for the TLPWT respectively. As shown, the heave and pitch QTFs trend to grow constantly for increasing frequency especially in diagonal. Comparing Figure 4.30 and Figure 4.31 to Figure 4.28(b) and Figure 4.28(c) respectively, it can be seen that the second-order loads are negligible in low frequencies, but become more significant in high frequencies. The magnitude of the second-order loads is about 1000 times less than that of the first-order loads. The peak of heave QTF is at pitch/bending natural frequency, while the peak of pitch QTF is at right end of its diagonal line.

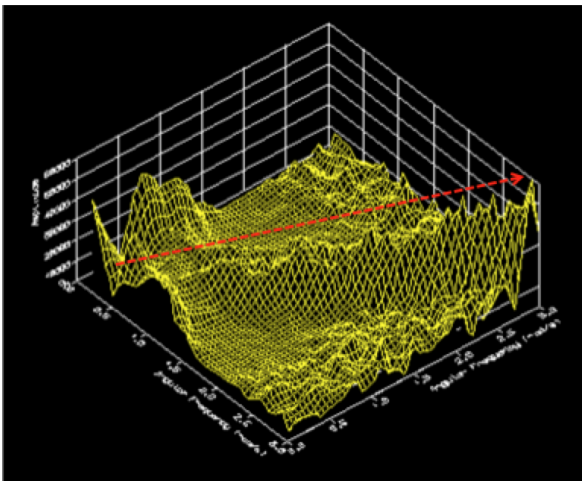


Figure 4.30: Sum-freq. QTF in heave

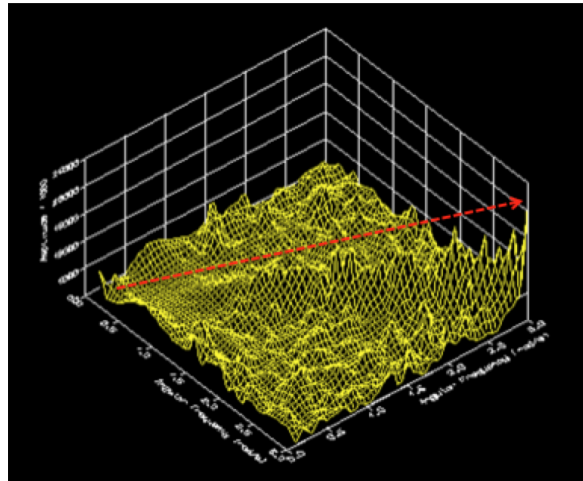


Figure 4.31: Sum-freq. QTF in pitch

### 4.4.2 Difference-frequency Transfer Force

Figure 4.32 shows the distribution of surge difference-frequency QTF for various wave frequency packages. The maximum of the QTF coincides with the surge natural frequency  $0.14rad/s$ . Indeed, the diagonal of the QTF ( $w_1 = w_2$ ) is the so-called mean drift force , which is shown in

Figure 4.33. The drift force depends on wave heading angle and wavelength. This project only applies head sea to the frequency-domain analysis. It can be seen from the figure that the mean drift force is small in long waves but large in short waves. Furthermore, the magnitude of the mean surge drift force is also approximately 100 times less than that of the surge excitation force (Figure 4.28(a)). In addition, by interference between waves generated from different pontoons of the TLPWT, the drift force may become small in certain wavelengths and headings, e.g. the drops shown in Figure 4.33.

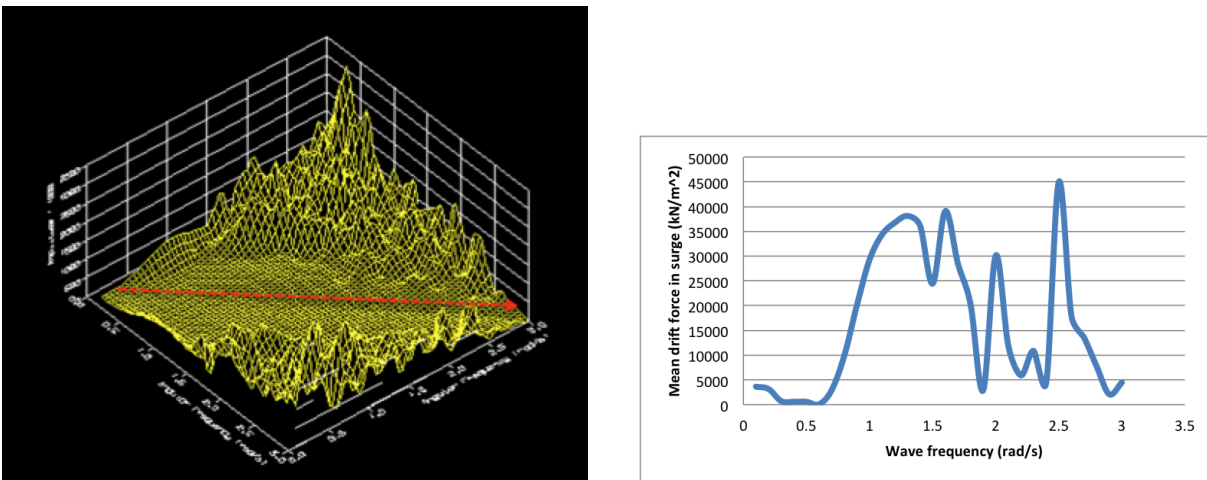


Figure 4.32: Difference-frequency QTF in surge Figure 4.33: Mean drift force in surge (head sea)

#### 4.4.3 Second-order Quadratic Transfer Motion

The first-order motions usually depend on the geometry of the structure, but the second-order motions are much more complicated. The second-order solution is inherently coupled, depending not only on geometry but also on the first-order motions, mass, damping, the stiffness of the mooring system and supported wind turbine [Gueydon et al. \(2015\)](#). The computed second-order transfer motions (QTM) in surge, heave, pitch and yaw are shown in Figure 4.34-4.37 respectively. The surge and yaw QTM are difference-frequency results, while the heave and pitch QTM are sum-frequency results. The peak of surge QTM coincides with the surge natural period  $0.14 \text{ rad/s}$ , while the peak of pitch QTM is at the right end of the diagonal line. The fluctuations in the pitch QTM relates to first-order pitch RAO (Figure 4.29(c)). As the heave natural

frequency  $11.42 \text{ rad/s}$  is too high to reach, there is no excitations presented in heave QTM.

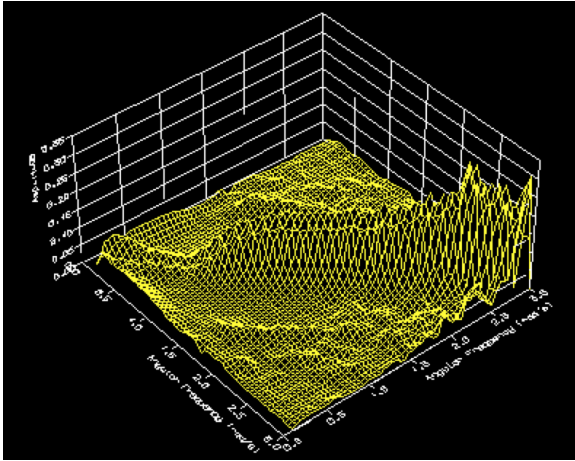


Figure 4.34: Diff-freq. RAO in surge

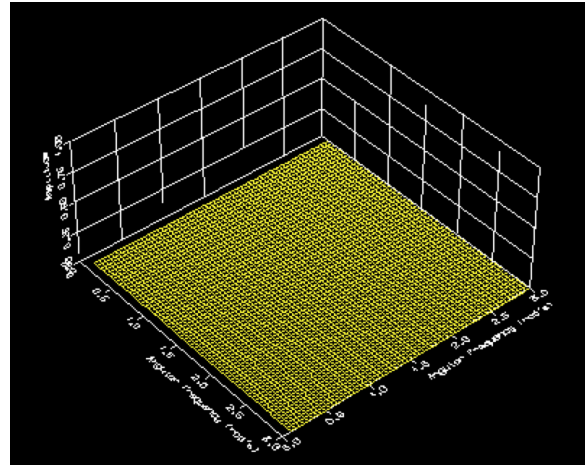


Figure 4.35: Sum-freq. RAO in heave

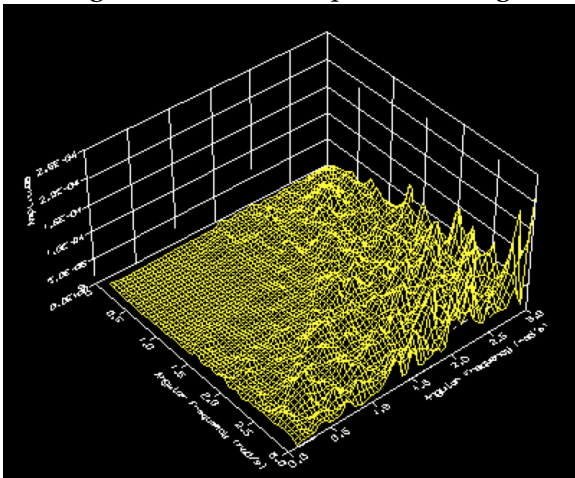


Figure 4.36: Sum-freq. RAO in pitch

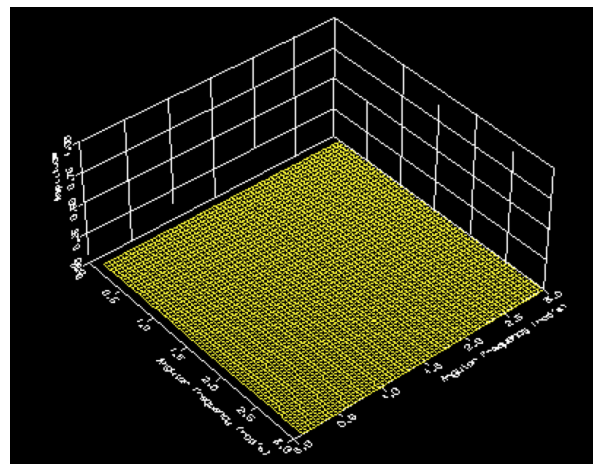


Figure 4.37: Diff-freq. RAO in yaw

# Chapter 5

## Time Domain Dynamic Analysis

Chapter 4 presents the frequency-domain linear analysis for the TLPWT. However, if the non-linear load effects are needed to be considered, the equations of motion (Eq. 2.55) should be solved in time-domain. In the time-domain analysis, the frequency-dependence can be included through the convolution integral approach [MARINTEK \(2012b\)](#). This approach has already been introduced in Section 2.4.2.

By using the state-of-art code SIMO-REFLEX-AeroDyn (SRA) with an external controller, the nonlinear dynamic simulations are carried out. It accounts for the turbulent wind inflow, aerodynamics, hydrodynamics, control dynamics, structural mechanics and tendon dynamics. Computation is performed in every time step. The introduction for SRA can be read also in Section 2.5.2.

Prior to run SRA code, the Wadam G1.SIF file (obtained from frequency-domain analysis) is supposed to be converted to a sys.dat file via DeepC. Appendix D gives details for this generation process. The combined sys.dat file is then used to build a SIMO-RIFLEX coupled TLPWT model in SIMA. SIMA is a graphical user interface for RIFLEX and SIMO. The body data in original sys.dat file accounts for only relates to the TLP floater, and the DTU 10MW wind turbine (a RIFLEX model, see Appendix E) and tendon system are modeled directly in SIMA. Figure 5.1 shows an overview of the TLPWT model in SIMA.

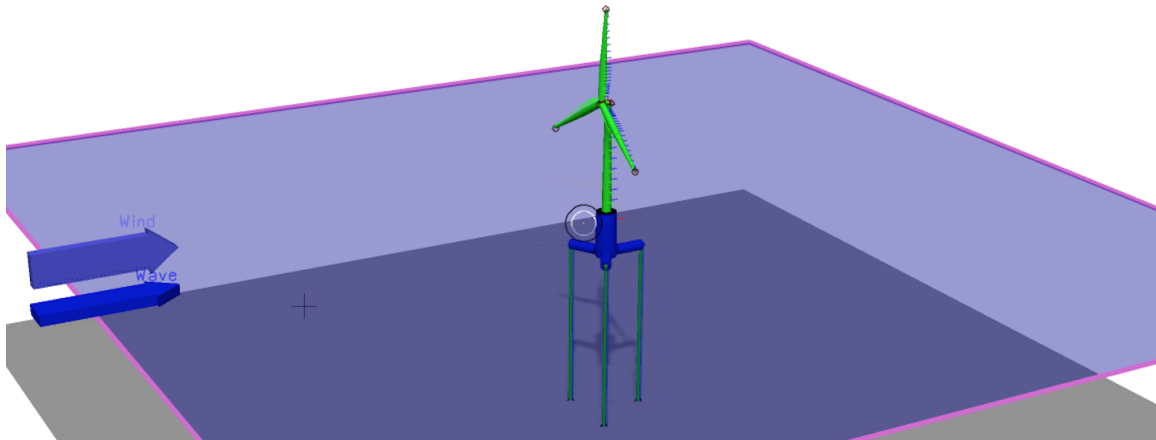


Figure 5.1: Overview of the TLPWT in SIMA

The structural model of the tendons in SIMA includes both bending and axial stiffness. The anchor points are modeled as fixed in translation but free in rotation. Furthermore, there is a flexible coupling at the fairlead as well, such that the tendons can be considered as pin-pinned beams.

The flow added mass, radiation damping and excitation on the hull will be calculated based on first-order flow theory in SIMA. Besides, the input `sys.dat` file only includes sum-frequency QTF and mean wave drift force coefficients, and the difference-frequency loads on the hull are computed according to Newman's approximation in SIMA. This approximation is described in Section 2.3.2.

Then the following files are used for SRA run. The first four files are generated from SIMA while the three Macro files are modified based on Erin's macro files for TLPWT#3 [Bachynski \(2014\)](#). In addition, several files regarding to AeroDyn input (`Aerodyn.ipt`), airfoil information (`AirfoilLibrary.dat`), DLL input (`DLLinputs.txt`) and control input (`ControlInput.txt` and `Cotnrolfix-pitch.jar`) are also required for the time-domain analysis.

- `inpmod.inp`
- `stamod.inp`
- `dynmod.inp`

- new sys.dat
- sta.mac
- dyn.mac
- s2x.mac

SIMA has a basic assumption - the floating body is neutrally buoyant without the RIFLEX elements. Hence it is also necessary to correct the mass, COG and restoring matrix of the TLP hull in the original sys.dat file since tower and turbine are explicitly modeled as beams in RIFLEX, and hub and nacelle as rigid bodies in SIMO, with their mass and gravity considered in the mass and restoring matrix respectively. The modification process is referred to Appendix F in [Kvittem \(2014\)](#).

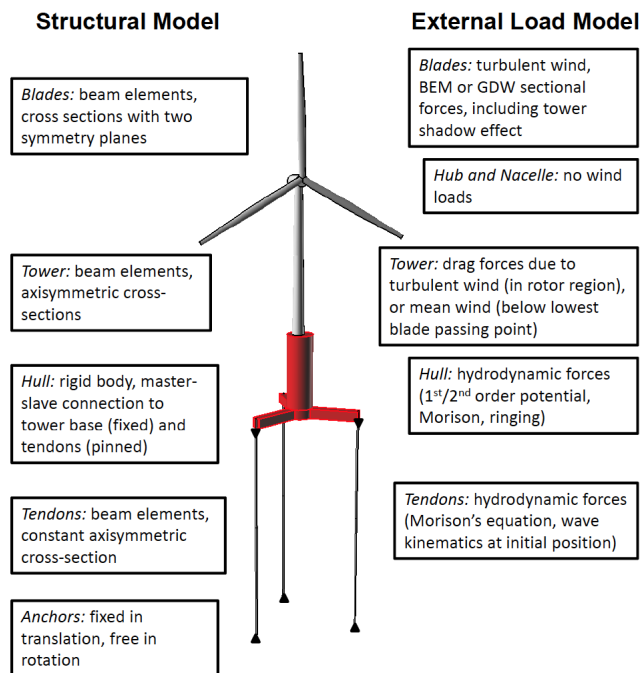


Figure 5.2: Description of the structural model and external load model of the TLPWT [Bachynski \(2014\)](#)

Applying the structural, hydrodynamic, aerodynamic and control theory described in Chapter 2 to the TLPWT model, Figure 5.2 shows the SRA TLPWT model [Bachynski \(2014\)](#), overview-

ing its structural model and external load model. The specifications for the TLPWT model are listed as follows:

- The following specifications are applied to hull, hub and nacelle.
  1. The hull, hub and nacelle are considered as rigid bodies.
  2. The hull acts as the master node for fairleads and turbine tower.
  3. There is no external loads acting on hub or nacelle, but hydrodynamic forces on the hull.
  4. Note that the hydrodynamic forces are always applied on the initial position of the structure, so that the relative phasing among first-order wave forces, second-order forces, Morison load, and ringing loads are correct.
  5. Wave kinematics are used from the mean water surface.
- The following specifications are applied to tendon, tower, shaft, blade and blade eccentricities. More detailed definition for the DTU wind turbine can be found in Appendix E.
  1. The tendons, tower and blades were modeled by flexible beam elements.
  2. The shaft and blade eccentricities were modeled by relatively stiff elements.
  3. Note the tower of original DTU 10MW wind turbine model is cut by  $10m$  from bottom in order to guarantee the  $10m$  freeboard of the TLPWT.
  4. Each tendon is composed of 80 elements, with cross-sectional properties computed for hollow, air-filled tubular steel sections.
  5. The tendon length is specified and a very small vertical stretching length is given in static analysis of the TLPWT. In this way, the pretensions can be applied to the structure.
  6. Normally the Reyleigh damping model is used for structural elements like mooring liens or tendons so that the mass- and stiffness-proportional damping coefficients are applied to tendons.
  7. The anchors are modeled by nodes that are fixed in translation but free in rotation, meaning that the tendons are pinned to the seabed.



8. Pinned connection to the hull are also applied at fairleads.
9. The wind turbine model is directly copied from Qiang Wang's model [Wang \(2014\)](#), which properties are specified referring to [Bak et al. \(2013\)](#).

After setting up all the properties for the TLPWT, a series of time-domain analysis are carried out, such as free decay test (Section 5.1), constant wind test (Section 5.2) and turbulent wind test (Section 5.3).

## 5.1 Free Decay Test

The decay test is performed to document the system natural periods and damping coefficients. The initial displacements of the TLPWT are achieved by applying a ramp force/moment for 50s (50s – 100s), then holding the force/moment constant for another 100s (100s – 200s) and finally releasing the force/moment at point (0, 0, 0) (See [Figure 5.3](#)).

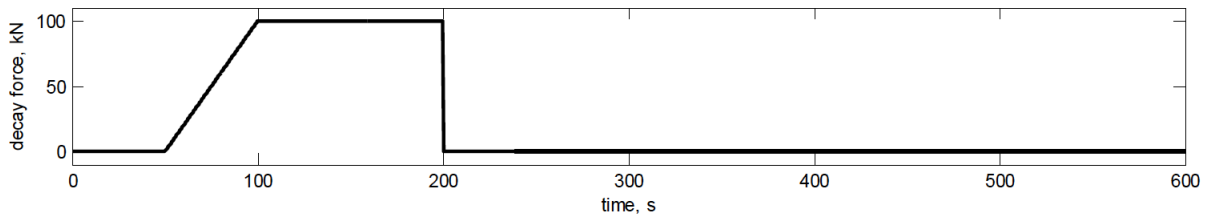


Figure 5.3: Example of decay force with ramp duration 50s and constant force duration 100s

Table [5.1](#) lists the simulation parameters used in the decay test. A specified force/moment is applied on the hull of the TLPWT in different DOF. During the free decay test, the wind turbine is supposed to be parked and its blades to be feathered by rotating its blades 90 degrees, attaching them to tower and keeping them fixed. Additionally, the free decay tests are carried out in calm water ( $H_s = 0.001m$ ,  $T_p = 100s$  and  $U_{wind} = 0$ ) to cancel out the environmental effects. For TLPWTs, in order to get more solid decay test output in heave and pitch, it can be useful to make this time step smaller (e.g. 0.01s) in the Dyn-TLPWT.mac file.

Table 5.1: Simulation parameters for decay test

Motion	Force/Moment	Simulation length	Simulation time step (RIFLEX)	Response time step (SIMO)
Surge	500kN	600s	0.01s	0.1s
Heave	50000kN	300s	0.01s	0.01s
Pitch	260000kNm	300s	0.01s	0.01s
Yaw	260000kNm	600s	0.01s	0.1s

Figure 5.4 - 5.7 present the TLPWT responses in surge, heave, pitch and yaw decay tests respectively. Indeed, the flexibility of the tower has a significant effect on the pitch mode of motion [Matha \(2010\)](#), Figure 5.6 therefore shows two natural periods during the pitch free decay test of this TLPWT. The platform in pitch mode is stiff with small natural period of 0.6s caused by large tendon axial stiffness; while the tower-nacelle-rotor dominates in this case, showing a natural period of 3.49s.

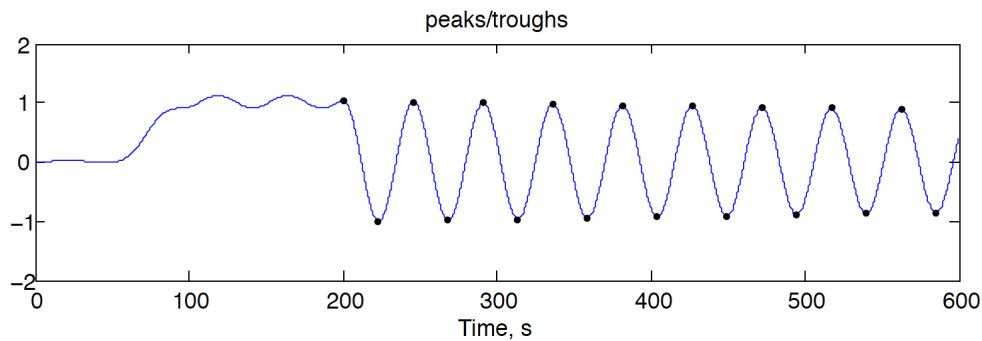


Figure 5.4: TLPWT surge motion (m) in free decay test along time

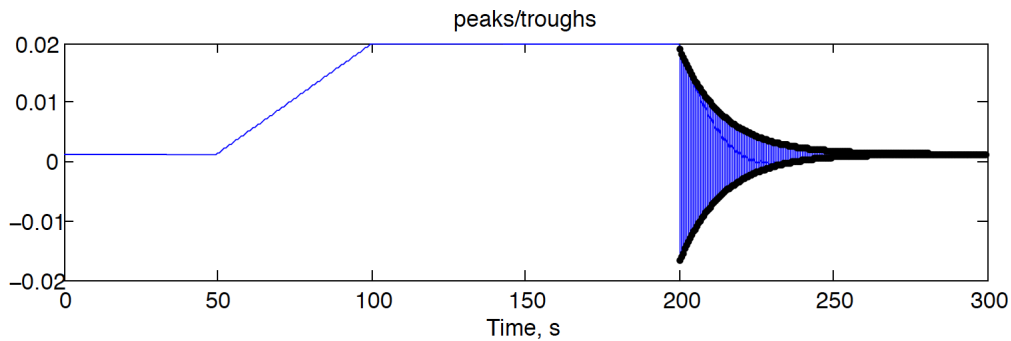


Figure 5.5: TLPWT heave motion (m) in free decay test along time

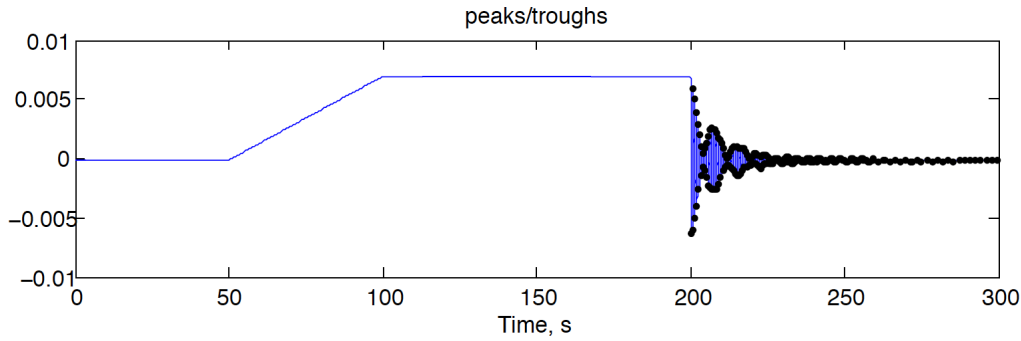


Figure 5.6: TLPWT pitch motion (deg) in free decay test along time

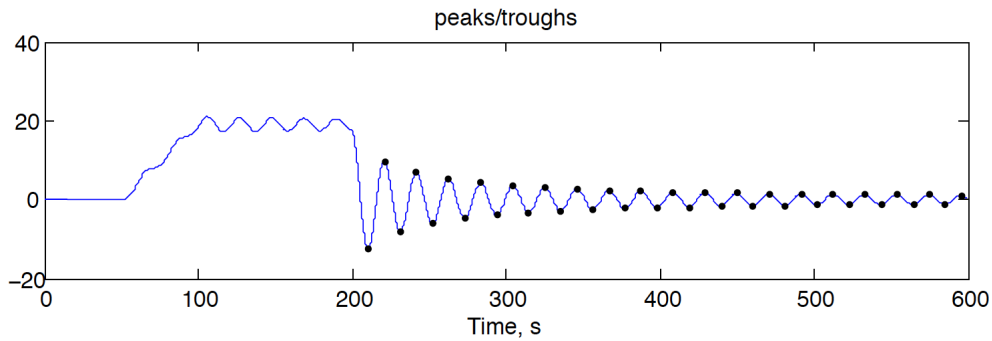


Figure 5.7: TLPWT yaw motion (deg) in free decay test along time WRONG???

For the TLPWT, its restoring forces are dominated by tendon system (can be seen from Table 3.7). The tendons can be reasonably approximated as linear. But the viscous contribution plays an important role in its damping forces in practice. Assuming uncoupled motions, the damping force for any degree of freedom  $\eta$  can be described as Mathisen and Price (1985):

$$F(\dot{\eta}) = b_1 \dot{\eta} + b_2 |\dot{\eta}| \dot{\eta} \quad (5.1)$$

Where  $b_1$  and  $b_2$  are constant linear and quadratic damping coefficients respectively.

In order to estimate the contribution of linear and quadratic damping coefficients, a simulated line (red dotted line in Figure 5.8) is created based on the natural period in this motion. This recreated line should match the original line (blue solid line in Figure 5.8) as much as possible. In this way, proper linear and quadratic damping coefficients can be calculated based on this recreated line. But it is difficult to accurately fitting the damping coefficients from the filtered data series in pitch mode due to the overlapped two natural periods. Therefore, the

damping coefficients for the coupled pitch bending modes are not computed in pitch decay test.

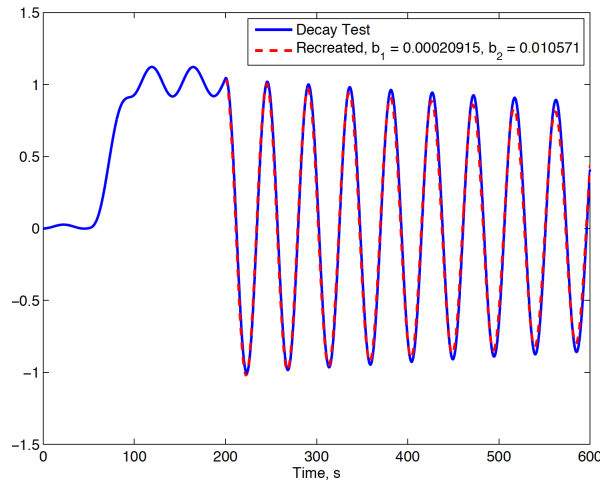


Figure 5.8: Recreated line and original decay line in surge decay test

Table 5.2 lists the natural periods and damping coefficients estimated from each decay test. The obtained natural periods satisfy the TLPWT design criteria in Section 3.1.2. The surge/sway natural period (45.23s) is larger than normal wave period range 3.5 – 25s, while the heave (0.55s) and pitch/roll (0.60s) natural periods are less than that region. This implies that the designed TLPWT is soft in horizontal directions but stiff in vertical directions.

Additionally, the natural periods obtained from decay test have a good consistency with the values from spreadsheet calculations (Table 3.6). The surge/sway, heave and yaw natural periods are of great similarity. However, the pitch/roll natural period (0.60s) is slightly larger than the spreadsheet result (0.53s). This maybe due to the coupling effects between surge and pitch motion. Another possible reason is the weakness of the spreadsheet design. During the spreadsheet calculation, the TLPWT is assumed as a fully rigid body, such that the coupling between pitch/bending is unable to estimate.

Table 5.2: Natural period and damping coefficients based on decay test

Motion	Natural period $T_n$ (s)	Linear damping coefficient $b_1$ (rad/s)	Quadratic damping coefficient $b_2$ (1/m or 1/deg)
Surge/Sway	45.23	0.0020915	0.010571
Heave	0.55	0.18901	0.00000
Pitch/Roll	0.60	-	-
Yaw	20.87	0.0028121	0.014922

Furthermore, Table 5.2 shows that the damping in surge and yaw motion is better described as quadratic damping: the viscous loads acting on center column and pontoons are larger than linear potential damping, especially for low frequencies. On the contrary, the high frequency heave motion has a relatively linear decay process.

## 5.2 Constant Wind Test

In order to examine the mean offset motions and wind turbine performance of the TLPWT in practical operational condition, constant wind tests are performed for wind speeds in region  $4\text{ m/s} - 24\text{ m/s}$ . BEM method is used for wind speed  $U_{wind} < 8\text{ m/s}$  while GDW method is used for wind speed  $U_{wind} \geq 8\text{ m/s}$ . Section 2.1.2 and Section 2.1.3 introduces these two methods in details. Simulation time  $800\text{ s}$  is sufficient to achieve steady outputs in the constant wind test.

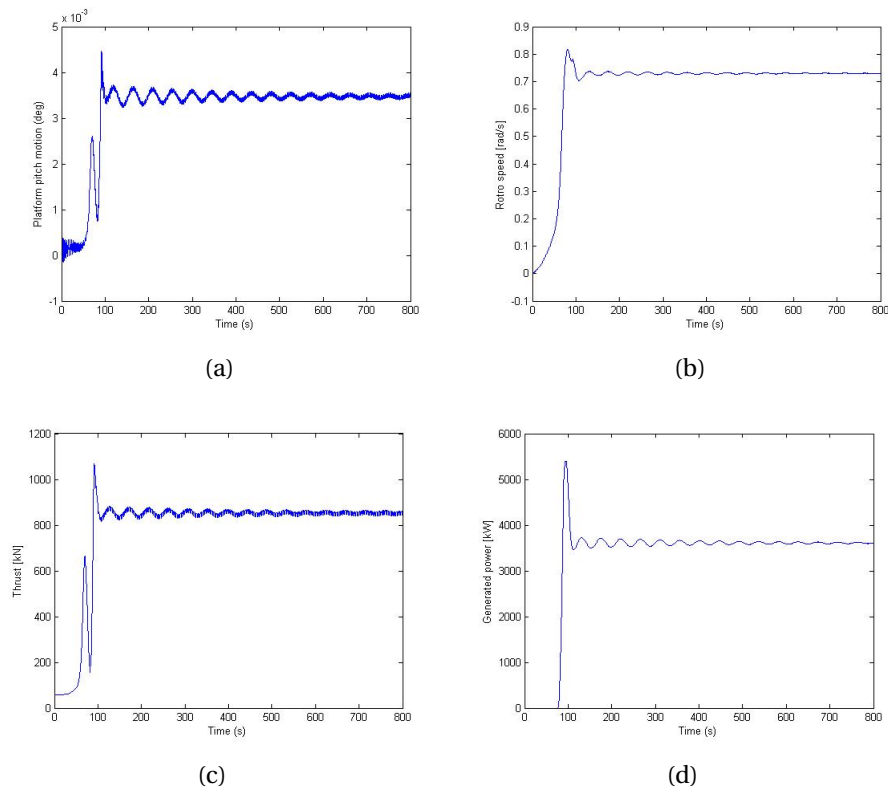


Figure 5.9: Time histories of platform pitch motion, thrust, rotor speed and generated power of the TLPWT under constant wind speed  $8\text{ m/s}$

Figure 5.9 shows an example of aerodynamic results of constant wind test at  $8\text{ m/s}$ . It takes

about 150s for the TLPWT to start up and all parameters become steady. Then these parameters oscillate with time regularly due to the rotation of blades and presence of tower. It can be seen two frequencies involved in the platform pitch motion (Figure 5.9(a)) and thrust force (Figure 5.9(c)). Section 5.1 has mentioned that tower bending contributes to the pitch motion of the TLPWT. As for thrust force, Fast Fourier Transformation (FFT) is applied to the thrust data along time history 150s – 800s in order to assess possible frequencies.

Figure 5.10 shows the calculated thrust spectrum, where the start-up time 0s–150s is filtered. Obviously the frequency 0.341 Hz dominates the oscillation of thrust force, which is about 3 times of the rotor frequency 0.113 Hz corresponding to rotor speed 0.712 rad/s in Figure 5.9(b). This is the so-called '3P frequency effects'. The blades of the wind turbine passing in front of the tower will cause a shadow effect and produce a loss of wind load on tower Dolan and Lehn (2006).

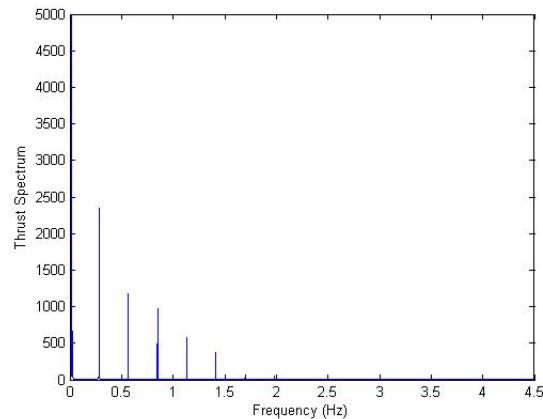


Figure 5.10: Thrust spectrum after FFT transformation at constant wind speed 8 m/s

Figure 5.11 shows the change of blade pitch angle and Figure 5.12 presents the test results in different constant wind speed. All the statistics are mean values taken after the plotted result curves tending to be stable. This TLPWT uses a Pitch-Regulated Variable Speed (PRVS) control system Bachynski (2014) to regulate the power output and structural loads. As mentioned in Section 3.2, the DTU 10MW wind turbine has a cut-in wind speed of 4 m/s (below which external wind is too little to get effective power) and a cut-out wind speed of 25 m/s (above which the wind turbine must be shut down to avoid potential structural damage). Between the cut-in and

cut-out wind speed region, the PRVS controller is active.

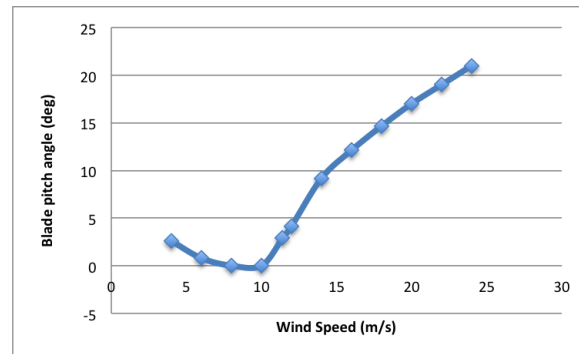
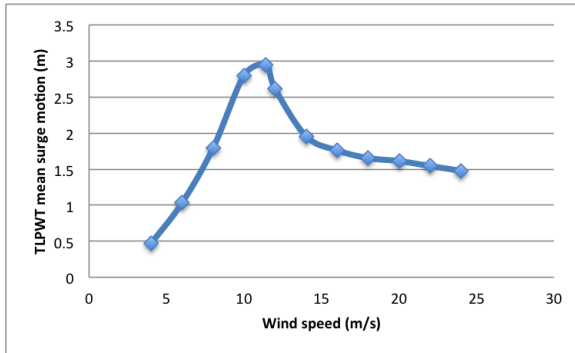
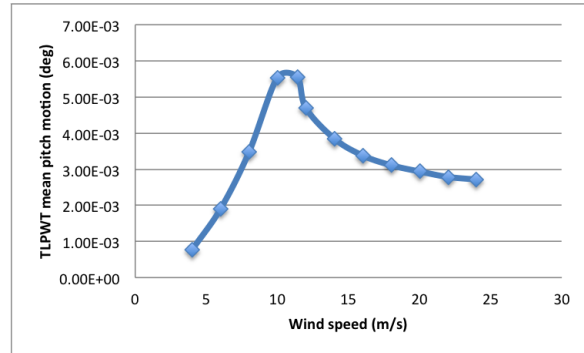


Figure 5.11: Mean blade pitch angle for wind speed  $4m/s$  to  $24m/s$

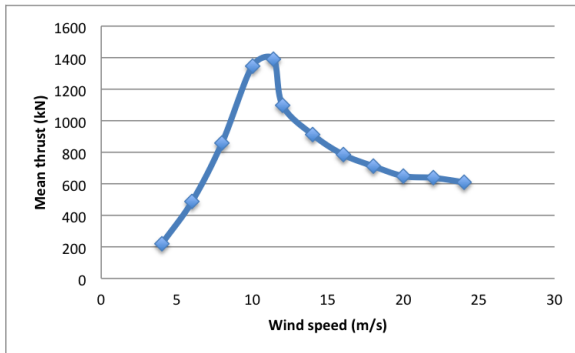
In the below-rated speed region, the blade rarely pitches, but the generator torque varies quadratically such that the wind turbine operates as closely as to the optimal tip speed ratio. In the meantime, the platform motions, wind thrust, generated power and rotor speed also increase quadratically. Once the wind speed equals to the rated speed  $11.4m/s$ , the turbine reaches the rated torque  $9950kNm$ , rated rotor speed  $1.005rad/s$  and rated power  $9440kW$ . Considering the power transfer efficiency 94.4%, the actual generated rated power should be  $10MW$  as expected. In the above-rated speed region, the blade pitch starts varying placidly to minimize the structural loads/motions and keep constant power output. Furthermore, the maximum mean surge motion is only  $3m$ , which has a good agreement with the stability calculation result in Section 4.1. And the pitch motions in all wind speeds are extremely small so that this motion can be ignored.



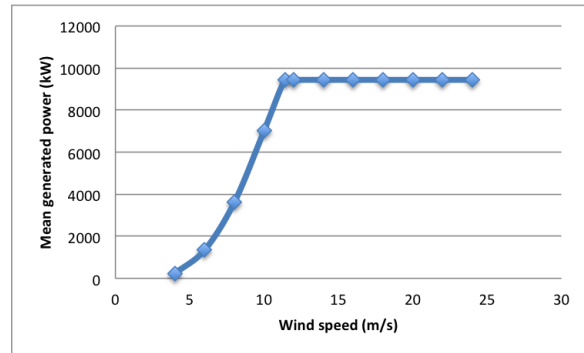
(a)



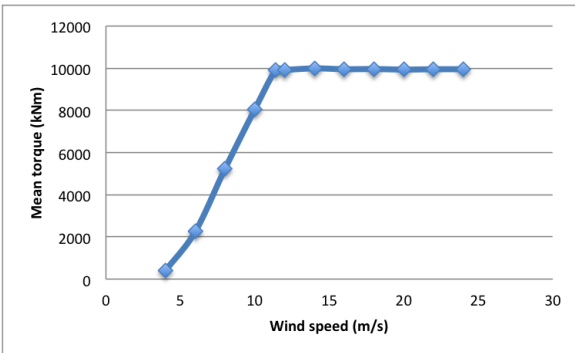
(b)



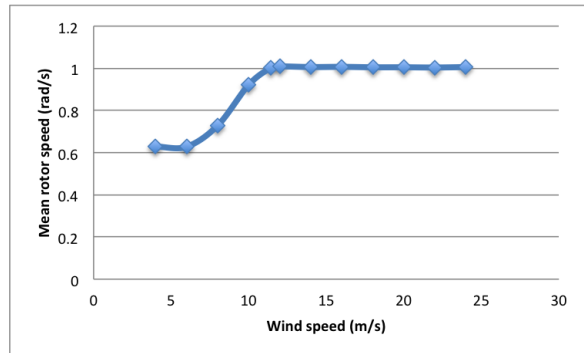
(c)



(d)



(e)



(f)

Figure 5.12: Constant wind test results for wind speed 4m/s to 24m/s



## 5.3 Combined Turbulence Wind and Irregular Wave Test

For offshore floating wind turbines, as the combination of turbulent wind and irregular wave may result in significant response, the results in these cases should be examined carefully to insure the safety of TLPWT. Each simulation lasts 4000s and corresponded to a 1h dynamic analysis, since the first 400s is filtered to eliminate the start-up transient effects. The allowable minimum pitch angles are modified to zero degrees for various wind speeds in the blade pitch controller file.

### 5.3.1 Load Case

The Norway 5 site is selected as a representative site for the conceptual design of the TLPWT, as Site No. 14 in Figure 5.13. The general information regarding to Site No. 14 is listed in Table 5.3.



Figure 5.13: Location of 18 potential European offshore sites [Li et al. \(2015\)](#)

For the TLPWT, the mean wind speed at hub height can be calculated by [Li et al. \(2013\)](#):

$$U_z = U_{10} \left( \frac{z}{10} \right)^\alpha \quad (5.2)$$

Where  $\alpha = 0.1$  should be used for this site;  $z$  is the hub height 119m;  $U_{10}$  is the mean wind speed at the reference height 10m.

Table 5.3: General information and statistics of site 14 in North Sea

Site no.	14
Area	North Sea
Name	Norway 5
Water depth	200m
Distance to shore	30m
Average wind power density at 80m	1094.84W/m <sup>2</sup>
Average wave power density	46.43kW/m
50-year $U_w$ at 10m	33.49(m/s) <sup>a</sup>
50-year $H_s$	10.96m
Mean value of $T_p$	11.06s

The load cases should cover below-rated, rated, above-rated and extreme wind speeds to account for various practical environmental conditions. The extreme condition with a return period of 50 years was obtained by using the contour surface method and the wind and wave data in general operational conditions were fitted with analytical joint distributions [Li et al. \(2013\)](#). The following procedure is used to choose operational load cases:

1. Eq. 5.2 can be used to calculate the mean wind speed at hub height  $U_{119}$ .
2. The conditional distribution of significant wave height  $H_s$  for given mean wind speed  $U_{119}$  is applied. The most probable  $H_s$  should be the peak of the probability density function.
3. The conditional distribution of wave peak period  $T_p$  for given significant wave height  $H_s$  and mean wind speed  $U_{119}$  is applied. The most probable  $T_p$  should be selected in the same way as  $H_s$ .

In addition, the turbulence intensity can be calculated by mean wind speed at hub height  $U_{119}$  [Burton et al. \(2001\)](#):

$$I_u = I_{ref}(0.75 + 5.6/\bar{U}) \quad (5.3)$$

Where  $I_{ref} = 0.16, 0.14, 0.12$  for wind class A, B and C;  $\bar{U}$  is the mean wind speed at hub height. It is recommended to use wind class C for offshore structures [IEC \(2005\)](#) and thus  $I_{ref} = 0.12$  is applied to the calculation of turbulence intensity.

Table 5.4: Load cases for turbulence wind test

Load case	$U_{119}$ (m/s)	$H_s$ (m)	$T_p$ (s)	$I_u$	Turbine status
OP1	8	2	10.3	0.17	Operating
OP2	11.4	2.5	10.2	0.15	Operating
OP3	18	4.1	10.5	0.13	Operating
EX	40	15.6	14.5	0.11	Parked

Table 5.4 gives the four load cases applied in the turbulence wind test. In the first three load case (OP1, OP2 and OP3), the turbine is in normal operational condition with active control. But in the the extreme load case (EX), the blades are pitched to feather and the turbine is shut down to avoid damage in adverse weather conditions.

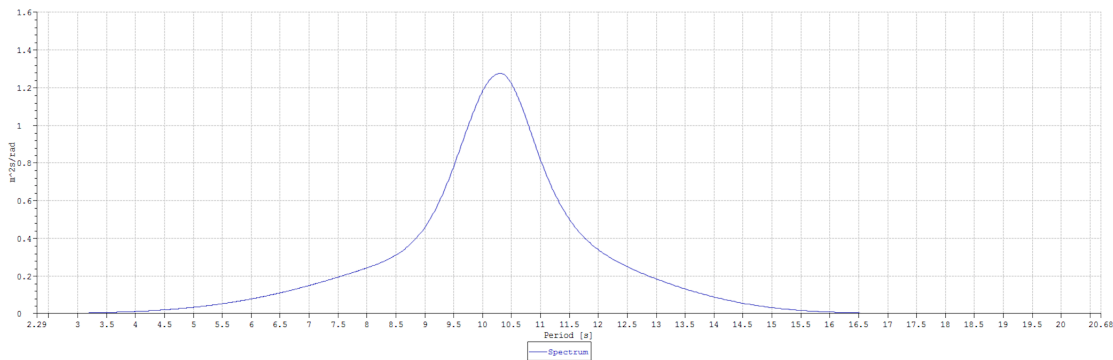


Figure 5.14: JONSWAP spectrum for the wave distribution in load case OP1

Incoming waves are simulated by JONSWAP spectrum with peakness value of 3.3, as shown in Figure 5.14. The three dimensional wind fields in all load cased are generated by using NREL's Turbsim program [Jonkman \(2009\)](#) for IEC class C. However, the IEC definition of the extreme wind speed model is a bit confusing. The reference wind speed is defined as  $50\text{m/s}$  based on the wind turbine class, and the input wind speed  $40\text{m/s}$  will be ignored when "EWM50" (extreme 50-year turbulence wind) is chosen. In this case, the "NTM" (norma turbulence wind) model is also used for the load case EX.

### 5.3.2 Case Study - TLPWT Response

#### TLPWT Response in Normal Load Case

In order to assess the influence of turbulence wind in normal LC, the turbulence wind test is performed for load case OP3. Figure 5.15 shows the time realizations of the wind speed, blade pitch, generated power and TLPWT motions in OP3 based on 1h simulations. Obviously, turbulent wind leads to blade controller pitching blades accordingly. Consequently, there is some kind of oscillations in the TLPWT motions. The maximum surge motion is about 6m, less than 5% water depth, which still fulfills the TLPWT design criteria in Section 3.1.1. The heave and pitch motions are negligible. However, the power output is always constant at rated power because the DTU 10MW wind turbine employs a constant-power controller.

The time realizations of the TLPWT performance for load case OP1 and OP2 are given in Appendix F.

#### TLPWT Response in Extreme Load Case

To assess the influence of turbulence wind in extreme LC, the turbulence wind test is performed for load case EX. Figure 5.16 shows the time realizations of the wind speed, blade pitch, generated power and TLPWT motions in EX based on 1h simulations.

In extreme conditions, the wind turbine is parked, hence there is no power output in this case. Although the TLPWT motions are larger than that in OP3, the motions are still limited. The mean surge motion is about 4m but the maximum surge motion can be 15m. The heave as well as pitch motions are still quite small.

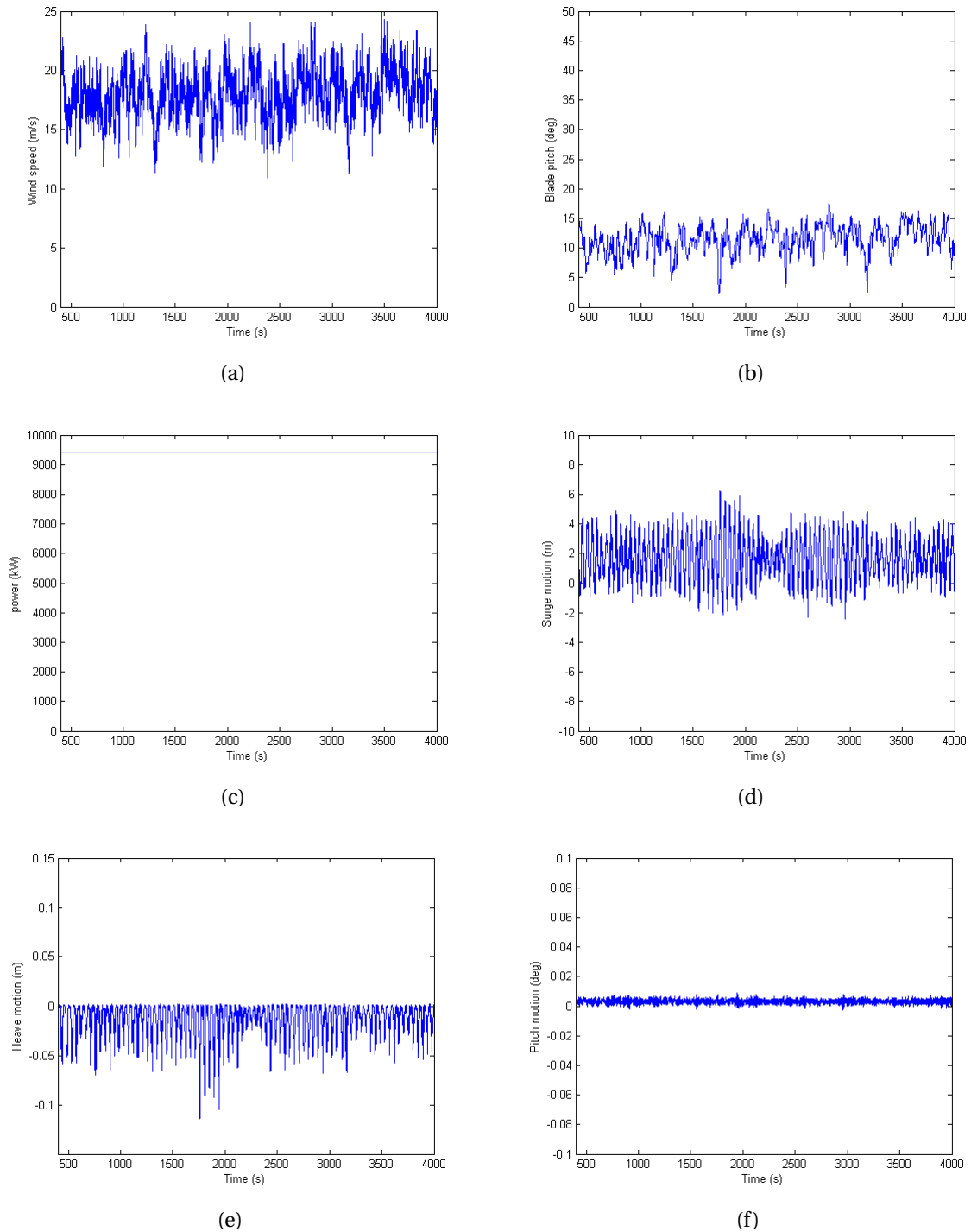


Figure 5.15: Time realizations of wind speed, blade pitch, generated power, surge motion, heave motion and pitch motion of the TLPWT for turbulence wind test in load case OP3

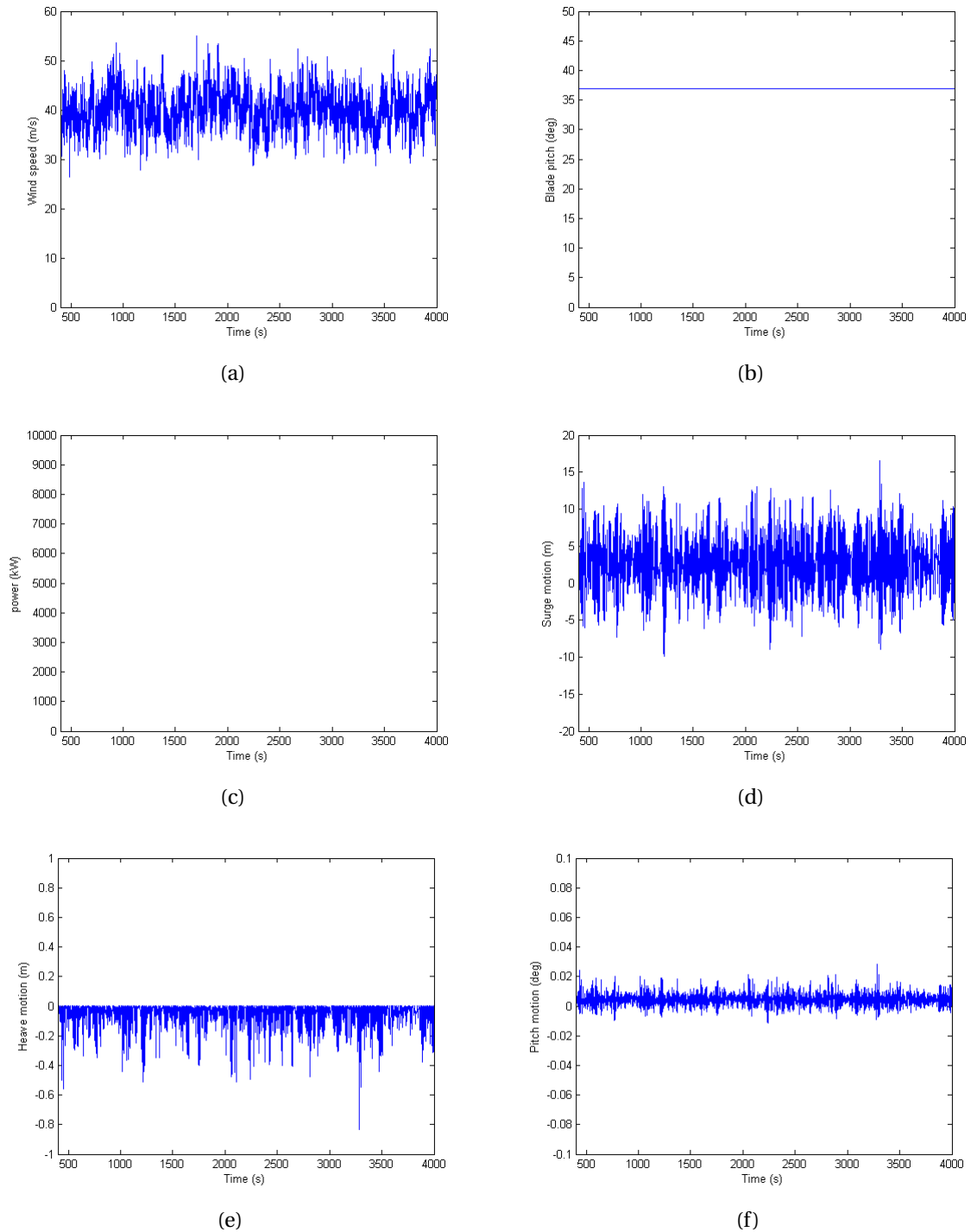


Figure 5.16: Time realizations of wind speed, blade pitch, generated power, surge motion, heave motion and pitch motion of the TLPWT for turbulence wind test in load case EX

### 5.3.3 Spectral Analysis of Response

In order to examine the influence of the turbulent wind in different load cases further, the TLPWT motion, blade and tower banding moment and tension spectra are computed by FFT method and then smoothed by WAFO toolbox. Note that the utilization of WAFO will cause energy lost in the smoothed spectrum to a certain degree, which depends on maximum lag size of the `dat2spec2` function in Matlab. The maximum lag size used in this project is 3000.

#### TLPWT Response

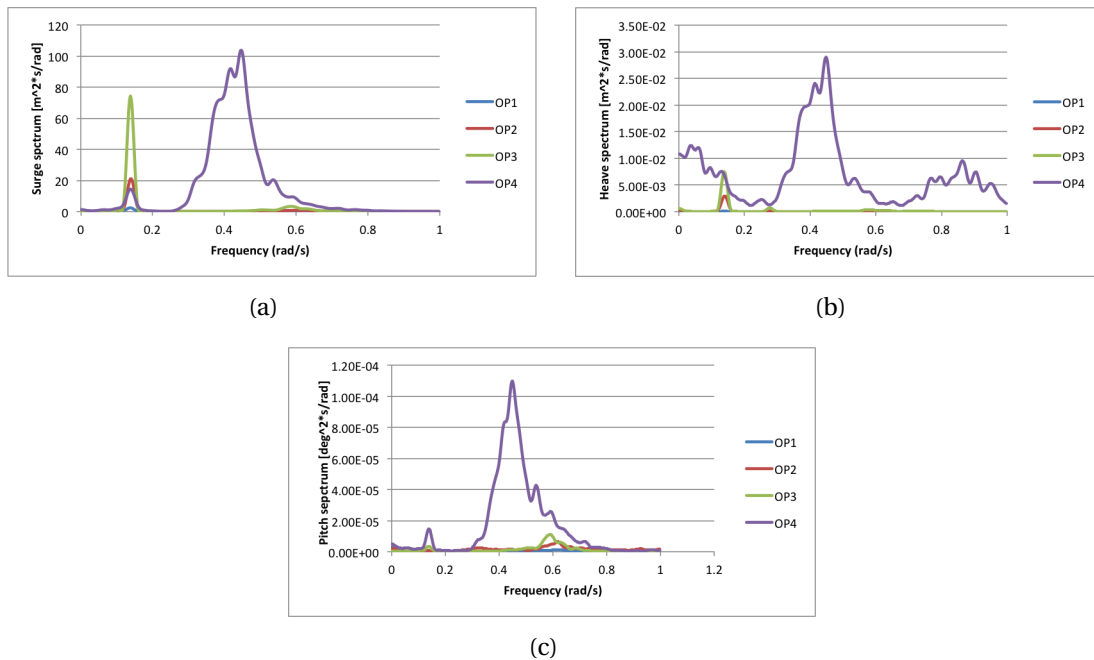


Figure 5.17: Smoothed spectra of the TLPWT responses in load case OP1, OP2, OP3 and EX

Figure 5.17 shows TLPWT response spectrum in surge, heave and pitch for normal load cases (OP1, OP2, OP3) and extreme load case (EX). Apparently, a harsher environmental conditions result in larger TLPWT responses. Furthermore, the natural frequency of the wind is about  $0.14 \text{ rad/s}$ , and the natural frequency of the incoming waves is about  $0.6 \text{ rad/s}$  for OP1, OP2 and OP3 but  $0.4 \text{ rad/s}$  for EX (calculated from the wave peak periods in Table 5.4). Checking the peaks in TLPWT response spectrum, it can be found that in operational condition, the TLPWT are dominated by turbulent wind and surge resonant responses in surge and heave motion, but

incoming wave in pitch motion. Nevertheless, all the motions are dominated by incoming waves under extreme load case as the blades are feathered in this condition.

### Blade and Tower Response

Figure 5.18(a) shows the spectra of the out-of-plane blade root bending moment under different load cases. In normal operational conditions (OP1-OP3), the blade root bending moment is increasing along with the increase of wind speed. In OP3, the bending moment spectrum has a sharp increase at  $1 \text{ rad/s}$ , which equals to the blade rotational frequency, namely '1P frequency effect'. In extreme condition (EX), the wind turbine will be parked so that the influence of blade root bending moment becomes negligible.

The fore-aft tower base bending moment depends on the nacelle motions relative to platform, thrust force and the load transfer to hull inertia and tendon tensions Bachynski (2014). Figure 5.18(b) shows the spectra of the fore-aft tower base bending moment under different load cases. It is clear that wave-frequency loading also dominates tower base bending moment, similar to TLPWT pitch motion (Figure 5.17(c)). Therefore the dynamic inertial loads is of importance for avoid big tower-base bending moment.

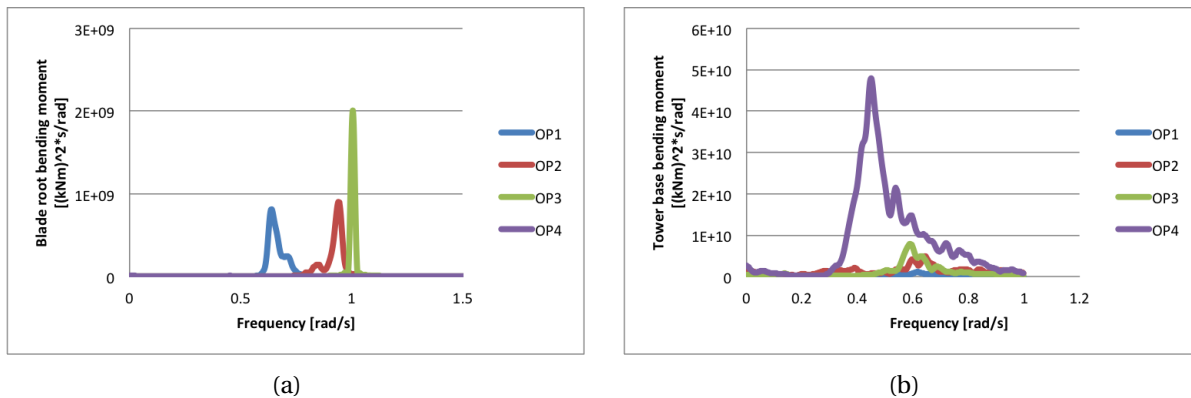


Figure 5.18: Smoothed spectra of the blade and tower bending moment in load case OP1, OP2, OP3 and EX



## Tensions

Figure 5.19 shows the tension1 spectrum. Obviously, tension1 is also dominated by the incoming wave frequency. Besides, tensions trend to increase in harsher environmental conditions. This is seen in Figure 5.26.

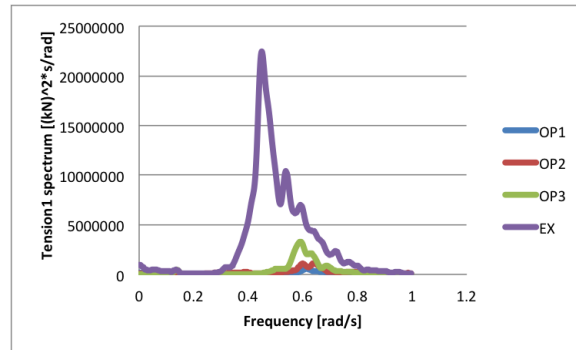


Figure 5.19: Smoothed tendon1 tension spectrum in load case OP1, OP2, OP3 and EX

### 5.3.4 Statistical Analysis of Response

Each load case in Table 5.4 is applied to 10 identical and independent 1h simulations with 5 different random seeds to reduce the stochastic variations. Then statistical analysis is performed to the average of the computed results, regarding to TLPWT global motions, blade and tower bending moment and tendon tensions.

#### TLPWT response

Figure 5.20 presents the TLPWT surge motion along wind speed. The mean surge motion keeps constant at about 2m when wind speed is larger than the rated speed 11.4m/s. But the maximum surge keeps increasing as wind speed. Indeed, large horizontal translation is not critical for the wind turbine performance or fatigue, but maybe critical for the tendon seabed connectors and the power cable due to large induced angles, and it can induce considerable tension variations due to set-down effects [Bachynski \(2014\)](#). The maximum allowable surge motion for the TLPWT is 10m, 5% of the water depth (Section 3.1.1). However, this TLPWT may experience surge motion up to 16m in 50-year extreme environment condition. Therefore the tensions in

extreme conditions are checked by ULS in this Section 5.3.5.

Figure 5.21 shows that the pitch and motion of the TLPWT are very small. Even the maximum pitch motion in EX is only 0.03deg. Therefore the pitch motion of the TLPWT can be ignored. Similar condition occurs in heave motion (see Figure 5.22). Since the TLPWT trends to move downwards due to its tendon effects, as shown in Figure 5.15(e) and Figure 5.16(e), the minimum heave value is studied instead of the maxima. As expected, the TLPWT also keeps stable in vertical direction in operational condition, but may experience relatively large heave up to 0.8m in extreme condition.

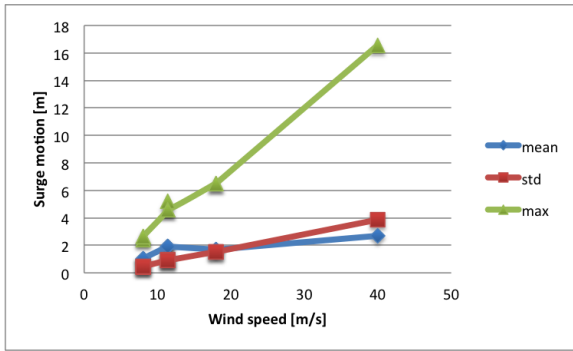


Figure 5.20: TLPWT surge motion

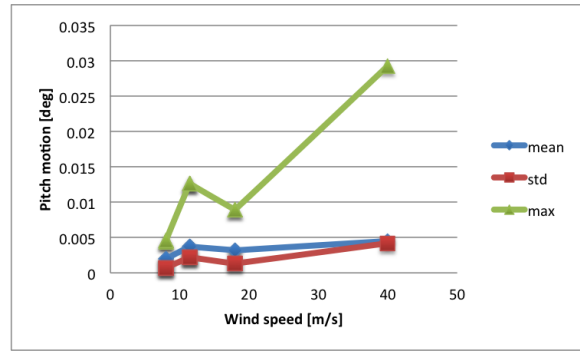


Figure 5.21: TLPWT pitch motion

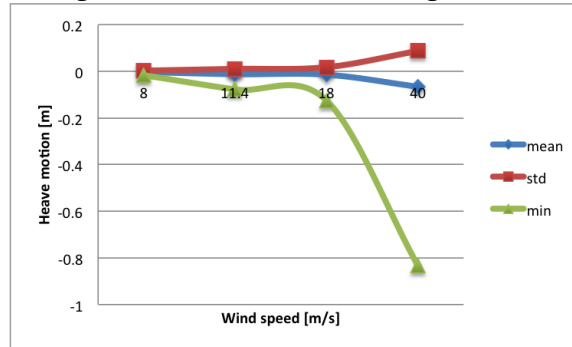


Figure 5.22: TLPWT heave motion

### Blade and Tower Response

The TLPWT is subjected to head wind, implying that the fore-aft tower base bending moment, i.e. the bending moment along y-axis ( $M_y$ ) should be the largest tower base bending moment. Therefore this section only discusses the fore-aft tower base bending moment. Figure 5.23

shows the tower base fore-aft bending moment against wind speed. The mean value, standard derivation and maximum value of the tower base bending moments all approaches peaks at rated speed  $11.4\text{m/s}$  due to the turbine control system.

Figure 5.24 shows the blade root out-of-plane bending moment. Note that the blade root bending moment is negative in operational condition but positive in extreme condition, so that the minimum value is examined in OP1-OP3, but maximum value in EX. It seems that the control system helps to limit the blade root bending moment generally. However, in extreme condition, the control system is shut up and there will be significant bending moment at blade root.

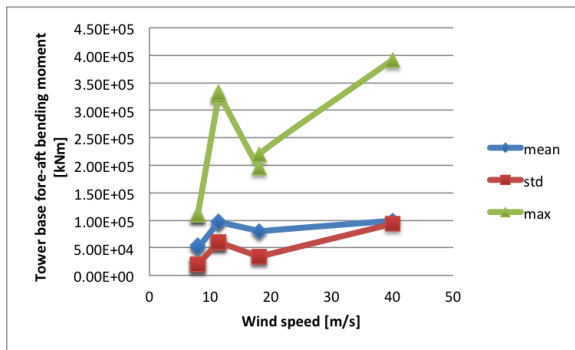


Figure 5.23: Tower base bending moment

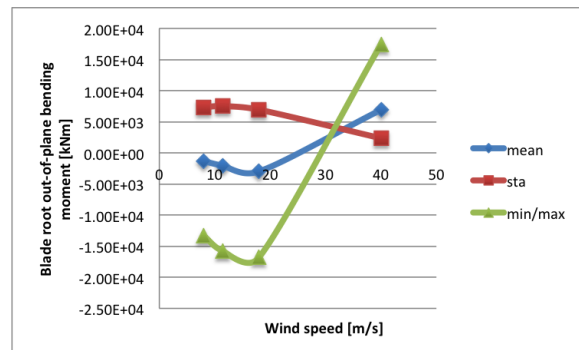


Figure 5.24: Blade root bending moment

In extreme environmental conditions, the wind turbine will be parked which eliminates the the effects of external harsh environments on the offshore wind turbine to a large degree. However, it is still possible to experience large tower base or blade root bending moment.

## Tensions

The realizations of duration  $1h$  tendon tensions are shown in Figure 5.25. The tendon mooring system of the TLPWT consists of three tendons. The fore tendon tension1/2 is the largest and aft tendon tension 3 is the smallest axial forces acting on the tendons when wind and wave comes from head sea (See Figure 5.1). For the safety of the TLPWT, tension1/2 should not exceed the yield tension force, while tension 3 should be positive.

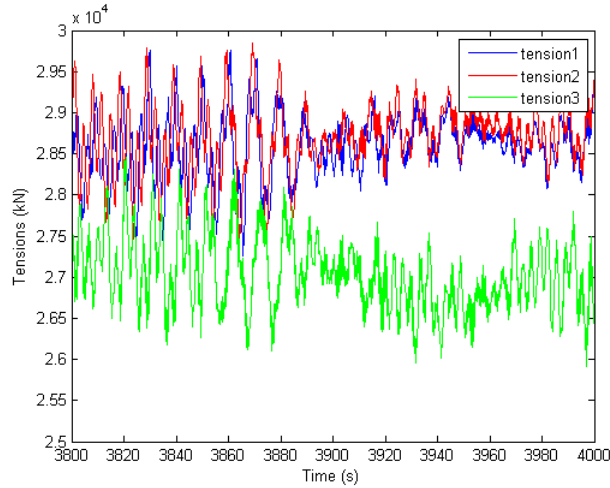


Figure 5.25: Time history of the tendon axial forces for the TLPWT in OP1

Figure 5.26 shows the tension1 statistical results against wind speed. The derivation values are almost zero, implying there is less variation in tendon1 tension due to small global motions of the TLPWT. Also because of the small global motion, the mean value of tension1 changes rarely in different wind speed. The maximum tension force in 50-year extreme environmental condition is  $3.824 \times 10^4$ , less than the yield load calculated from Eq. 5.4. Different from tension1, the minimum value of tension3 should be pay more attention to avoid slacking. As seen from Figure 5.27, the minimum tension3 keeps a high value even in extreme conditions, which implies a safe structure design. The mean value of both tension1 and tension3 are close to pre-tension  $28064kN$ , which implies that the global motions of the TLPWT are really small. The variations for tensions of the TLPWT are not sensitive to wind speed except in extreme conditions. ULS is used to check tensions further in Section 5.3.5.

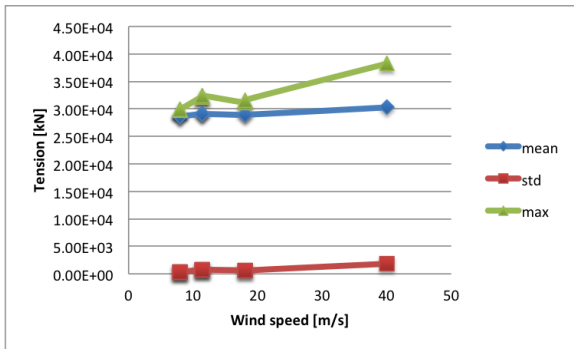


Figure 5.26: Tension1

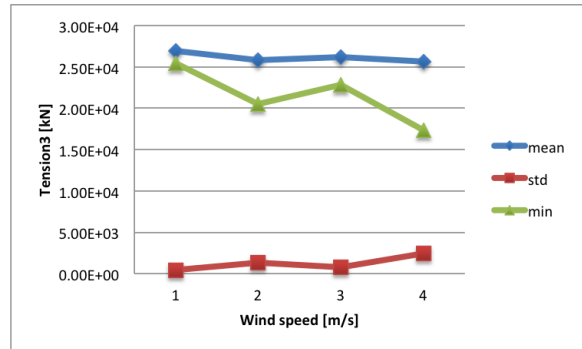


Figure 5.27: Tension3

### 5.3.5 ULS Check for Tensions

As mentioned in last section, tension1 has the possibility of exceeding the yield tendon axial force, while tension3 has the possibility of slacking. Hence ULS check is performed in this step in terms of tension1 and tension3.

#### Tension1/2

The maximum tension1 is checked further by following ULS requirement [Veritas \(2008\)](#). Firstly, 20 realizations of 1h are simulated. Secondly, one should establish extreme tension samples as maximum tension from each simulation. Thirdly, Gumbel cumulative distribution function (CDF) is used to fit the occurrence probability of observed samples, like shown in Figure 5.28. Finally, the corresponding Gumbel probability density function (PDF) can be calculated. The required extreme tension value shall be estimated as the Most Possible Maxima (MPM) value of the extreme value distribution, i.e. the peak  $T_{MPM} = 37619kN$  in Figure 5.29.

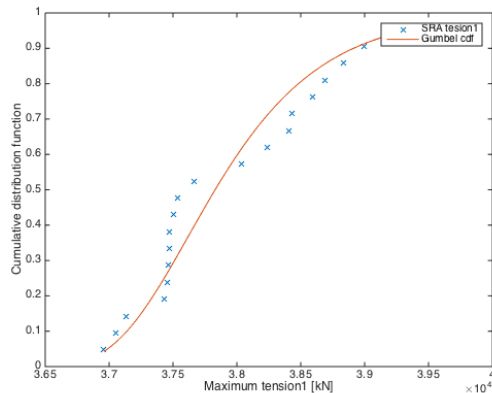


Figure 5.28: Maximum tension cdf

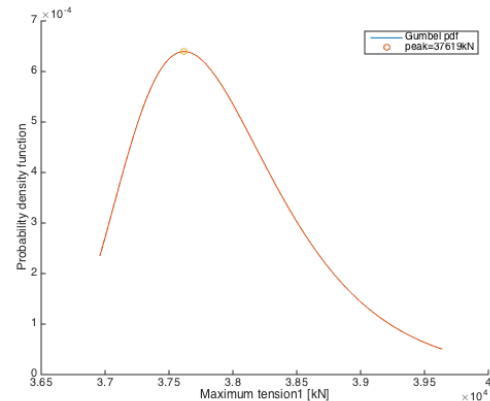


Figure 5.29: Maximum tension pdf

The variation of tensions is also examined in the turbulence wind test. Assuming tendon yield stress  $\sigma_y = 250MPa$ , the axial yield load on tendons are:

$$F_t = \sigma_y A_t = 250 \times 10^3 \times 0.73083 = 1.83 \times 10^5 kN \quad (5.4)$$

Then mooring line design for ULS is governed by the utilization factor:

$$u = \frac{T_{mean}\gamma_{mean} + T_{dyn}\gamma_{dyn}}{S_C} \leq 1 \quad (5.5)$$

Where,  $T_{mean}$  is the average value of 20 observed tension1;  $T_{dyn}$  is the difference between mean tension and most probable maxima, i.e.  $T_{dyn} = T_{MPM} - T_{mean}$ ;  $\gamma_{mean}$  and  $\gamma_{dyn}$  are partial safety factors with  $\gamma_{mean} = 1.1$ ,  $\gamma_{dyn} = 1.5$  and  $S_C$  is the characteristic strength which equals to 0.95 times of  $F_t$ .

The calculated utilization factor for tension1 is 0.24, which is much less than 1. This means that the strength of the tendon1 is definitely sufficient. However, this kind small utilization factor also means a too stiff tendon design and consequently more costly on the other hand. Further optimization for the tendon system can be performed in future work.

### Tension3

Moreover, ULS can also be used to check tension3 to avoid slacking phenomenon (Section 3.1.4) by Eq. 3.6:

$$\gamma_0 S_0 - \gamma_E S_E = 1.2 \times 28064 - 0.7 \times 26136 = 13982 > 0 \quad (5.6)$$

Where  $S_0$  is axial pretension force;  $S_E$  is the mean tension3 and  $\gamma_0$  as well as  $\gamma_E$  are safety factors. For the tendons of a TLP structure,  $\gamma_0 = 1.2$  and  $\gamma_E = 0.7$ . It can be seen that tension3 has no potential of slacking.

# Chapter 6

## Comparison of TLP, Spar and Semi-submersible Wind Turbines

This project only focuses on the design of the TLP floater. But a semi and a spar concepts are studied in the meantime of this work. All three floater concepts considered are designed to support the same DTU 10MW reference wind turbine, as shown in Figure 1.4. Table 6.1 lists the properties of the three floater concepts. The displacement of the Semi and Spar wind turbine equal to their mass. On the contrary, the displacement of the TLPWT is approximately twice than its mass due to tendon pretension. In addition, both Semi and Spar utilize catenary mooring lines but TLP utilizes tension legs. Section 1.2 has already introduces the three offshore wind turbine concepts in details. The frequency-domain as well as time-domain analysis are performed for all the three concepts within the same load cases. The characteristics of the three concepts are compared in this chapter.

Table 6.1: Properties of the three floater concepts

Floater	TLP	Semi	Spar
Water depth [m]	200	320	320
Draft [m]	35.3	19.15	120
Waterline diameter [m]	19.8	12.8	12
Total mass [t]	9293	7520	13405
Displacement [m <sup>3</sup> ]	17362	7520	13078
COG [m]	(-0.04,0,-9.83)	(0,0,4.9)	(-0.3,0,-74.53)
COB [m]	(0, 0,-22.67)	(0,0,-9.576)	(0,0,-62.07)
Mooring configuration	3 Tendon lines	3 Catenary lines	3 Catenary lines

## 6.1 Natural Period

Table 6.2 represents the natural periods of the three concepts obtained by free decay tests in calm water. Firstly, the semi and especially spar have relatively larger natural periods than the TLP floater in surge/sway. This is because semi and spar employ catenary mooring systems which has quite small restoring stiffness compared with tendon mooring system. The TLPWT is soft in horizontal directions but stiff in vertical direction. Nevertheless, SemiWT and SparWT are soft in both horizontal and vertical directions. Secondly, the TLP floater has extremely small natural periods in heave and pitch than others also due to its stiffed tendon mooring system. In addition to the TLPWT, the tower bending plays an vital role in its pitch motion, which has been discussed in Section 5.1. Last but not least, all the natural periods are outside of the general wave periods (3 – 25s) except for TLP’s yaw natural period, semi’s heave natural period and spar’s yaw natural period. This indicates that these offshore wind turbines maybe experience significant excitations in relative motion modes.

Table 6.2: Undamped natural periods of the three WT concepts obtained by decay test

Floater	TLP	Semi	Spar
Surge/Sway [s]	45.23	62.60	139.60
Heave [s]	0.55	21.93	31.00
Pitch [s]	0.60	41.11	35.40
Yaw [s]	20.87	51.87	9.70

## 6.2 Platform Motion

Because of the differences of the three concepts in terms of mooring system and structural as well as hydrodynamic properties, these three concepts experience totally different global motions in normal operational conditions. Figure 6.1 and Figure 6.2 show the mean surge and pitch motions of the three offshore wind turbines in various constant wind. Apparently, the mean values of global motions increase along with wind speed until the rated wind speed  $11.4\text{ m/s}$ , and then decrease since the wind turbine controller starts to pitch blades from that point. As a result of tensioned mooring system, a small surge motion (about  $3\text{ m}$ ) and almost zero heave motion can be detected for the TLPWT concept. On the other hand, the SparWT presents large surge



motion (up to 26m) while SemiWT presents large pitch motion (up to 10deg).

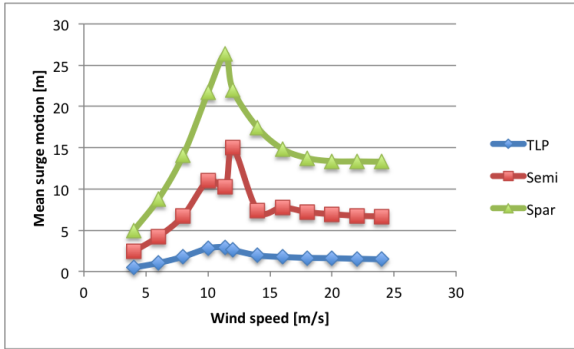


Figure 6.1: Mean surge motion

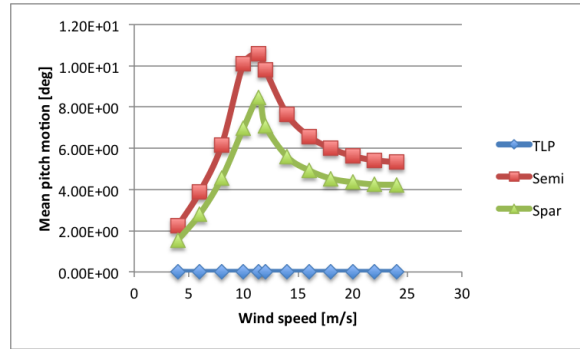


Figure 6.2: Mean pitch motion

Furthermore, Figure 6.3 and Figure 6.4 compare the mean values, standard derivations and maximum of surge and pitch motions of the three concepts in the four load cases (given in Table 5.4). In general, the motions of the three platforms increase first, then decrease after 11.4m/s, and finally increase again as wind speed higher than maximum allowable speed 18m/s. This is due to the reaction of PRVS control system to the environmental conditions, which is already introduced in Section 5.2. As a result of the taut mooring system, the motions of the TLPWT are significantly smaller than the other two concepts, especially the pitch motion. Table 6.1 shows that the COG of the SparWT is 74.53m lower than water surface, much deeper than the others. This explains why the mean, derivation and maximum of the surge motion of the SparWT are larger than that of TLPWT and SemiWT. The SparWT may experience surge motion up to 25m even in normal wind speed. In addition, one should note that SemiWT has a quite large pitch motion compared to others. The pitch motion of the SemiWT can reach 16° at wind speed 11.4m/s.

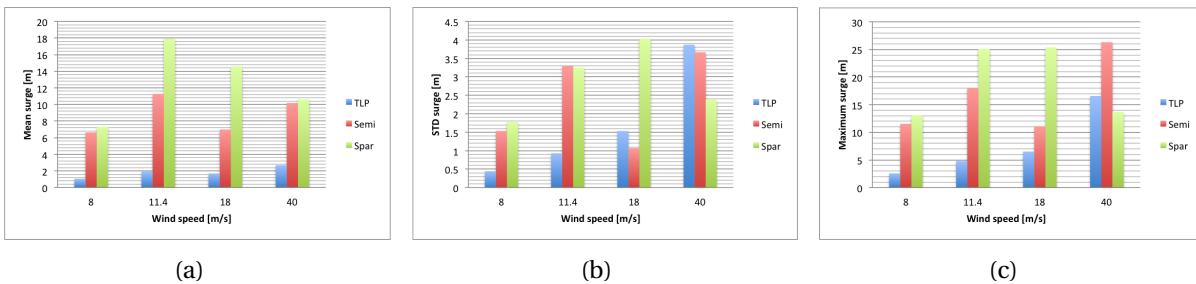


Figure 6.3: Mean values, standard derivations and maximum values of the surge motion for the three concepts

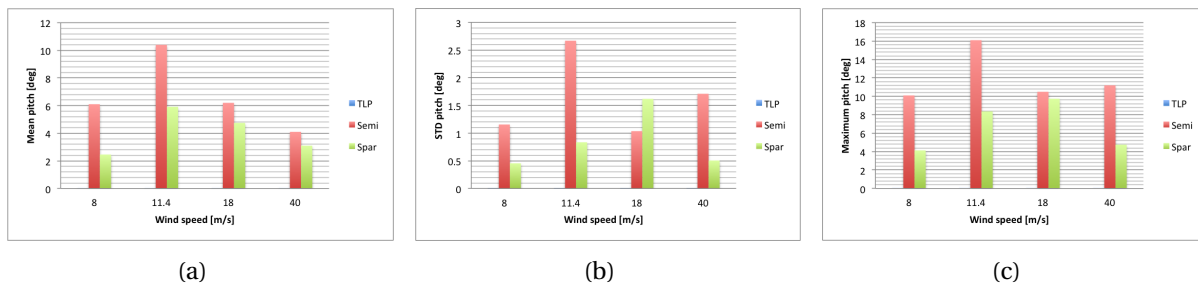


Figure 6.4: Mean values, standard derivations and maximum values of the pitch motion for the three concepts

### 6.3 Tower Base Bending Moment

It is mainly the large thrust force acting on the rotor and the weight of the rotor itself that causes tower base bending moment due to the tower tilt [Cheng et al. \(2015\)](#). Even under the same load case, the three offshore wind turbine concepts demonstrate significant differences in global motions, leading to great discrepancies in the tower base bending moment. The variations of tower base bending moment may result in outstanding stress fluctuations, and thus great fatigue damage.

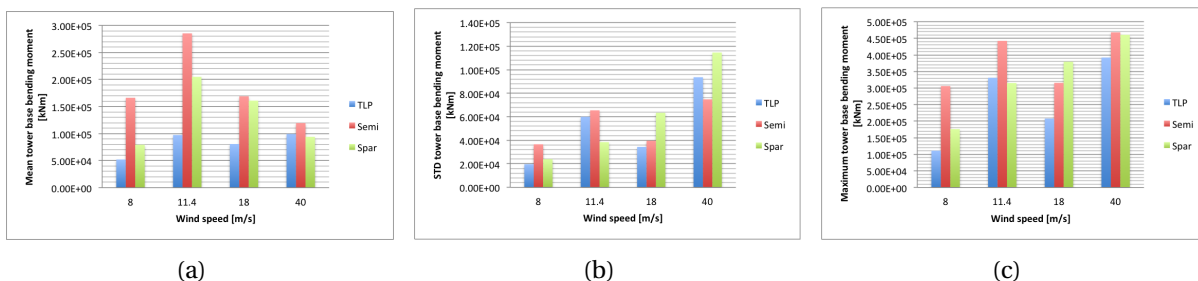


Figure 6.5: Mean values, standard derivations and maximum values of the fore-aft tower base bending moment for the three concepts

Figure 6.5 compares statistical results of the tower base bending moment for the three concepts in different wind speed. Here only the fore-aft tower base bending moment is considered. Similar to global motions, the tower base bending moment increases before rated wind speed, then decreases until cut-out wind speed and finally increases again in extreme wind speed. The mean bending moment of SemiWT is the largest, but that of the TLPWT is the smallest. The maximum bending moment shows the same trend. Note that the three concepts all show very close and large derivations for the tower base bending moment. Hence it is strongly recom-

mended to check the fatigue damage caused by tower base bending moment in the future work.

## 6.4 Blade Root Bending Moment

The general out-of-plane blade root bending moment also shows the same trend as global motions and tower base bending moment, increasing before rated speed  $11.4\text{ m/s}$ , decreasing afterwards and finally increasing again after  $24\text{ m/s}$  (See Figure 6.6). Apparently, the TLPWT has the smallest blade root bending moment but with largest variations, except in extreme condition. The mean value, standard derivations and maximum valued of the blade root bending moment of SemiWT and SparWT are very close. Considering the high variations of the blade root bending moment of the three designs, it is also recommended to check the fatigue damage caused by blade root bending moment.

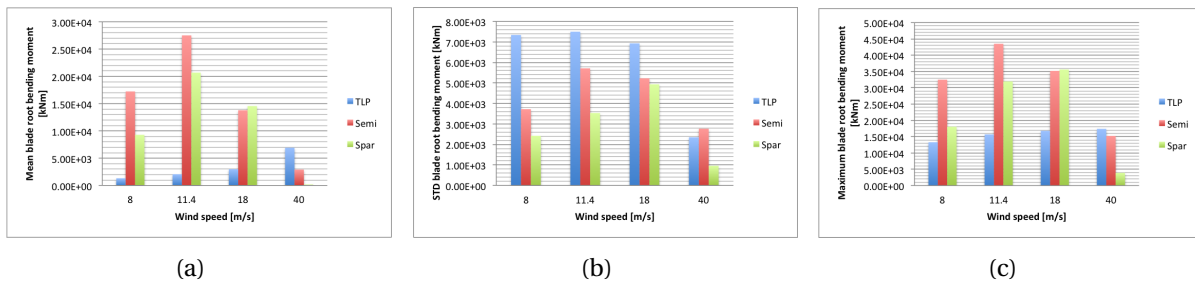


Figure 6.6: Mean values, standard derivations and maximum values of the out-of-plane blade root bending moment for the three concepts

## 6.5 Mooring Line Tension

Both SemiWT and SparWT employ three catenary mooring lines, while TLPWT employs three pretension tendons (See Figure 1.4). Therefore, the tensions acting on mooring lines of the TLPWT are significantly larger than SemiWT and SparWT. The mean tensions of the TLPWT in different wind speed are all close to pretension  $28064\text{ kN}$  due to TLPWT's small global motions, which is discussed in Section 6.2. Even though the derivations of tendon tensions are small in normal operation condition, the TLPWT may experience slightly larger tension  $38200\text{ kN}$  in 50-

year extreme condition with the very obvious derivation  $1840kN$ . This maximum tension has a good agreement with tension value under maximum thrust (Section 4.1).

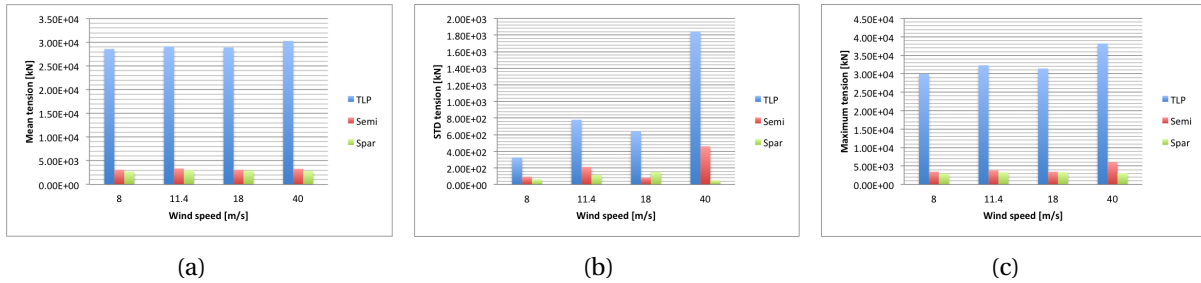


Figure 6.7: Mean values, standard derivations and maximum values of the mooring line tensions for the three concepts

# Chapter 7

## Summary and Recommendations for Further Work

### 7.1 Summary and Conclusions

The application of big-size wind turbine is constrained to land-base and shallow water nowadays. It is still challenging to build big-size offshore wind turbines in deep water. But challenge means opportunity. This thesis aims to examine a state-of-art TLP floater initial design for supporting the 10MW DTU reference wind turbine. The TLP floater consists of one single column, three spokes and three pretension tendons. In the mean time of the this project, parallel works (Semi and Spar floaters) are designed. The obtained properties of these three concepts are compared.

Fundamentally different from other offshore structures, the TLPWT employs a tension mooring system instead of a catenary mooring system. The pretension per line is  $28064kN$  and the yield tendon axial force is  $1.8 \times 10^5 kN$ . Due to the stiffed tendons, the TLPWT has small response motions. Therefore, the tendon tensions are almost constant even in 50-year extreme conditions. Additionally, the maximum tension<sup>1</sup> and minimum tension<sup>3</sup> are examined by ULS, which results show that the TLPWT tendons have no possibility of slacking or exceeding yield tension. On the other hand, the response motions of the SemiWT and SparWT are relatively larger. The SparWT can experience maximum surge motion up to  $25m$  and SemiWT can expe-

rience maximum pitch motion  $16^\circ$  at wind speed  $11.4\text{m/s}$ .

The hydrodynamic behaviors of the TLPWT are assessed in details by performing a wave-only frequency-domain analysis in head sea. The added mass and damping coefficients present strong wave-frequency dependence. The viscous damping effect is of importance in the surge motion of the TLPWT in long waves. In order to compute correct second-order results within the element number limit, a mesh convergence study is performed regarding to the mesh size and radius of the second-order free surface model. Mesh case 3 is selected after a series of comparisons. As the second-order forces are small, their most important contribution is in the vicinity of resonance. For instance, the resonance of heave QTF coincides with the pitch/bending natural frequency.

The natural periods of the TLPWT are  $45.23\text{s}$ ,  $0.55\text{s}$ ,  $0.60\text{s}$  and  $20.87\text{s}$  in surge/sway, heave, pitch/roll and yaw respectively. It is very soft in horizontal motions, but quite stiff in vertical motions due to stiffed tendon mooring system. On the contrary, the SemiWT and SparWT concept are soft in both horizontal and vertical planes. Furthermore, it should be noted that the flexibility of the tower has a significant contribution to the TLPWT pitch motion. The tower bending natural period is  $3.49\text{s}$ .

The rated wind speed for the three concepts is  $11.4\text{m/s}$ . The wind turbine controller plays an vital role during operation process to maximize the energy capture, and minimize the external loads and thus response motions. In critical weather conditions, the controller can pitch, feather or even shutdown the turbine. Consequently, the platform motions become less, but the rotor speed, generated torque and produced power still keep constant.

The TLPWT experiences wave frequency motions of the same order of magnitude as those of SemiWT and SparWT in horizontal plane. In the vertical plane, however, the TLPWT behaves like a fixed structure. In addition, the heave motion and pitch motion of the TLPWT are kinematically coupled with its surge motion. Usually the low-frequency TLPWT motions are primarily excited by wind, while its pitch motion, blade root bending moment, tower base bending mo-

ment and tensions are excited by incoming wave frequency. Nevertheless, in harsh weather, the turbine is shutdown and all the performances of the TLPWT are therefore dominated by wave frequency.

In summary, the global performance behavior of the TLPWT is desirable for a structure this size. The tension-leg mooring system suppresses nearly all vertical motions. The horizontal motion is quite small even in extreme weather conditions and thus there is rare change representing in tensions. Furthermore, the tower base and blade root bending moment are also much smaller than the Semi and Spar wind turbine. This TLPWT concept features with wide weather window, great load capacity and high stability. It is definitely reliable for the application of off-shore wind turbines in deep water.

Table 7.1 provides a summary of the properties of the TLPWT.

Table 7.1: Summary of TLPWT properties

Water depth	200m
Draft	35.3m
Rated power	10MW
Hub height	119m
Central column diameter	19.8m
Spoke height	8.5m
Spoke width	8.5m
Tendon outer radius	1.35m
Tendon inner radius	1.26m
Tendon mass per length	5737kg/m
Pretension per line	28064kN
Total mass	9293t
Displacement	17362m <sup>3</sup>
COG	(-0.04m, 0, -9.83m)
COB	(0, 0, -22.67m)
Surge/sway natural period	45.23s
Heave natural period	0.55s
Pitch/roll natural period	0.60s
Tower bending pitch natural period	3.49s
Yaw natural period	20.87s

## 7.2 Recommendations for Further Work

This thesis is a preliminary design and will serve as basis for further development of the TLPWT concept. The following suggestions are recommended for the future work.

Considering the TLPWT's small response motions and heave natural period, it can be concluded that the tendon mooring system is too stiff. This implies a great CAPEX on tendon material from economical perspective. The diameter of the tendons should be adjusted and so as the displacement of the TLPWT.

One tendon per corner is an economical option. However, there is no redundancy with one tendon per corner, and tendon removal or replacement involves complete de-installation/installation of the TLP. With one tendon per corner, safety factors are increased to provide additional safety that is normally provided by redundancy. Therefore, it is suggested to install more tendons in the TLPWT.

Additionally, only ULS is used for the inspection of the TLPWT design. ALS and FLS should be used in the future work.

Except for 'Springing' effects, the Tension-leg platforms are also known due to the 'Ringing' effects, which is a high frequency transient response. Steep and asymmetric waves have been shown to give ringing response. The ringing behavior is typically observed in sea states with peak period 3-5 times the natural periods. This project only studies the 'Springing' effects caused by sum-frequency. The 'Ringing' effects are also recommended to investigate in the further work.

This project only checked the viscous damping effects in frequency-domain analysis. Alternatively, the viscous damping can be checked by using viscous elements with difference drag coefficient  $C_D$  when running SRA. The  $C_D$  on the tendons are defined in the cross sections in the `inpmo.inp` file, while  $C_D$  on the hull are defined in the `sys` file (either as global drag coeffi-



icients for the whole hull or as distributed element forces).

In this project, Newman's approximation is used to calculation the difference-frequency QTF in SRA. Because the surge natural period is higher than general wave period, this approximation can give a satisfactory results for the slow-drift motions in horizontal plane. However, this approximation underestimates the vertical slow-drift forces. In this case, it is required to apply a full quadratic transfer function matrix for the slow-drift force computation in the vertical plane.

All the three concepts all show significant variations in fore-aft tower base bending moment as well as out-of-plane blade root bending moment. These variations may result in outstanding stress fluctuations, and hence great fatigue damage. Hence, it is strongly recommended to assess the fatigue damage in long term caused by these moments.

# Appendix A

## Acronyms

**ALS** Accident Limit State

**BEM** Blade Element/Momentum

**CAPEX** Capital Expenditure

**COB** Center Of Buoyancy

**COG** Center Of Gravity

**CDF** Cumulative Distribution Function

**DDF** Deep Draught Floater

**DLL** Dynamic Link Library

**DOF** Degrees Of Freedom

**EU** European Union

**EWEA** European Wind Energy Associate

**FLS** Fatigue Limit State

**GDW** Generalized Dynamic Wake

**FFT** Fast Fourier Transform

**FVAWT** Floating Vertical Axis Wind Turbine

**HF** High Frequency

**KC** Keulegan-Carpenter

**LC** Load Case

**LF** Low Frequency

**MPM** Most Possible Maxima

**PDF** Probability Density Function

**PRVS** Pitch-Regulated Variable Speed

**QTF** Quadratic Transfer Function

**QTM** Quadratic Transfer Motion

**SemiWT** Semi-submersible Wind Turbine

**SIMO** Simulation of Marine Operation

**SparWT** Spar Wind Turbine

**SRA** SIMO-RIFLEX-AeroDyn

**TLP** Tension Leg Platform

**TLPWT** Tension Leg Platform Wind Turbine

**ULS** Ultimate Limit State

**WADAM** Wave Analysis by Diffraction and Morrison Theory

**WAFO** Wave Analysis for Fatigue and Oceanography

**WF** Wave Frequency

# Appendix B

## Specifications of the TLPWT

All the values shown in this section are based on initial spreadsheet calculation.

Table B.1: Main dimensions for central upper column

Upper central column diameter	$D_1$	19.8m
Upper central column height	$h_1$	36.8m
Upper central column thickness	$t_1$	
Steel density	$\rho$	7850kg/m <sup>3</sup>
Displacement	$V_{column1}$	8252m <sup>3</sup>
Mass	$m_{columns}$	1.78e6kg
Central of gravity	COG	(0,0,-8.4m)
Central of buoyancy	COG	(0,0,-13m)
Inertia moment about x-axial	$I_x$	4.62e8kgm <sup>2</sup>
Inertia moment about y-axial	$I_y$	4.62e8kgm <sup>2</sup>
Inertia moment about z-axial	$I_z$	1.96e8kgm <sup>2</sup>

Table B.2: Main dimensions for central lower column

Lower central column diameter	$D_2$	19.8m
Lower central column height	$h_2$	8.5m
Lower central column thickness	$t_2$	
Steel density	$\rho$	7850kg/m <sup>3</sup>
Displacement	$V_{column2}$	2617m <sup>3</sup>
Mass	$m_{columns}$	5.87e5kg
Central of gravity	COG	(0,0,-31.05m)
Central of buoyancy	COG	(0,0,-31.05m)
Inertia moment about x-axial	$I_x$	6.14e7kgm <sup>2</sup>
Inertia moment about y-axial	$I_y$	6.14e7kgm <sup>2</sup>
Inertia moment about z-axial	$I_z$	9.00e7kgm <sup>2</sup>

Table B.3: Main dimensions for pontoons

Pontoon number	$n_p$	3
Pontoon radius	$r_p$	39.6m
Cross section height	$h_p$	8.5m
Cross section weidth	$w_p$	8.5m
Steel density	$\rho$	7850kgm <sup>3</sup>
Displacement	$V_{pontoons}$	6437.48m <sup>3</sup>
Mass	$m_{pontoons}$	1.30e6kg
Central of gravity	COG	(0,0,-31.05m)
Central of buoyancy	COG	(0,0,-31.05m)
Inertia moment about x-axial	$I_x$	6.91e7kgm <sup>2</sup>
Inertia moment about y-axial	$I_y$	6.91e7kgm <sup>2</sup>
Inertia moment about z-axial	$I_z$	9.04e8kgm <sup>2</sup>

Table B.4: Main dimensions for ballast system

Diameter	$D_3$	19.8m
Height	$h_3$	5.65m
Concrete density	$\rho$	2562.5kg/m <sup>3</sup>
Displacement	$V_{ballast}$	1739m <sup>3</sup>
Mass	$m_{ballast}$	4.46e6kg
Central of gravity	COG	(0,0,-32.48m)
Central of buoyancy	COG	(0,0,-32.48m)
Inertia moment about x-axial	$I_x$	1.21e8kgm <sup>2</sup>
Inertia moment about y-axial	$I_y$	1.21e8kgm <sup>2</sup>
Inertia moment about z-axial	$I_z$	2.18e8kgm <sup>2</sup>

# Appendix C

## Overview of QTFs

Figure C.1 - Figure C.6 show the sum-frequency QTFs in heave for mesh case 1-6 respectively.

Figure C.7 - Figure C.12 show the sum-frequency QTFs in pitch for mesh case 1-6 respectively.

Figure C.13 - Figure C.18 show the difference-frequency QTFs in surge for mesh case 1-6 respectively. The red dot lines shown in the following pictures represent the diagonal lines, where

$$w_1 = w_2.$$

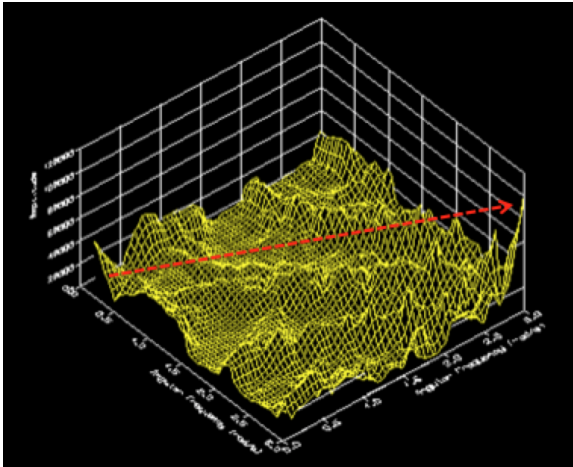


Figure C.1: Mesh 1 sum-freq. QTF in heave

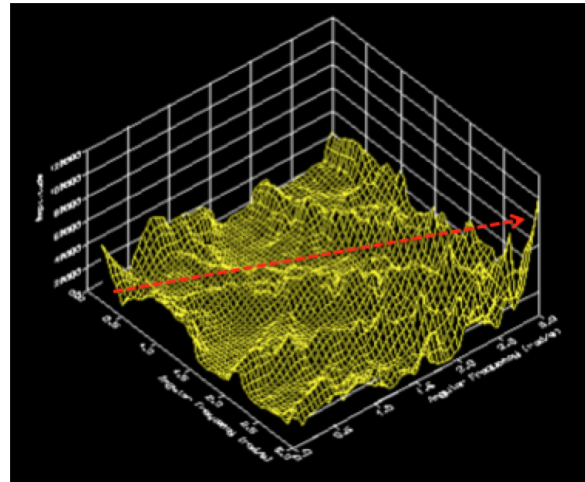


Figure C.2: Mesh 2 sum-freq. QTF in heave

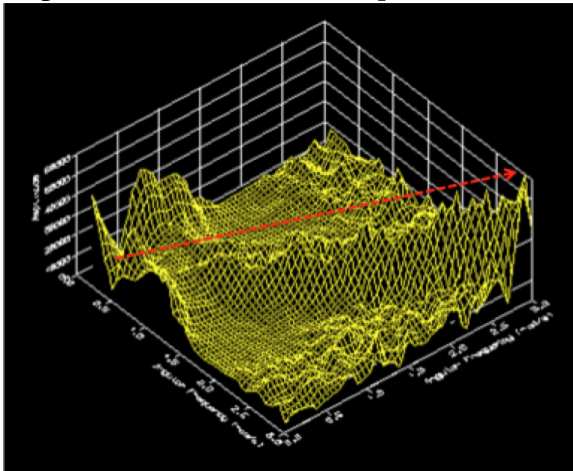


Figure C.3: Mesh 3 sum-freq. QTF in heave

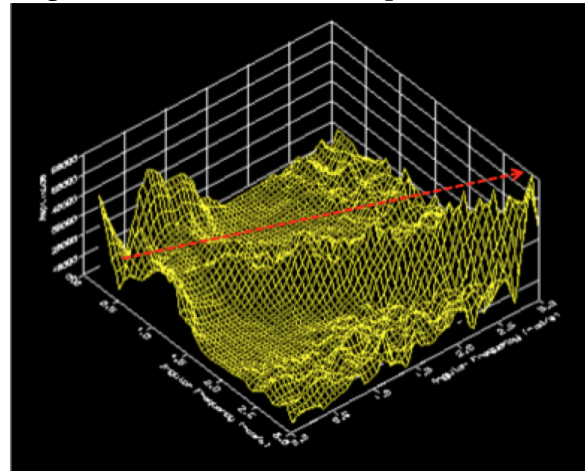


Figure C.4: Mesh 4 sum-freq. QTF in heave

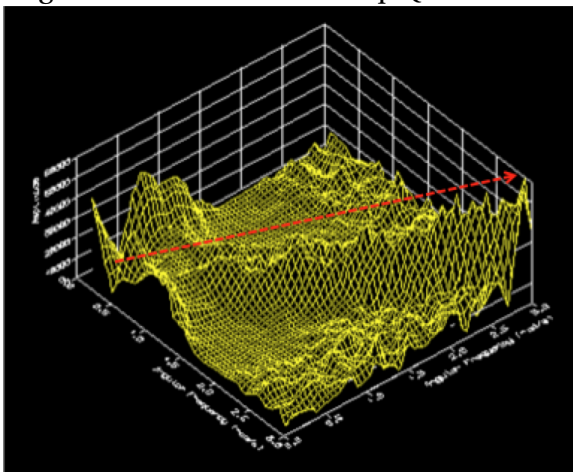


Figure C.5: Mesh 5 sum-freq. QTF in heave

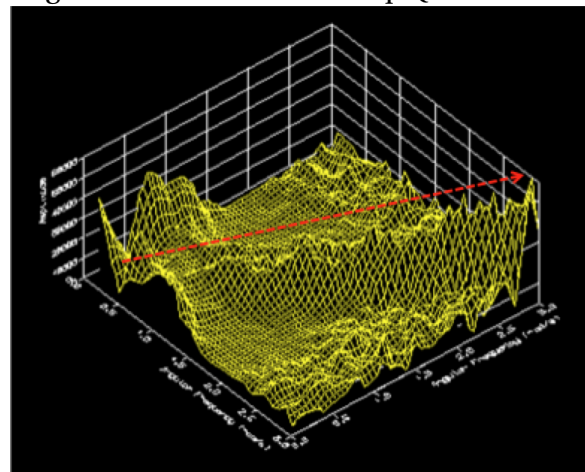


Figure C.6: Mesh 6 sum-freq. QTF in heave

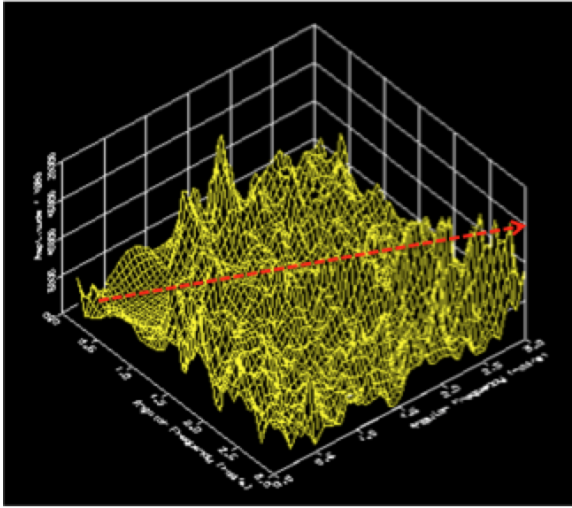


Figure C.7: Mesh 1 sum-freq. QTF in pitch

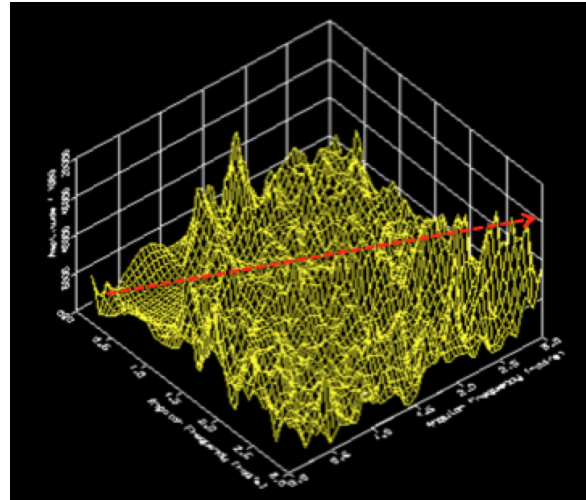


Figure C.8: Mesh 2 sum-freq. QTF in pitch

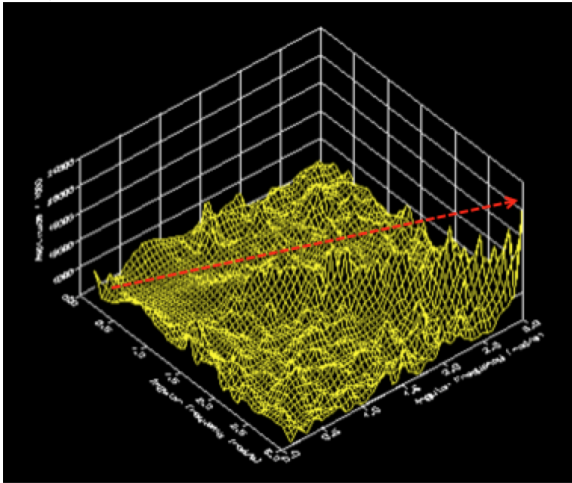


Figure C.9: Mesh 3 sum-freq. QTF in pitch

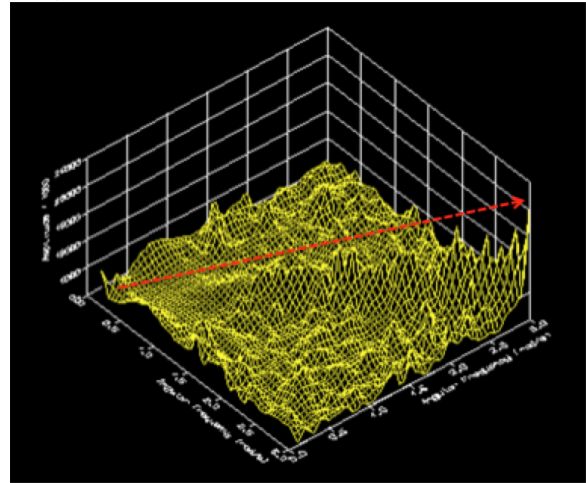


Figure C.10: Mesh 4 sum-freq. QTF in pitch

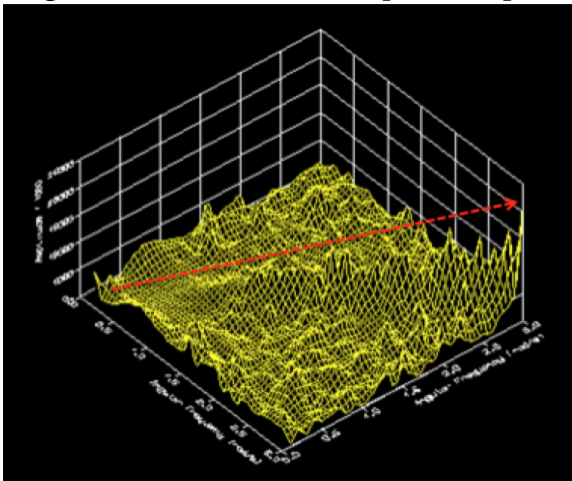


Figure C.11: Mesh 5 sum-freq. QTF in pitch

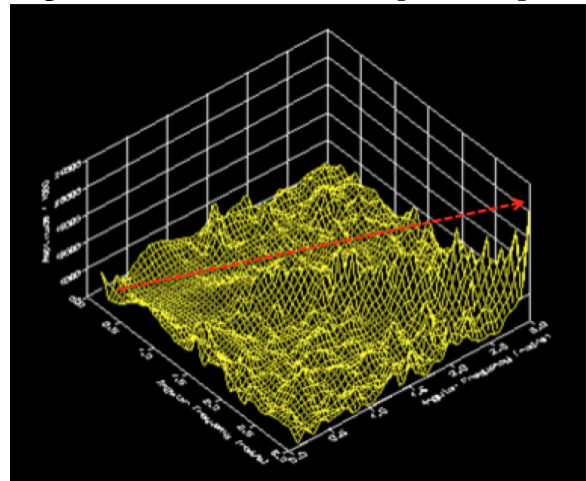


Figure C.12: Mesh 6 sum-freq. QTF in pitch



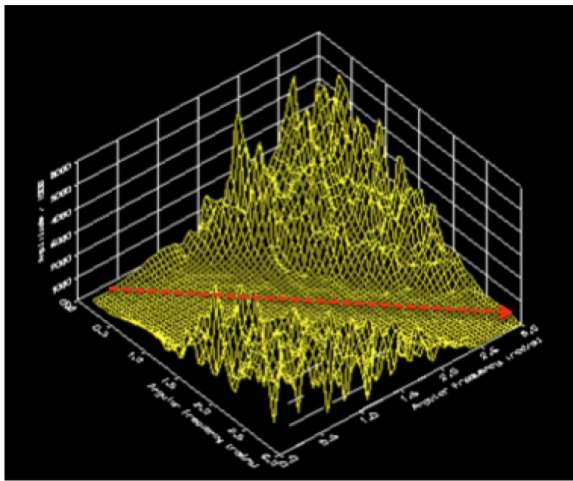


Figure C.13: Mesh 1 diff-freq. QTF in surge

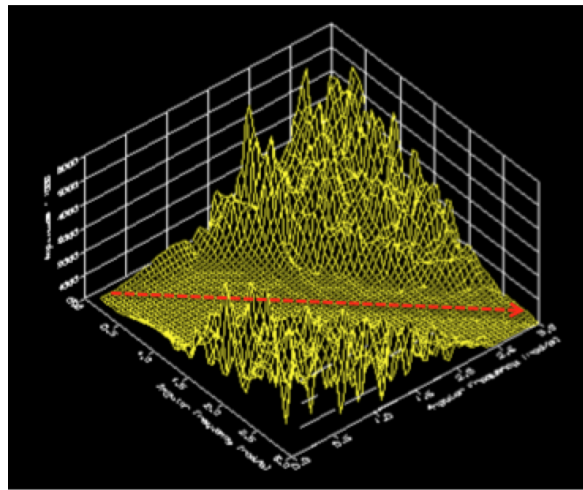


Figure C.14: Mesh 2 diff-freq. QTF in surge

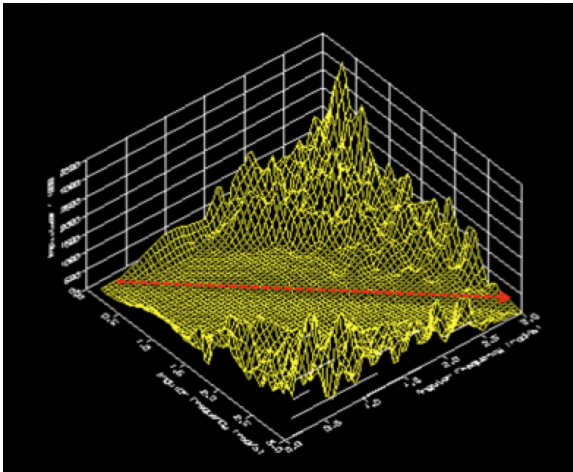


Figure C.15: Mesh 3 diff-freq. QTF in surge

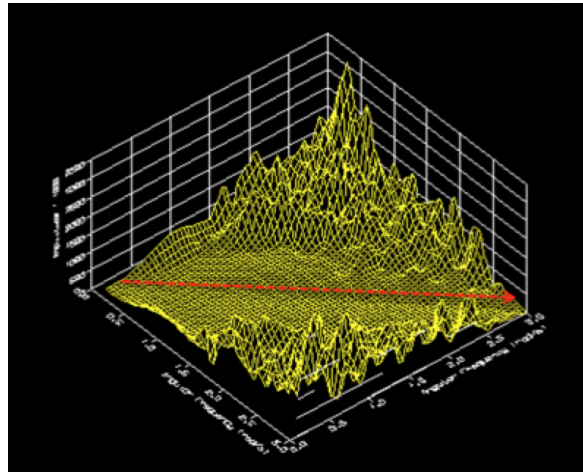


Figure C.16: Mesh 4 diff-freq. QTF in surge

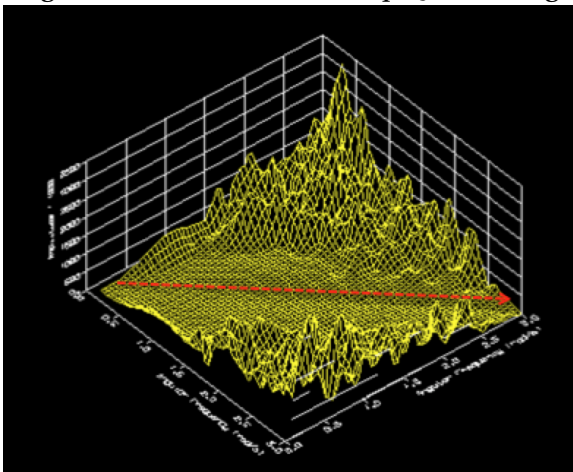


Figure C.17: Mesh 5 diff-freq. QTF in surge

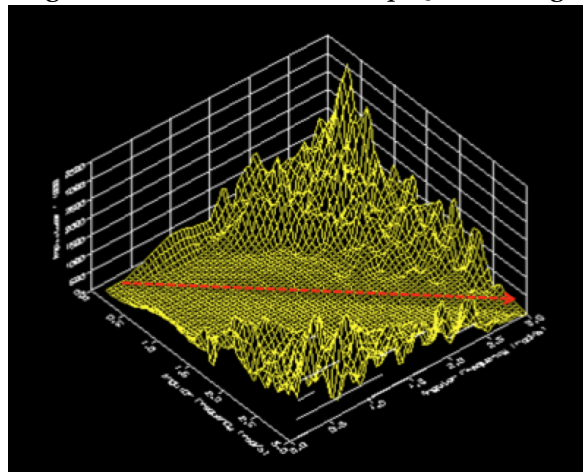


Figure C.18: Mesh 6 diff-freq. QTF in surge

# Appendix D

## Combined sys.dat File Generation

Since the current version of SIMA (V3.2) is impossible to read QTFs, the Wadam data (G1.SIF file) should be imported to DeepC first and then generate a sys.dat file for the reading in Sima. Input to DeepC is the frequency depended added mass, potential damping, restoring forces, excitation forces and second-order results calculated in HydroD. The environment condition is defined in DeepC at first, which includes definition of wave, wind, seabed etc. Note the motion type must be specified as "coupled".

Instead of developing a SRA model, only a rigid-body is developed in DeepC, which is sufficient to create an input with correct commands for first-order and second-order wave loads (Figure D.1). However the retardation element (3,3) is noticed looking wired, when checked in DeepC (Figure D.2) since only 7 frequencies are involved in the calculation, and thus a combined sys.dat file from first-order results and second-order results is created for solving this problem. The process for generating this combined sys.dat file is given in Appendix E.

In DeepC, the retardation functions are calculated for different retardation elements. They are the equivalent of a time domain input of the vessel added mass and potential damping, meaning that the vessel data must be read prior to calculating them. In fact, two "bi-products" result from the calculation process of retardation functions, namely added mass at infinite frequency and extra damping required to prevent negative damping (displayed in Figure D.3) [DNV \(2014a\)](#). These "bi-products" will be applied to the time-domain simulation of the vessel mo-

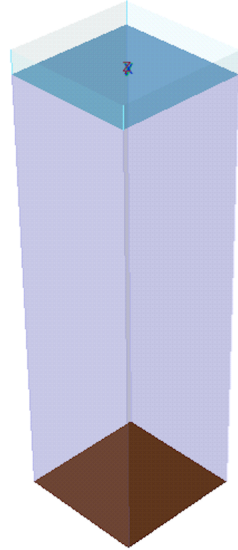


Figure D.1: Overview of the DeepC model

tion.

Figure D.2 displays the change of retardation element (3,3) over the time, where time step  $0.5s$  is used. However, it seems that the retardation function goes to zero until about  $2400s$ . This is because 25 frequencies ( $0.2rad/s$  to  $1.4rad/s$  with a frequency step  $0.2rad/s$ ) are used in the HydroD model. 7 frequencies are definitely enough for the second-order loads calculation, but not for the first-order loads calculation.

In order to solve this problem, another HydroD model with more frequencies involved ( $0.1rad/s$  to  $3rad/s$  with a frequency step  $0.1rad/s$ ) is created and only the first-order results are calculated for the sake of time-saving. The new generated retardation function is shown in Figure D.3. Now, the retardation element (3,3) trends to be zero after  $48s$ , which is much more reliable.

In this case, the first order wave excitation part in the original sys.dat file is replaced by the same part in the new sys. dat (Figure D.4). Then one can get the combined sys.dat file.

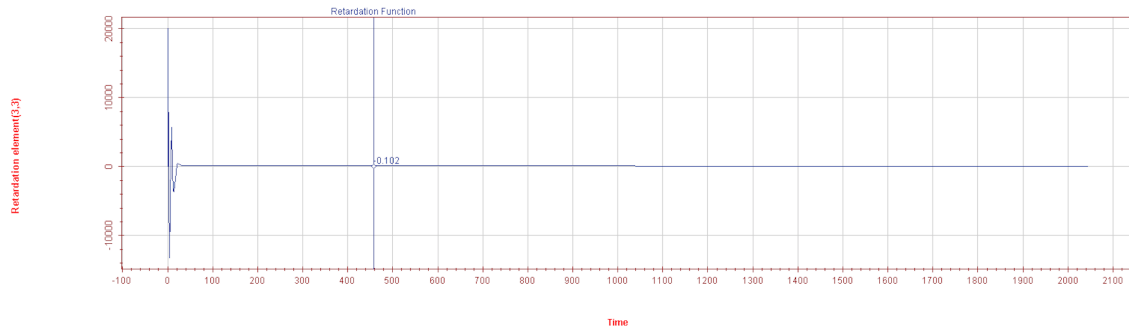


Figure D.2: The variation of the retardation element (3,3) over time

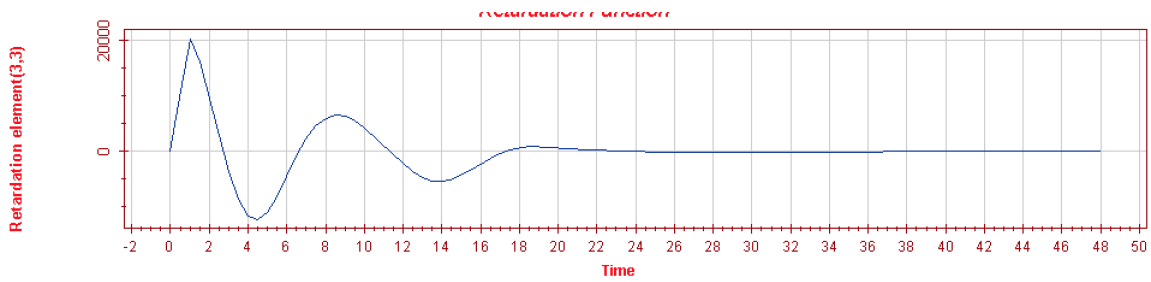


Figure D.3: The variation of the retardation element (3,3) over time

```

TestPad - W:\DeepC\firstloads\Analysis\sys-Analysis.dat
File Edit Search View Tools Macros Configure Window Help
sys-Analysis.dat
Quadratic damping coefficients for vessel: vessel
-----
      DL11      DL12      DL13      DL14      DL15      DL16
0.000e+000 0.000e+000 0.000e+000 0.000e+000 0.000e+000 0.000e+000
0.000e+000 0.000e+000 0.000e+000 0.000e+000 0.000e+000 0.000e+000
0.000e+000 0.000e+000 0.000e+000 0.000e+000 0.000e+000 0.000e+000
0.000e+000 0.000e+000 0.000e+000 0.000e+000 0.000e+000 0.000e+000
0.000e+000 0.000e+000 0.000e+000 0.000e+000 0.000e+000 0.000e+000
0.000e+000 0.000e+000 0.000e+000 0.000e+000 0.000e+000 0.000e+000
0.000e+000 0.000e+000 0.000e+000 0.000e+000 0.000e+000 0.000e+000
0.000e+000 0.000e+000 0.000e+000 0.000e+000 0.000e+000 0.000e+000
-----
FIRST ORDER WAVE EXCITATION
=====
1st order wave force transfer function for vessel: vessel
-----
      nfordir  nfofre  ifosym  itypin
1           30      2         1

WAVE DIRECTION FORCE TRANSFER FUNCTION
-----
      ifodir  fodir (deg)
1           1           0.000

WAVE FREQ FORCE TRANSFER FUNCTION
-----
      ifreq  fofrfe (rad/T)
1           1           0.10000
2           2           0.20000
3           3           0.30000
4           4           0.40000
5           5           0.50000
6           6           0.60000
7           7           0.70000
8           8           0.80000
9           9           0.90000
10          10          1.00000
11          11          1.10000
12          12          1.20000
13          13          1.30000
14          14          1.40000
15          15          1.50000
16          16          1.60000
17          17          1.70000
18          18          1.80000
19          19          1.90000
20          20          2.00000
21          21          2.10000
22          22          2.20000
23          23          2.30000
24          24          2.40000
25          25          2.50000
26          26          2.60000
27          27          2.70000
28          28          2.80000
    
```

Figure D.4: The first order wave excitation part in the new sys.dat file

# Appendix E

## RIFLEX Models

The following definitions are made for the DTU 10MW Wind Turbine (Figure E.1):

- Every line has two supernodes (blue dots shown in Figure E.1) at the ends .
- Every blade consists of two lines: one eccentricity ( $2.8m$ ) and one foil ( $86.266m$ ). Blade "eccentricity" is a stiff element connecting shaft to blade. While the blade "foil" is the rest of the blade.
- End 2 of the eccentricity must be at the same position as the end 1 of the foil. All the supernodes in same position are marked by red circles in Figure E.1.
- There must be a rigid connection between the end 2 of the eccentricity and the end 1 of the foil.
- The supernodes at the tower bottom should be fixed.
- The shaft line must be a single line, which have two segments connected by a FLEX joint. The FLEX joint is free in x-direction, and fixed in y- and z- directions. A dummy stiffness is given in x-direction.
- The nacelle is connected to tower top.

In addition, the three TLP tendons are also defined in the same way in SIMA.

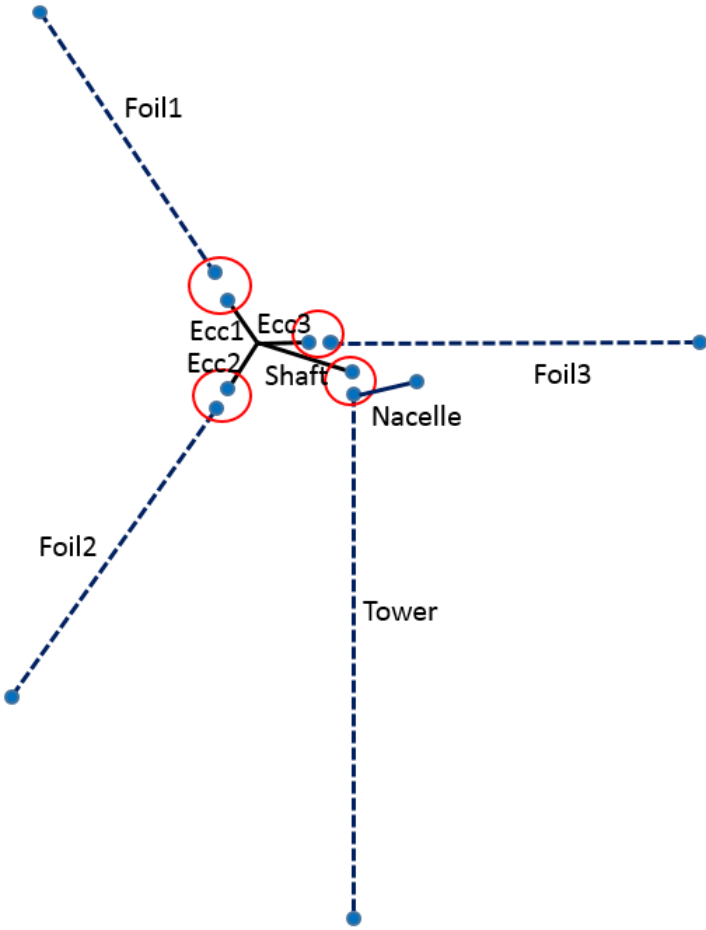


Figure E.1: RIFLEX wind turbine model

# **Appendix F**

## **Turbulence wind test response**

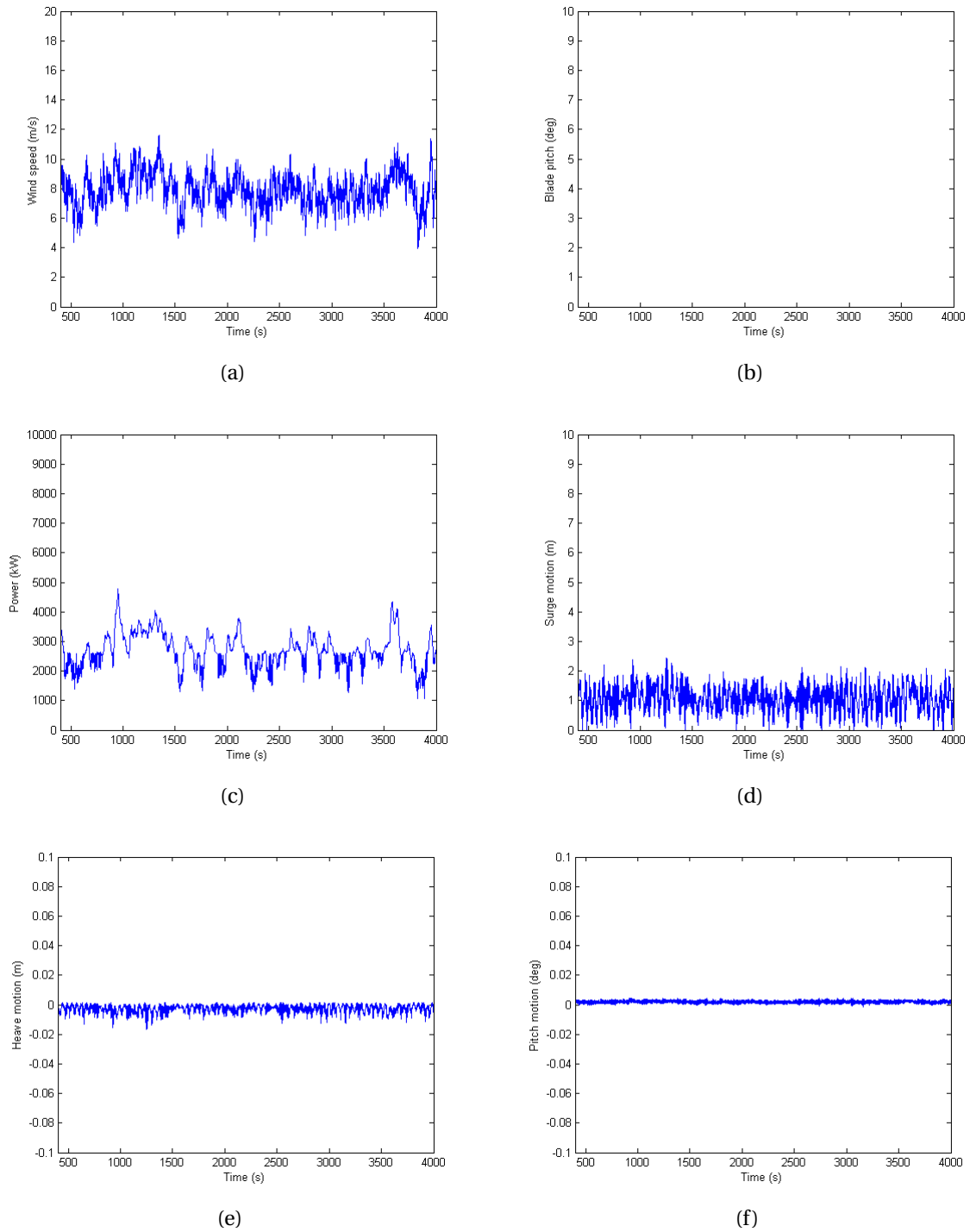


Figure F.1: Time realizations of wind speed, blade pitch, generated power, surge motion, heave motion and pitch motion of the TLPWT for turbulence wind test in load case OP1



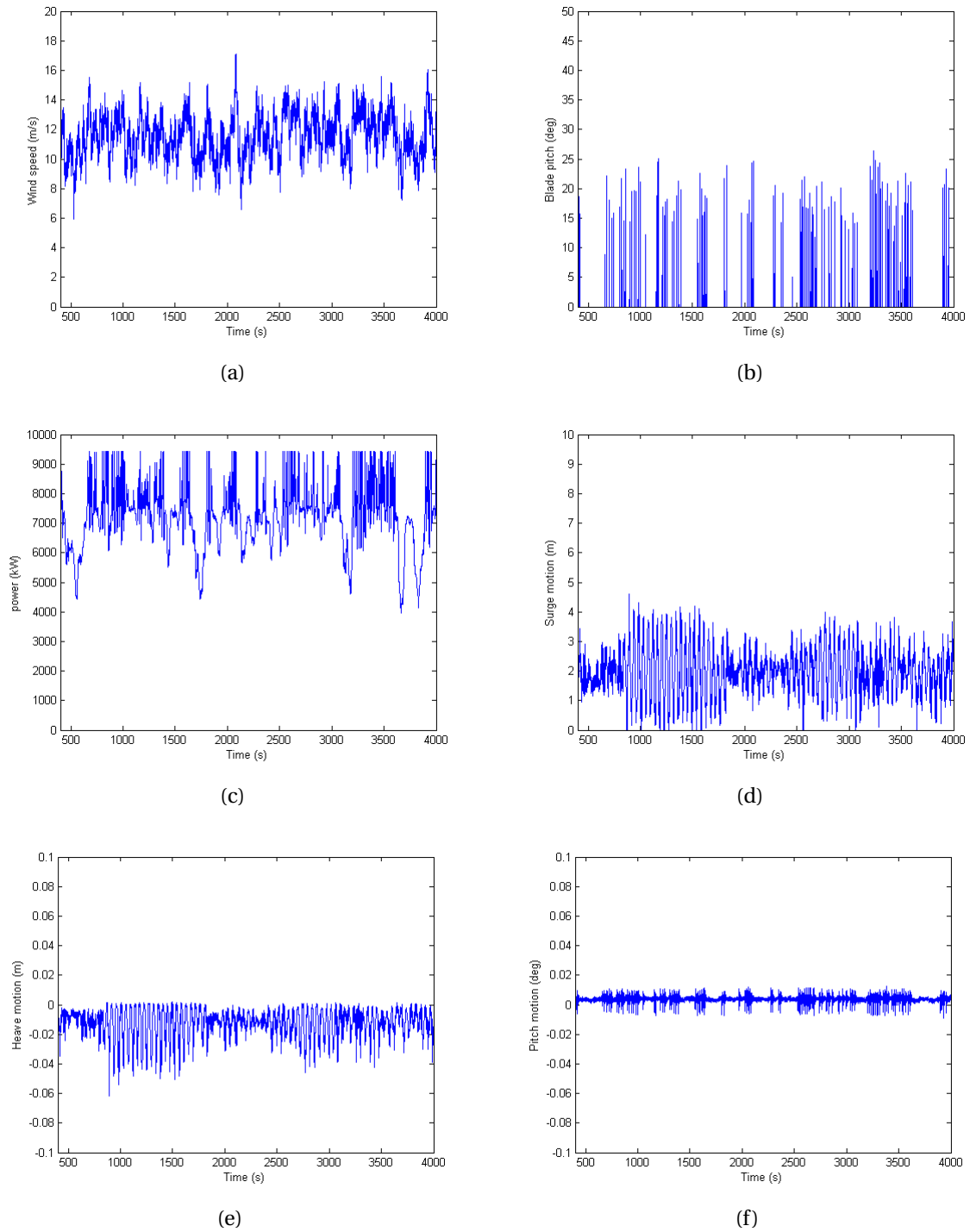


Figure F.2: Time realizations of wind speed, blade pitch, generated power, surge motion, heave motion and pitch motion of the TLPWT for turbulence wind test in load case OP2

# Bibliography

- Alan Price, James Platt, B. W. (2015). *Full power at Westermost Rough offshore wind farm*. Dong Energy.
- API (2010). *Planning, designing and constructing tension leg platforms (Edition 3)*. American Petroleum Institute.
- Bachynski, E. E. (2014). *Design and Dynamic Analysis of Tension Leg Platform Wind Turbine*. Norwegian University of Science and Technology, Trondheim, Norway.
- Bachynski, E. E. (2015). *Basic Aerodynamics for Wind Turbines, Lecture Notes for Course Integrated Dynamic Analysis of Wind*. Norwegian University of Science and Technology, Trondheim, Norway.
- Bachynski, E. E., Moan, T., et al. (2012). Linear and nonlinear analysis of tension leg platform wind turbines. In *The Twenty-second International Offshore and Polar Engineering Conference*. International Society of Offshore and Polar Engineers.
- Bae, Y. and Kim, M. (2013). Rotor-floater-tether coupled dynamics including second-order sum-frequency wave loads for a mono-column-tlp-type fowt (floating offshore wind turbine). *Ocean Engineering*, 61:109–122.
- Bak, C., Zahle, F., Bitsche, R., Kim, T., Yde, A., Henriksen, L. C., Natarajan, A., and Hansen, M. (2013). Description of the dtu 10 mw reference wind turbine. *DTU Wind Energy Report-I-0092*.
- Boorsma, K. (2012). Power and loads for wind turbines in yawed conditions. Technical report, ECN-E-12-047, ECN, Petten, The Netherlands.

Bousman, W. G. (2009). Uh-60 airloads program tutorial.

Burton, T., Sharpe, D., Jenkins, N., and Bossanyi, E. (2001). *Wind energy handbook*. John Wiley & Sons.

Cheng, Z., Wang, K., Gao, Z., Moan, T., et al. (2015). Dynamic modelling and analysis of three floating wind turbine concepts with vertical axis rotor. In *The Twenty-fifth International Offshore and Polar Engineering Conference*. International Society of Offshore and Polar Engineers.

Chenyu Luan, Zhen Gao, T. M. (2015). *Criteria and procedure for concept design of the hulls of semi-submersible wind turbines*. Norwegian University of Science and Technology, Trondheim, Norway.

DNV (1994). Wadam - wave analysis by diffraction and morison theory. *SESAM user's manual, Høvik*.

DNV (2008). *Structural design of TLPs (LRFD method), DNV-OS-C105*. Det Norske Veritas.

DNV (2010a). Global performance analysis of deepwater floating structures. *Høvik: Det Norske Veritas*.

DNV (2010b). Wadam user manual. *Det Norske Veritas*.

DNV (2011). *SESAM user course - GeniE workshop: modeling a semisubmersible - panel, morison and structural (FE) modes*. Norway.

DNV (2013a). Design of floating wind turbine structures. *Offshore Standard DNV-OS-J103*.

DNV (2013b). *SESAM user manual HydroD (wave load and stability analysis of fixed and floating structures)*. Det Norske Veritas.

DNV (2014a). *DeepC user's manual (Version V4.8-04)*. Det Norske Veritas.

DNV (2015). *SESAM user course in stability and hydrostatic analysis HydroD workshop: perform the analysis in HydroD*. Norway.

- DNV, G. (2014b). Environmental conditions and environmental loads. *Recommend Practice DNV-RP-C205*.
- Dolan, D. S. and Lehn, P. W. (2006). Simulation model of wind turbine 3p torque oscillations due to wind shear and tower shadow. In *Power Systems Conference and Exposition, 2006. PSCE'06. 2006 IEEE PES*, pages 2050–2057. IEEE.
- Edenhofer, O., Pichs-Madruga, R., Sokona, Y., Seyboth, K., Kadner, S., Zwickel, T., Eickemeier, P., Hansen, G., Schlömer, S., von Stechow, C., et al. (2011). *Renewable energy sources and climate change mitigation: Special report of the intergovernmental panel on climate change*. Cambridge University Press.
- Erich, H. (2000). Wind turbines: fundamentals, technologies, application, economics.
- Faltinsen, O. (1993). *Sea Loads on Ships and Offshore Structures*. Cambridge Ocean Technology Series. Cambridge University Press.
- Gao, Z. (2015). *Lecture notes for 'Integrated analysis of offshore wind turbines (hydrodynamic analysis of offshore wind turbines)*. Norwegian University of Science and Technology, Trondheim, Norway.
- Greco, M. (2012). *Lecture notes to TMR 4215: Sea loads*. Norwegian University of Science and Technology.
- Gruet, R. et al. (2011). Wind energy and eu climate policy. *Report, European Wind Energy Association, Brussels*. URL [www.ewea.org](http://www.ewea.org).
- Gueydon, S., Wuillaume, P.-Y., Jonkman, J., Robertson, A., Platt, A., et al. (2015). Comparison of second-order loads on a tension-leg platform for wind turbines. In *The Twenty-fifth International Offshore and Polar Engineering Conference*. International Society of Offshore and Polar Engineers.
- Hansen, M. O. (2008). *Aerodynamics of wind turbines*. Earthscan, UK and USA, 2nd edition.
- Hansen, M. O. (2015). *Aerodynamics of wind turbines*. Routledge.

- Henderson, A., Leutz, R., Fujii, T., et al. (2002). Potential for floating offshore wind energy in Japanese waters. In *The Twelfth International Offshore and Polar Engineering Conference*. International Society of Offshore and Polar Engineers.
- IEC (2005). *Medical electrical equipment - Part 1: General requirements for basic safety and essential performance*. International Electrotechnical Commission.
- Jonkman, B. J. (2009). Turbsim user's guide: Version 1.50.
- Kibbee, S. (1996). Seastar minimal platform for small deepwater reserves.
- Kibbee, S. E., Leverette, S. J., Davies, K. B., Matten, R. B., et al. (1999). Morpeth seastar mini-tlp. In *Offshore Technology Conference*. Offshore Technology Conference.
- Kim, M. and Yue, D. (1988). The nonlinear sum-frequency wave excitation and response of a tension-leg platform.
- Kvittem, M. I. (2014). Modelling and response analysis for fatigue design of a semi-submersible wind turbine.
- Leithead, W. (2007). *Wind energy*. DOI: 10.1098/rsta.2006.1955. Philosophical Transactions of the Royal Society.
- Li, L., Gao, Z., and Moan, T. (2013). Joint environmental data at five European offshore sites for design of combined wind and wave energy devices. In *ASME 2013 32nd International Conference on Ocean, Offshore and Arctic Engineering*, pages V008T09A006–V008T09A006. American Society of Mechanical Engineers.
- Li, L., Gao, Z., and Moan, T. (2015). Joint distribution of environmental condition at five European offshore sites for design of combined wind and wave energy devices. *Journal of Offshore Mechanics and Arctic Engineering*, 137(3):031901.
- Lindenburg, C. (2003). Investigation into rotor blade aerodynamics. *ECN Report: ECN-C-03-025*.
- Liu, S. and Janajreh, I. (2012). Development and application of an improved blade element momentum method model on horizontal axis wind turbines. *International Journal of Energy and Environmental Engineering*, 3(1):1–10.

- Lundteigen, M. A. and Rausand, M. (2008). Spurious activation of safety instrumented systems in the oil and gas industry: Basic concepts and formulas. *Reliability engineering & system safety*, 93(8):1208–1217.
- Lygren, J. E. L. (2011). Dynamic response analysis of a tension-leg floating wind turbine.
- Manwell, J. F., McGowan, J. G., and Rogers, A. L. (2010). *Wind energy explained: theory, design and application*. John Wiley & Sons.
- MARINTEK (2011). *SIMO user's manual*. MARINTEK, Trondheim, Norway.
- MARINTEK (2012a). *RIFLEX user's manual*. MARINTEK, Trondheim, Norway.
- MARINTEK (2012b). *SIMO theory manual*. MARINTEK, Trondheim, Norway.
- MARINTEK (2013). *RIFLEX user's manual*. MARINTEK, Trondheim, Norway.
- Matha, D. (2010). Model development and loads analysis of an offshore wind turbine on a tension leg platform with a comparison to other floating turbine concepts: April 2009. Technical report, National Renewable Energy Laboratory (NREL), Golden, CO.
- Mathisen, J. and Price, W. (1985). Estimation of ship roll damping coefficients. *Royal Institution of Naval Architects Transactions*, 127.
- Matzat, G. (2014). Top 10 things you didn't know about offshore wind energy. *U.S. Department of Energy*.
- Moan, T. (1994). *Design of marine structures, Vol. 1*. Norwegian University of Science and Technology, Trondheim, Norway.
- Moriarty, P. J. and Hansen, A. C. (2005). *AeroDyn theory manual*. Citeseer.
- Musial, W., Butterfield, S., and Boone, A. (2004). Feasibility of floating platform systems for wind turbines. In *23rd ASME Wind Energy Symposium, Reno, NV*.
- Newland, D. (1993). *An introduction to random vibrations, spectral and wavelet analysis*. Longman Scientific & Technical.

- Newman, J. N. (1977). *Marine hydrodynamics*. MIT press.
- NMD (1987). *Regulations for design (construction) of mobile platforms*. the Norwegian Maritime Directorate, Oslo, Norway.
- Obasaju, E., Bearman, P., and Graham, J. (1988). *A study of forces, circulation and vortex patterns around a circular cylinder in oscillating flow*, volume 196. Cambridge University Press.
- Ormberg, H., Bachynski, E. E., et al. (2012). Global analysis of floating wind turbines: Code development, model sensitivity and benchmark study. In *The Twenty-second International Offshore and Polar Engineering Conference*. International Society of Offshore and Polar Engineers.
- Peters, D. A. and He, C. J. (1991). Correlation of measured induced velocities with a finite-state wake model. *Journal of the American Helicopter Society*, 36(3):59–70.
- Pitt, D. M. and Peters, D. A. (1981). Theoretical prediction of dynamic-inflow derivatives. *Vertica*, 5(1):21–34.
- Refat, H. M. and El-gamal, A. R. (2014). Influence of the density of water on the dynamic behavior of square tension leg platform. *American Journal of Civil Engineering and Architecture*, 2(4):122–129.
- Roddier, D., Peiffer, A., Aubault, A., and Weinstein, J. (2011). A generic 5 mw windfloat for numerical tool validation & comparison against a generic spar.
- Smith, M. (2015). Chevron cable loss in rough seas in the gulf of mexico delays 5.1 billion development. <http://metroforensics.blogspot.no/2015/06/chevron-cable-loss-in-rough-seas-in.html>.
- Snel, H., Schepers, J., and Nederland, S. E. C. (1995). *Joint investigation of dynamic inflow effects and implementation of an engineering method*. Netherlands Energy Research Foundation ECN.
- Srinivasan, N. (2014). *Tension-based tension leg platform*. Google Patents. US Patent 8,764,346.
- Than, K. (2006). Floating ocean windmills designed to generate more power. *LiveScience*, 18:214–15.

- Tian, X. (2015). *Design and Analysis of a TLP Floater Supporting the DTU 10MW Wind Turbine (Specialization Project)*. Norwegian University of Science and Technology, Trondheim, Norway.
- Veritas, D. N. (2008). Offshore standard dnv-os-e301: Position mooring.
- Veritas, N. (2001). *Stability and watertight integrity*. Det Norske Veritas.
- WAMIT (1998). *Wamit user manual (Version 6.4, 6.4S), Chapter 11 Second-order module*. WAMIT Inc., Chestnut Hill, MA, USA.
- Wang, Q. (2014). *Design of a Steel Pontoon-type Semi-submersible Floater Supporting the DTU 10MW Reference Turbine*. PhD thesis, TU Delft, Delft University of Technology.
- Wayman, E. N., Sclavounos, P., Butterfield, S., Jonkman, J., Musial, W., et al. (2006). Coupled dynamic modeling of floating wind turbine systems. In *Offshore Technology Conference*. Offshore Technology Conference.
- Wind, M. V. O. (2013). The v164-8.0 mw turbine. <http://www.mhivestasoffshore.com/Products-and-services/The-Turbines>, 164.